

T-3645

**LOW ENERGY ELECTRON DIFFRACTION DETERMINATION
OF SURFACE STRUCTURE APPLIED TO
CHEMISORPTION AND TO
MARTENSITIC ALLOYS**

by

David J. Hannaman

**ARTHUR LAKES LIBRARY
COLORADO SCHOOL of MINES
GOLDEN, COLORADO 80401**

ProQuest Number: 10796384

All rights reserved

INFORMATION TO ALL USERS

The quality of this reproduction is dependent upon the quality of the copy submitted.

In the unlikely event that the author did not send a complete manuscript and there are missing pages, these will be noted. Also, if material had to be removed, a note will indicate the deletion.



ProQuest 10796384

Published by ProQuest LLC (2019). Copyright of the Dissertation is held by the Author.

All rights reserved.

This work is protected against unauthorized copying under Title 17, United States Code
Microform Edition © ProQuest LLC.


ProQuest LLC.
789 East Eisenhower Parkway
P.O. Box 1346
Ann Arbor, MI 48106 – 1346

T-3645

A thesis submitted to the Faculty and the Board of Trustees of the Colorado School of Mines in Partial fulfillment of the requirements for the degree of Doctor of Philosophy (Applied Physics).

Golden, Colorado

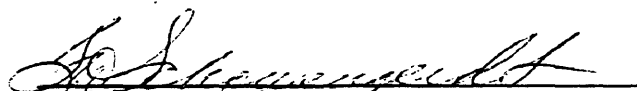
Date 1-19-89

Signed: 
David J. Hannaman

Approved: 
Dr. Mark A. Passler
Thesis Advisor

Golden, Colorado

Date 1/19/89

Signed: 
Dr. Franklin D. Schowengerdt
Professor and Head,
Physics Department

ABSTRACT

Low Energy Electron Diffraction has been used to determine the surface structure of four systems. The first is the full coverage Ni(110)-(2x1)2CO system. At 125 K CO is found, by intensity analysis, to adsorb to the short bridge site with an alternating tilt from the vertical. The structure is unique in that the metal-C and C-O tilt angles differ. The structural parameters determined are the metal-C (1.95 Å) and C-O (1.12 Å) bond lengths, the metal-C tilt (27°) and the C-O tilt (17°). The clean metal contraction is relaxed by the presence of the CO. The structure of the 0.4 coverage Ni(110)-NO system at 125 K has also been determined. NO has been found to adsorb molecularly in a horizontal configuration across the long bridge with a highly dilated bond length of 1.45 Å and a Ni-N,O bond length of 1.72 Å. The surfaces of two martensitically transforming alloys have also been studied. The first alloy was a CuZnAl sample which undergoes a bcc to 9R transformation at -30°C. At room temperature a (3x1) surface reconstruction, spot splitting, and lack of inversion symmetry was observed in the LEED pattern. On the basis of these observations a model for the formation of surface martensite is proposed. The second martensitic

T-3645

alloy investigated was a FeNi alloy which undergoes a fcc to bcc transformation at 110 K. The surface was studied at temperatures down to 180 K and no surface martensite was observed. From intensity-temperature measurements the effective surface Debye temperature was determined to be 303 K. From an IV analysis the first interplanar separation was found to be contracted 3% and the second interplanar distance dilated 1% from the bulk value.

TABLE OF CONTENTS

	<u>Page</u>
ABSTRACT	iii
LIST OF FIGURES	vii
LIST OF TABLES	ix
LIST OF ABBREVIATIONS	x
ACKNOWLEDGEMENTS	xi
1. INTRODUCTION	1
A. Scope	1
B. Low Energy Electron Diffraction: A Primer	6
2. SURFACE STRUCTURE OF NI(110)-(2X1)2CO	13
A. Previous Work	13
B. Experimental	17
C. Analysis	18
D. Results	21
E. Discussion	31
3. SURFACE STRUCTURE OF NI(110)-NO	35
A. Previous Work	35
B. Experimental	37
C. Analysis	38
D. Results	46
E. Discussion	55

4.	SAMPLE PREPARATION	57
	A. Composition	57
	B. Orientation	62
	C. Polishing	64
	D. In Situ Cleaning and Anealing	65
5.	SURFACE STRUCTURE OF BETA-BRASS	69
	A. Motivation	69
	B. Experimental	72
	C. Models Proposed	79
	D. Discussion	86
6.	SURFACE STRUCTURE OF FeNi	88
	A. Motivation	88
	B. Experimental	89
	C. Analysis	99
	D. Results	101
	E. Discussion	107
	REFERENCES CITED	114
	APPENDIX: Computer Programs for Generating Stereographic Projections and Plotting Laue Back Reflection Photographs	118

LIST OF FIGURES

	<u>Page</u>
1-1. A Schematic of the LEED Experiment	7
2-1. Geometry of the fcc(110) surface	14
2-2. Four structural models for CO adsorption	20
2-3. R-factor contour plot for common CO tilt and Ni-C bond length	23
2-4. R-factor contour plot for C-O bond length and Ni-C bond length	24
2-5. Parameters for structural model of CO adsorption .	25
2-6. R-factor contour plot for metal-C tilt and C-O tilt	27
2-7. Lowest R-factor values for different metal-C and C-O bond lengths	29
2-8. Definition of nearest neighbor distances for adsorbed atoms	32
3-1. Top site adsorption models for NO adsorption . . .	40
3-2. Short bridge adsorption models for NO adsorption .	41
3-3. Long bridge adsorption models for NO adsorption .	42
3-4. Hollow adsorption models for NO adsorption	43
3-5. R-factor contour plot for Ni-N,O interlayer and N-O bond length	51
3-6. IV curves for the (10) beam	53
3-7. IV curves for the (01) beam	54
3-8. Structure of the Ni(110)-NO system	56
4-1. Representative WDS Spectrum for CuZnAl Sample . .	58
4-2. Representative WDS Spectrum for FeNi Sample . . .	61
5-1. LEED pattern of the CuZnAl surface	75

5-2.	Modulation wave of the (110) planes	82
5-3.	Lattice Displacement Wave of the close packed rows	83
6-1.	LEED pattern of the FeNi(111) surface	90
6-2.	Experimental IV curve for the (0,0) beam	92
6-3.	Intensity versus temperature for the (0,0) beam	94
6-4.	Bragg peaks of the (0,0) beam	96
6-5.	The L_0 phase shifts of Iron and Nickel	100
6-6.	Schematic of four possible stacking models	102
6-7.	IV curves for the (10) beam	103
6-8.	IV curves for the (01) beam	104
6-9.	R-factor as a function of the first interlayer	106
6-10.	R-factor contour plot of the first and second interlayer	109

LIST OF TABLES

	<u>Page</u>
4-1. WDS composition results	59
6-1. Summary of first interlayer variation as a function of lattice constant	108
6-2. Summary of first and second interlayer variations as a function of lattice constant	110

LIST OF ABBREVIATIONS

A/D	Analog to Digital
AES	Auger Electron Spectroscopy
ARUPS	Angle Resolved Ultraviolet Photoelectron Spectroscopy
BIS	Bremsstrahlung Isochromet Spectroscopy
EELS	Electron Energy Loss Spectroscopy
ESDIAD	Electron Stimulated Desorption Ion Angular Distribution
LEED	Low Energy Electron Diffraction
MEIS	Medium Energy Ion Scattering
MQS	Multi-stable Quenching Spectroscopy
M_s	Martensitic transformation starting temperature
PC	Personal Computer
SURAFS	Surface Absorption Fine Structure
TA	Transverse Acoustic
TDS	Temperature Desorption Spectroscopy
TED	Transmission Electron Diffraction
UPS	Ultraviolet Photoemission Spectroscopy
WDS	Wavelength Dispersive Spectroscopy
XPS	X-Ray Photoelectron Spectroscopy

ACKNOWLEDGEMENTS

The opportunity to acknowledge and express my appreciation of the support I have received at the Colorado School of Mines is a most pleasant task. I thank the Colorado School of Mines for financial support in the form of a teaching assistantship. I also thank the National Science Foundation for their support of the martensitic alloy investigations, under grant DMR-8612175.

I wish to thank Jack Kintner for his assistance and patience during my sojourns in the machine shop. I would like to give Faye West special thanks, not only for her help, but also for making the department office a pleasant place to be.

Bob McGrew, of the Metallurgy Department, in addition to performing the WDS measurements, was of general assistance in various other aspects of sample preparation. His help is greatly appreciated.

My committee members, Dr. Mark Passler, Dr. Timothy Hayes, Dr. Thomas Furtak, and Dr. Al Czanderna provided guidance and understanding. In particular, their critical comments on this dissertation are appreciated. Additionally I would like to thank Dr. Krauss for making available the FeNi sample.

T-3645

Dr. Mark Passler, my advisor, has provided more than just direction and insight for this research. His support and understanding during some unusual circumstances is greatly appreciated.

Finally, this thesis would not be possible without the support and love of my wife Joanne. Her patience and understanding were always there when needed, and she deserves more thanks than can be expressed here.

1. INTRODUCTION

Surface Physics has seen tremendous growth over the last twenty years. The characteristics to be determined about a surface are the composition, the structure, and the electronic and vibrational properties. Low Energy Electron Diffraction (LEED) is a nearly ideal technique to determine the structure of ordered surfaces. The large cross section of electrons scattering from atoms results in low energy electrons being effective surface probes. The diffraction pattern of the elastically scattered electrons is a direct map of the two dimensional surface reciprocal lattice while the intensities of the diffracted beams as a function of incident electron wave vector provide information on the surface basis, e.g. bond lengths and bond angles. Additionally, intensity versus temperature measurements can give insight into the surface vibrational properties.

1.A: Scope

As a surface science technique, LEED has reached the stage in the last ten years where it has provided important insight into a variety of physical processes. Among the more important, economically, are chemisorption and heterogeneous catalysis. As the geometry of a chemisorbed

adsorbate is a consequence of the bonds involved, the structure of the chemisorbed system can aid in the understanding of metal-atom and metal-molecule interactions. In addition the structure of a chemisorbed molecule may also aid in determining the mechanistic steps in heterogeneous catalysis. The first part of this dissertation deals with the structure of two adsorbates, CO and NO, on a particular surface, the Ni(110). The Ni(110) surface was expected to provide some interesting structures due to the relatively open nature of the FCC(110) surface, while the differences in chemistry of the CO and NO molecules would also provide good comparison between their chemisorbed structures.

The second half of this dissertation concerns the application of LEED to the surface of martensitic alloys in a search for a precursor to the transformation. The martensitic phase transformation is a solid-solid diffusionless transformation resulting from cooperative displacements of the atoms. The kinetics and morphology of the transition are dominated by the strain energy arising from the shear-like displacements. The transition is characterized by an orientation relationship between the parent and product lattices. This orientation correspondence results in a strain energy due to the mismatch between the two lattices. In spite of the great

deal of phenomenology known about the transformation, there is a lack of understanding of the nucleation and kinetics of growth. In an effort to gain such understanding a variety of precursive phenomena have been studied. Among the more promising is the evidence, from electron diffraction studies, that a surface martensite phase exists prior to the bulk transformation. The higher lattice energy of the surface compared to the bulk suggests that the surface may provide some of the strain energy to drive the transformation. In particular, the relative ease of surface reconstruction, due to a decrease in constraint of atomic displacements compared to the bulk, may affect the formation of surface martensite. A surface reconstruction may promote, or be a step in, the formation of surface martensite. The existence of a surface martensite and whether it acts as a nucleation site to the bulk transformation is still debated.

This thesis represents the first effort of a continuing project to investigate, with LEED, the surface structure of martensitically transforming alloys and attempt to resolve the question of whether a surface martensite is present and if so, is a true precursor to the bulk transformation. The two alloys used in this initial effort were a CuZnAl alloy and a FeNi alloy. For CuZnAl alloys there is a large amount

of evidence for a surface martensite phase while for FeNi alloys the evidence is more debatable. In addition these two alloys differ in the amount of strain accompanying the transformation: the brass exhibiting moderate strain and the FeNi having large strain. Thus the results for these two alloys should provide a good basis for subsequent study.

The plan for the rest of the dissertation is as follows. This introductory chapter finishes with a brief discussion of the LEED experiment and some of the common analysis methods used throughout this thesis to determine a surface structure.

Chapter Two concerns the determination of the surface structure of the Ni(110)-(2x1)2CO system. In the first section the existing literature on this system is covered. While in sections B and C the experimental details and the analysis programs are described. In section D the results of the theoretical calculations are given. The chapter ends with a discussion of our results and how they compare with other measurements.

Chapter Three parallels Chapter Two for the Ni(110)-NO system.

Chapter Four begins the work on the martensitic alloy surface structure investigations by discussing the technical details of the samples and the preparation procedures used.

In section A the composition and the transformation temperatures of the CuZnAl and the FeNi samples are discussed. In section B the procedures used to orient the samples to the desired crystal faces are detailed. Next the polishing and etching procedures are explained. The chapter ends with the high vacuum cleaning and annealing procedures developed for the two samples.

In Chapter Five the investigation of the CuZnAl sample is presented. The chapter begins with a brief discussion of the evidence for surface martensite in beta phase alloys. The experimental details and observations are discussed in section B. This is followed by some models presented to explain the details of the LEED pattern and the formation of surface martensite. The chapter ends with a discussion on the presence of surface martensite as determined by our experiments.

Chapter Six covers the work on the FeNi alloy. The evidence for surface martensite in FeNi alloys is discussed in section A. In section B the experiments performed on this alloy are detailed, including intensity vs. temperature measurements to determine the effective surface Debye temperature. The theoretical programs to analyze the IV curves are covered in section C and in section D the results are presented. This is followed by a comparison of our

results to similar systems and how they relate to the presence of a surface martensite on this alloy.

1.B: Low Energy Electron Diffraction: A Primer

The LEED experiment is illustrated schematically in Fig. 1-1. An incident electron beam is focused on the sample. Typically this electron beam has diameter on the order of 1 mm and a coherence length of 100 Å. The electron emission is adjusted to provide a linear emission current as a function of energy. The inelastically scattered electrons are separated from the diffracted electron beams by a set of retarding grids. The diffracted electrons are subsequently accelerated towards a fluorescent screen where they are then imaged. The system used for our experiments imaged through a video camera where the beam intensities can be measured in real time or recorded for later analysis. The portion of the video signal (window) near a diffraction spot is analog integrated using appropriately timed boxcar integrators. The integrated intensities are stored on a PC after A/D conversion. The PC calculates the window position and continuously positions the integrator window on the spot. Video vertical sync pulses are used to simultaneously clock both the window position and the electron energy ramp.

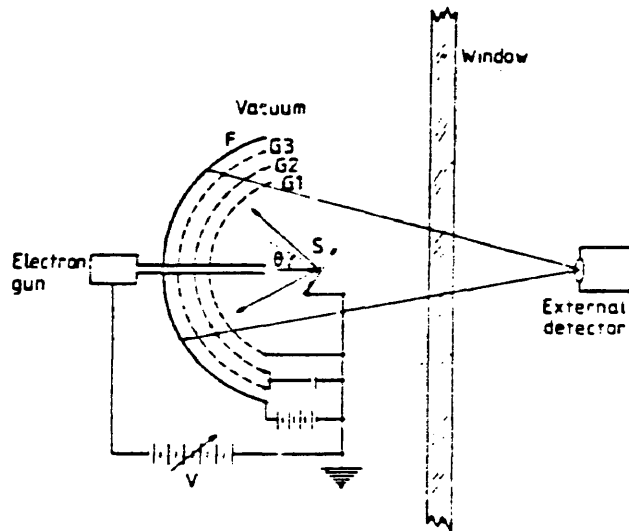


Figure 1-1. Schematic of LEED Experiment. Defined in the figure are the sample S, the three retarding grids G1, G2, and G3, and the fluorescent screen F.

Stray magnetic fields near the sample are minimized with two sets of Helmholtz coils. The sample is mounted on a manipulator which allows for rotation about one axis and tilt about the other two axes. This permits measurements to be taken at both normal and off-normal incidence of the electron beam to sample. In addition, the temperature of the sample can be varied from approximately 125 K to 800 K. Cooling is achieved by pumping liquid nitrogen through coils which are wrapped about the sample mount. Heating is through a heating filament mounted directly behind the sample. Electron emission from the filament onto the back of the sample mount provides the majority of heating at high temperatures.

As a diffraction experiment Low Energy Electron Diffraction is a tool to determine crystallographic structure. The wavelength (1 \AA at 150 eV), and the short mean free path ($\sim 10 \text{ \AA}$), of low energy electrons make LEED well suited to surface structure studies. In analogy to x-ray and neutron diffraction, the diffraction pattern is a map of the reciprocal lattice, while the intensities of the diffracted beams provide basis information (surface geometry, bond lengths, bond angles, etc.). In contrast to x-ray and neutron diffraction, which probe the three dimensional structure, LEED probes the structure of the top

few layers only. Thus, information from a LEED experiment is not three dimensional, and not strictly two dimensional, but has aspects of both. In general, each layer is assumed to have two dimensional periodicity parallel to the surface. The third dimension (perpendicular to the surface) is allowed to vary, both within and between layers.

That the LEED diffraction pattern is a direct map of the two dimensional reciprocal lattice of the surface, can be seen from the two dimensional periodicity of the surface, and Bloch's Theorem. Inside the crystal, the electron wave vector parallel to the surface is conserved to within a reciprocal lattice vector. Thus the emerging diffracted electrons can have momentum parallel to the surface equal to any reciprocal lattice vector (plus the incident parallel momentum) subject to the restriction that the total energy of the diffracted electrons be less than or equal to the incident electron energy. This energy restriction on the emerging beams limits the number of spots that are seen at a given energy.

Basis information is obtained by measurements of the intensity of the diffracted beams as a function of the incident electron wave vector. The standard practice, and the one used throughout our analysis, is to measure the intensity of the diffracted beams as a function of incident

electron energy (IV curves).

The high atomic scattering cross section of electrons with energy less than 1000eV which makes LEED such a powerful surface probe also complicates the analysis. Unlike x-ray diffraction in which a kinematic single scattering approach is sufficient to describe the diffraction intensities, LEED requires a dynamic multiple scattering calculation of the diffraction intensities. Fortunately, several calculational schemes are available for this purpose, among the most common and the computer codes used throughout our analysis, are the VanHove-Tong subroutines (1).

The method of determining the surface structure from a set of IV curves is an iterative approach. A set of calculations are performed for an initial set of trial geometries. A comparison of the theoretical and experimental curves then dictates the choice for the next set of IV calculations. The correct structure is converged upon by increasing the agreement between theory and experiment. Care must be taken to explore a wide variety of geometries and parameters to decrease the chance that the correct structure was bypassed through a poor choice of geometries and parameters.

While visual comparison of the experiment and theory is

sufficient for separating out initial geometries and models, the changes in the IV curves, as the correct structure is converged upon, become subtle and subjective, necessitating an objective comparison. This comparison between the theoretical and experimental curves is facilitated by the use of a numerical R-factor (or Reliability factor). A variety of R-factors exist for this purpose (2), the majority of which are sensitive to peak positions and relative peak heights. They differ mostly in their approach to measuring this sensitivity. We chose the Zanazzi-Jona R-factor (3). Based on experience and common agreement, a Zanazzi-Jona R-factor of < 0.2 implies that a structure is very probable, $0.2 < \text{R-factor} < 0.35$ indicates a structure is probable, and an R-factor > 0.5 indicates that the structural determination is doubtful. To allow for error in the experimental energy scale, plus the uncertainty of the exact inner potential to use in the calculations, the experimental IV curves are shifted from -5 eV to $+5 \text{ eV}$ with respect to the theory during the R-factor analysis. To facilitate the interpretation of the R-factor results, contour plots of the R-factor versus two of the structural parameters are made. The contour plots used throughout this dissertation were made using the SURFACE II plotting program (4). Typically a third order polynomial surface was fit to the R-factor data.

From these contour plots trends and correlations in the data can be readily seen.

2. SURFACE STRUCTURE of Ni(110)-(2x1)2CO

2.A: Previous Work

The adsorption of CO on Ni(110) has received considerable attention recently for several reasons. Technologically, the adsorption of CO on this surface involves one component of catalytic reactions of economic importance such as methanation and Fischer-Tropsch synthesis of hydrocarbons. Physically, this system appears unusual in that CO, at full coverage, adsorbs in a tilted configuration.

The fcc(110) surface shown in Fig. 2-1 is highly anisotropic for a low index surface. It has close packed nickel atoms in the $[\bar{1}10]$ direction and a $2^{\frac{1}{2}}$ larger 2D spacing in the $[001]$ direction. By convention the first surface coordinate is in the direction of the smaller lattice spacing or the $[\bar{1}10]$ direction. Defined in the figure are the high symmetry adsorption sites - top, short bridge, long bridge, and hollow. The short bridge and long bridge correspond to the $[\bar{1}10]$ and $[100]$ directions respectively.

Previous LEED studies of this system focused solely on the sequence of patterns associated with the adsorption process. Behm (5) observed a sequence of patterns $c(8x2)$ to

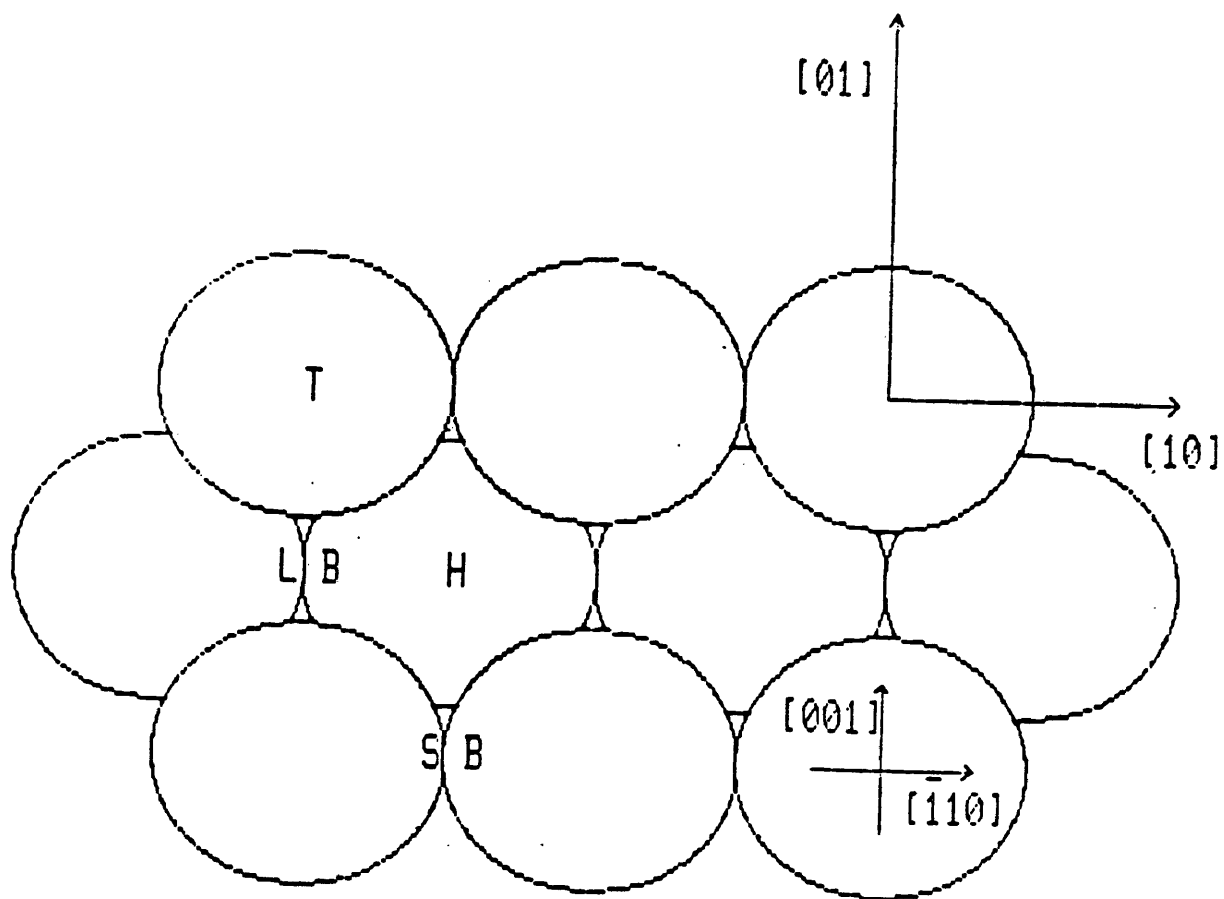


Figure 2-1. Geometry of the fcc(110) surface showing four possible adsorption sites: top (T), short bridge (SB), long bridge (LB), and hollow (H).

c(4x2) to (2x1) at full coverage. At normal incidence the $((2n+1)/2, 0)$ beams were missing, indicating a (001) glide plane. This (2x1) unit cell with the observed (110) mirror plane and (001) glide plane has structural notation $(2x1)p2mg$. These observations are consistent with a model previously suggested by Lambert (6) in which the CO molecule, at full coverage, is terminally bonded but tilted with respect to the surface normal alternately in the [001] and [00 $\bar{1}$] directions as one proceeds along the [110] direction.

Numerous EELS studies are in agreement that CO is adsorbed molecularly at room temperature and below. Molecular adsorption is indicated because the CO stretch frequency is observed. At low coverage two closely spaced CO stretch frequencies are observed; both are shifted to lower values than the free CO frequency. These two shifted frequencies indicate that at low coverage CO adsorbs to two different sites. The frequency shift is due to electron transfer from the bonding $5-\sigma$ CO orbital to the metal and from the metal to the antibonding $2\pi^*$ CO orbital. While two CO stretch frequencies are observed at low coverages, only the higher stretch frequency is observed at full coverage. The site assignments for the frequencies depend on the investigation - the two low coverage sites being associated

either with the top and the short bridge (7, 8, 9) or with the short bridge and the long bridge (10). These same studies associate the full coverage site with either the short bridge (7, 8, 9) or with the long bridge (10).

An infrared ellipsometric study suggests that the sites are top and short bridge at low coverage and short and long bridge at full coverage (11).

Early ESDIAD measurements (12) failed to reveal the zig zag tilt of the CO molecule suggested by the early LEED motivated models. Subsequent refinements of the technique suggested a 17° to 19° tilt (13, 14).

Experimental determinations of the electronic structure have been made by ARUPS (15) and by BIS (16). The results are consistent with tight binding calculations of the band structure for a free unsupported CO layer of $p2mg$ symmetry with alternating tilt of 15° to 20° .

Thus, while much is known about the $Ni(110)-(2 \times 1)2CO$ system from other techniques, a LEED study of the structure was warranted. Resolution of the question of the full coverage adsorption site and determination of previously undetermined parameters such as bond lengths, bond angles and metal interplanar spacing, could be answered by a LEED structural determination.

2.B: Experimental

The Ni sample was obtained from another source where it had been cut and polished to within $1/2$ degree of the (110) face. We confirmed this orientation by Laue back reflection studies. The sample was cleaned in the UHV chamber for hundreds of hours by ion bombardment at 3 keV Ar^+ , 5×10^{-5} torr at a variety of temperatures ranging from room temperature to 700 K. After annealing for 15 min at 750 K it was cooled to the experimental temperature of 125 K in 2-3 min and 5-10 L exposure of CO administered at 5×10^{-8} torr. The base pressure of the system was 3×10^{-10} torr.

Intensity data were obtained at normal incidence, this plus the minimization of stray magnetic fields was verified by the similarity of symmetrically equivalent beams.

The sequence of LEED patterns observed upon the adsorption of the CO was undetermined to $c(4 \times 2)$ to (2×1) , consistent with previous observations. The sequence of diffraction patterns stopped at $c(4 \times 2)$ if there was hydrogen contamination of the adsorbing gas, therefore care was taken to reduce this contamination. The absence of the $((2n+1)/2, 0)$ spots at normal incidence and the $(\bar{1}10)$ mirror plane confirmed the presence of $p2mg$ symmetry.

Experimental IV data was acquired for 20 beams (12 integral and 8 fractional) of which 9 beams (6 integral and

3 fractional) were inequivalent by symmetry.

2.C: Analysis

The symmetrically equivalent beams were averaged. The beams used were $(0, \bar{1})$, $(1, 0) + (\bar{1}, 0)$, $(1, 1) + (1, \bar{1}) + (\bar{1}, 1) + (\bar{1}, \bar{1})$, $(0, \bar{2})$, $(1, \bar{2}) + (\bar{1}, \bar{2})$, $(2, 0) + (\bar{2}, 0)$, $(1/2, \bar{1}) + (\bar{1}\bar{7}\bar{2}, \bar{1})$, $(1/2, \bar{2}) + (\bar{1}\bar{7}\bar{2}, \bar{2})$, $(3/2, 1) + (\bar{3}\bar{7}\bar{2}, 1) + (3/2, \bar{1}) + (\bar{3}\bar{7}\bar{2}, \bar{1})$ where the plus signs indicate which beams were averaged for the R-factor analysis. The symmetrically equivalent beams were similar in all aspects - peak position, relative peak intensities, and even absolute magnitude - the averaging performed to utilize all available data.

Since the Zanazzi-Jona R-factor calculates the first and second derivatives of the IV curves, the background intensity (which increases with energy) and any experimental noise had to be eliminated. The background was subtracted from the experimental curves by finding the line, which when subtracted from the IV curve minimized the area under the curve, with the constraint that the minimum intensity of the resulting curve was greater than zero. Experimental noise was eliminated by filtering the data through a cubic spline data smoother (17).

Theoretical calculations of the IV profiles were made using subroutines supplied by M.A. Van Hove (1). We wrote the

main programs for the structures modeled, which were tested by comparison with existing programs for simpler structures (terminally bonded CO with no tilt).

Two categories of models were tested, shown in Fig. 2-2, those which placed CO horizontally in the Ni surface troughs and those which terminally bonded CO onto high symmetry ridge sites. In all models the geometries satisfied $p2mg$ symmetry. Calculation of the horizontal models required a surface basis with 6 atoms (2 Ni, 4 average C and O) due to the close proximity of the sublayers. In these models the C and O scattering amplitudes were averaged since no preference for their orientation was expected. The terminally bonded models required three sublayers with surface basis of 2 atoms, i.e. a sublayer with 2 Ni atoms another with 2 C atoms and a third with 2 O atoms. The atomic scattering for all models tested was calculated to 5 partial wave phase shifts using often tested potentials (13). Up to 115 beams (63 integral and 52 fractional) were used in the calculation of which 62 (36 integral and 26 fractional) were not equivalent by symmetry of the (110) mirror plane. LEED calculations in the bulk were by renormalized forward scattering and those in the surface composite layer by the composite space method using matrix inversion (1).

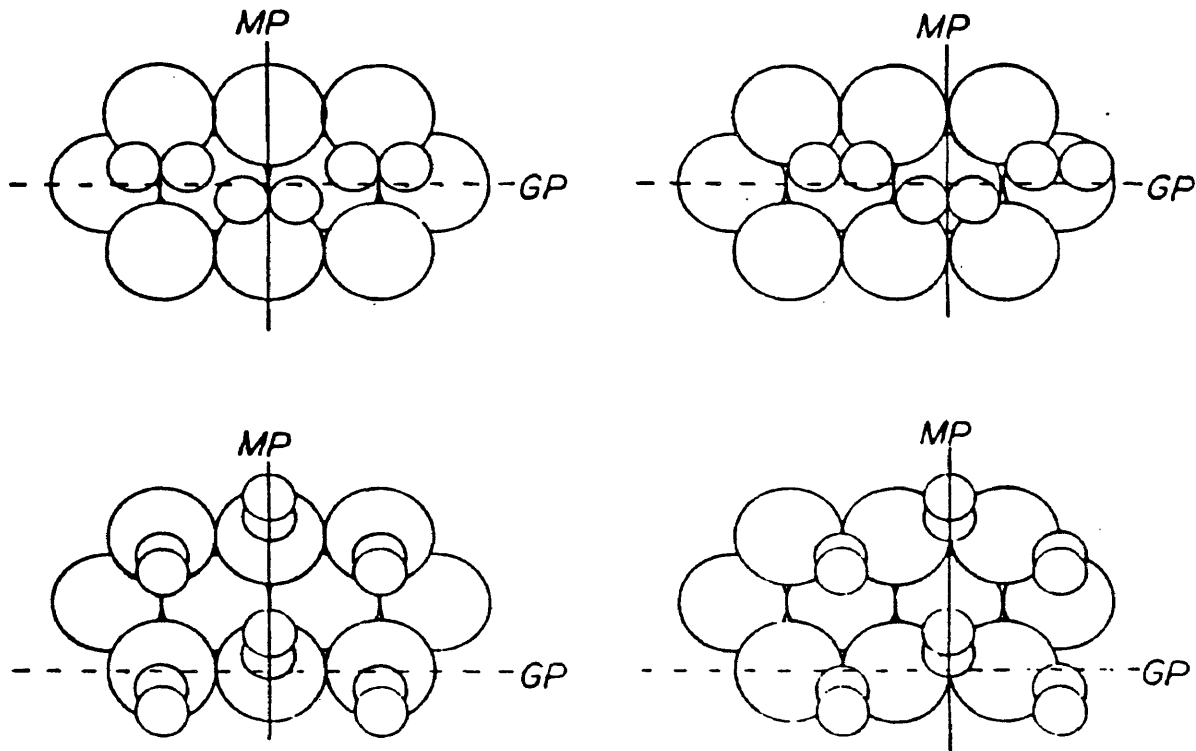


Figure 2-2. Four Structural models for the molecular adsorption of CO on Ni(110) showing the mirror plane and glide plane.

2.D: Results

Over 200 geometries were tested, all but 13 of which were for the short bridge geometry. All geometries had the ($\bar{1}10$) mirror plane and the (001) glide plane necessary for the $p2mg$ symmetry. On the basis of symmetry and tendencies noted in previous structural determinations, only some of the symmetry sites were deemed reasonable choices for the two structural models. The horizontal adsorption sites were chosen that would nestle the CO in a trough (long bridge and hollow). Terminally bonded sites were chosen which would maintain the molecule well above the metal. Initial calculations of these models yielded good visual agreement only for the terminally bonded short bridge geometry. Subsequent R-factor analysis verified this with R-factor values of low 0.2's for the short bridge and greater than 0.3's for the other geometries.

Attention was then focused on the short bridge site. For this site five structural parameters were varied: C-O bond length from 0.95 Å to 1.35 Å in 0.1 Å steps, Ni-C bond length from 1.7 Å to 2.075 Å in 0.075 Å steps, Ni-C tilt from 0° to 45° in 5° steps, C-O tilt from -10° to 35° in 5° steps and Ni-Ni first interlayer spacing at values +3%, 0%, -4% and -7% changed from bulk. All tilt angles were towards (away) the $[00\bar{1}]$ direction yielding the (001) glide plane.

If every point in this five parameter space were calculated, this would represent over 12,000 geometries. This number is too large by almost two orders of magnitude for the available computer resources, necessitating an interpretative interaction between the R-factor analysis and the choice of trial geometries.

Initially, the CO molecule was assumed to tilt with a common tilt angle from the vertical for the metal-C and the C-O bonds. A variety of contour plots of the R-factor vs. two of the parameters (see Figs. 2-3 and 2-4 for examples) facilitated the interpretation of the trends. The best geometries at this point in the analysis were in a space spanned by C-O bond lengths of 1.15 Å to 1.20 Å, Ni-C bond lengths of 1.90 Å to 1.95 Å and common CO tilts of 20° to 22°. However, our impression was that the R-factor was somewhat insensitive to the Ni-C interlayer spacing while being more sensitive to the Ni-O interlayer, as guided by the negative correlation in figure 2-4. Specifically the space spanning the R-factor minimum was for parameters giving a Ni-O interlayer spacing of roughly 2.4 Å. Less sensitivity of the the diffraction curves (and hence the R-factor) was expected for the Ni-C interlayer than for the Ni-O since the carbon layer lies underneath a full oxygen layer. Nevertheless we were concerned that this

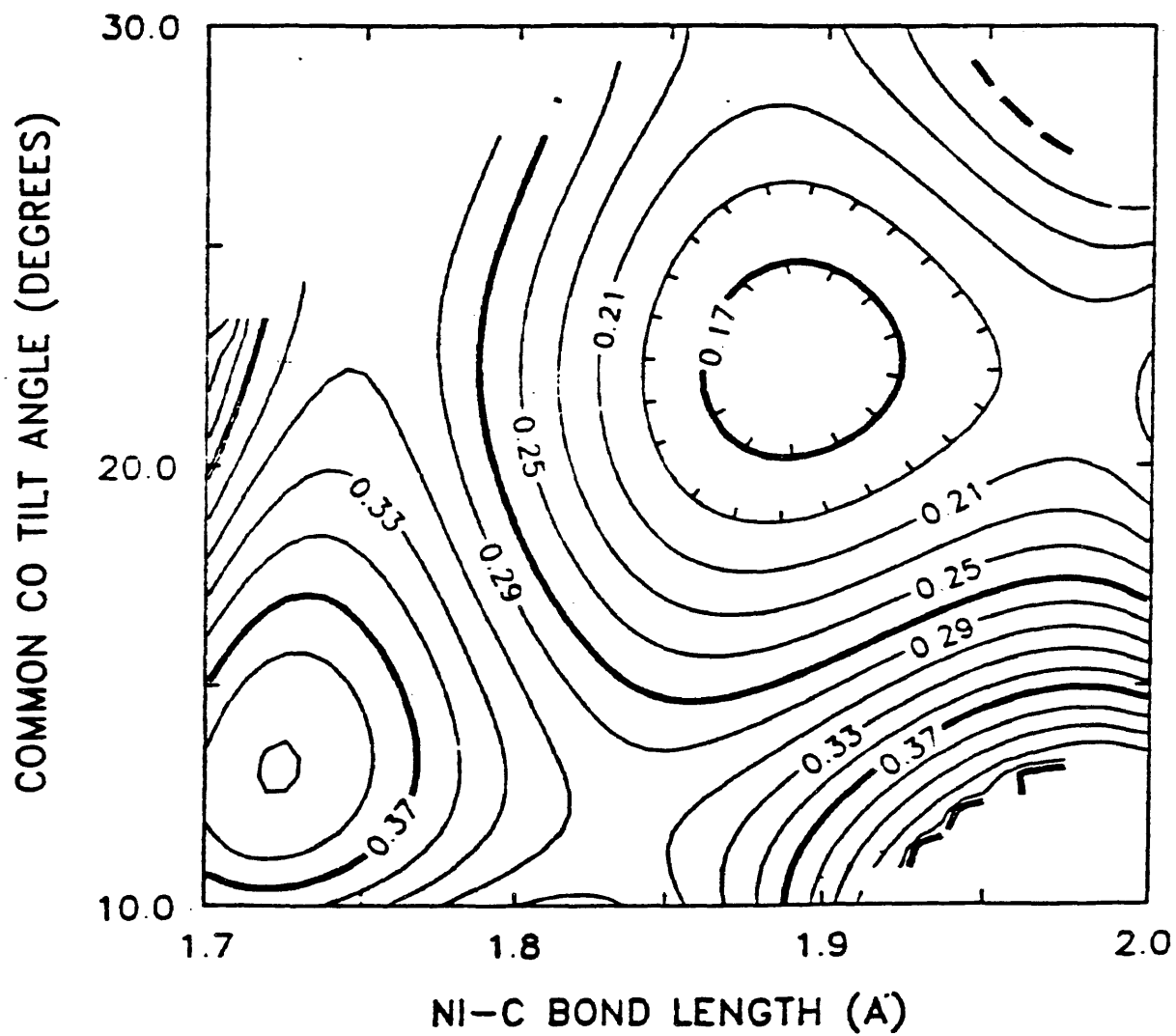


Figure 2-3. R-factor contour plot for common CO tilt and Ni-C bond length given a C-O bond length of 1.15Å and bulk Ni-Ni interlayer spacing.

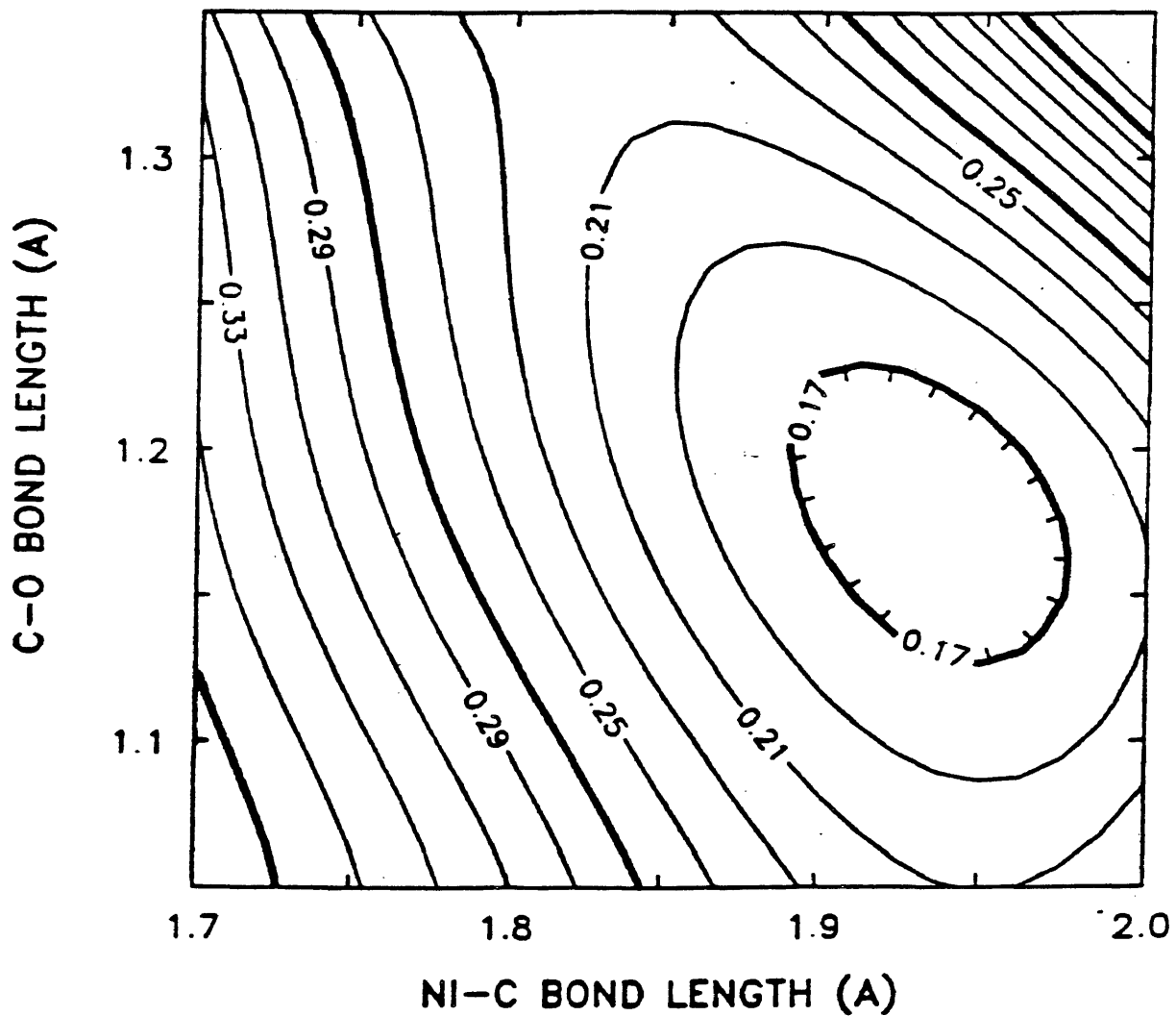


Figure 2-4. R-factor contour plot for C-O bond length and Ni-C bond length given a common CO tilt of 20° and bulk Ni-Ni interlayer spacing.

insensitivity was due to an inadequacy of our model.

The constraint of requiring common Ni-C and C-O tilts was thought to be the cause of the insensitivity. By allowing the two angles to differ the oxygen would be able to maintain a definite spacing from the nickel while allowing neighboring carbons greater freedom to distance themselves. Since repulsion of the carbons, from theoretical calculations (18), is thought to be the cause of the alternating tilt, this new model, shown in Fig. 2-5, made physical sense.

R-factor comparison of these models with experiment indicated no significant change in the optimum Ni-C bond length of 1.92 Å and C-O bond length of 1.15 Å but a preference for different tilt angles, shown in Fig. 2-6. The new "best fit" correlated to a Ni-C tilt of 27° and a C-O tilt of 17°. This minimum lying inside a long trough in the two dimensional R-factor space. The trough roughly corresponds to a Ni-O separation of 2.4 Å and an O glide of 1.0 Å. The boundaries of the valley defined by a common tilt of 22° and at a primary tilt for the metal-C of 31° and negligible C-O tilt of 5°. These boundaries represent small changes (i.e. 0.02 to 0.03) in the minimum R-factor. The shape of the valley suggests a anti-correlated uncertainty in the tilt angles. The two tilt model was tested for a

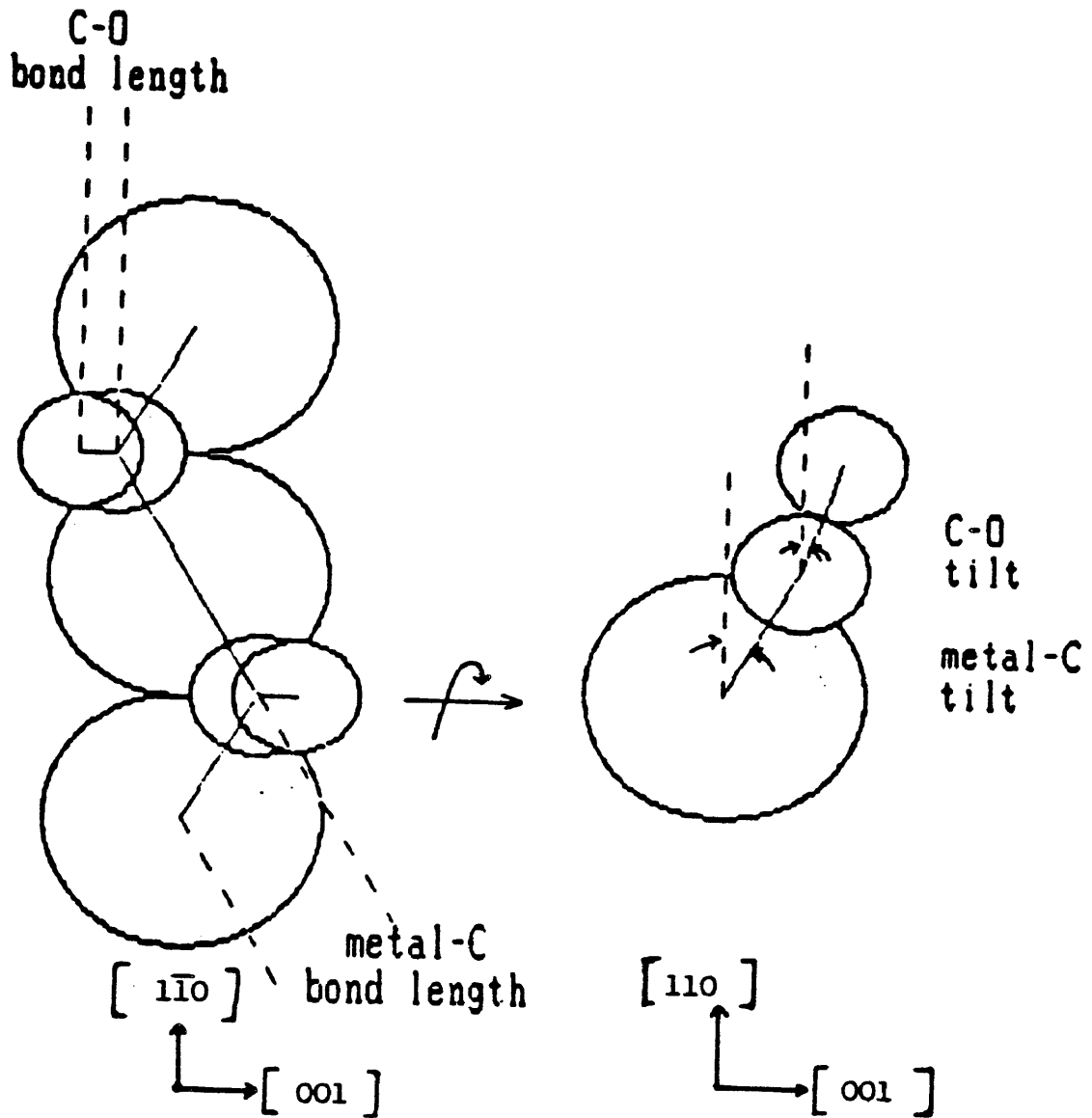


Figure 2-5. Parameters for a structural model of CO allowing different metal-C and C-O tilt angles.

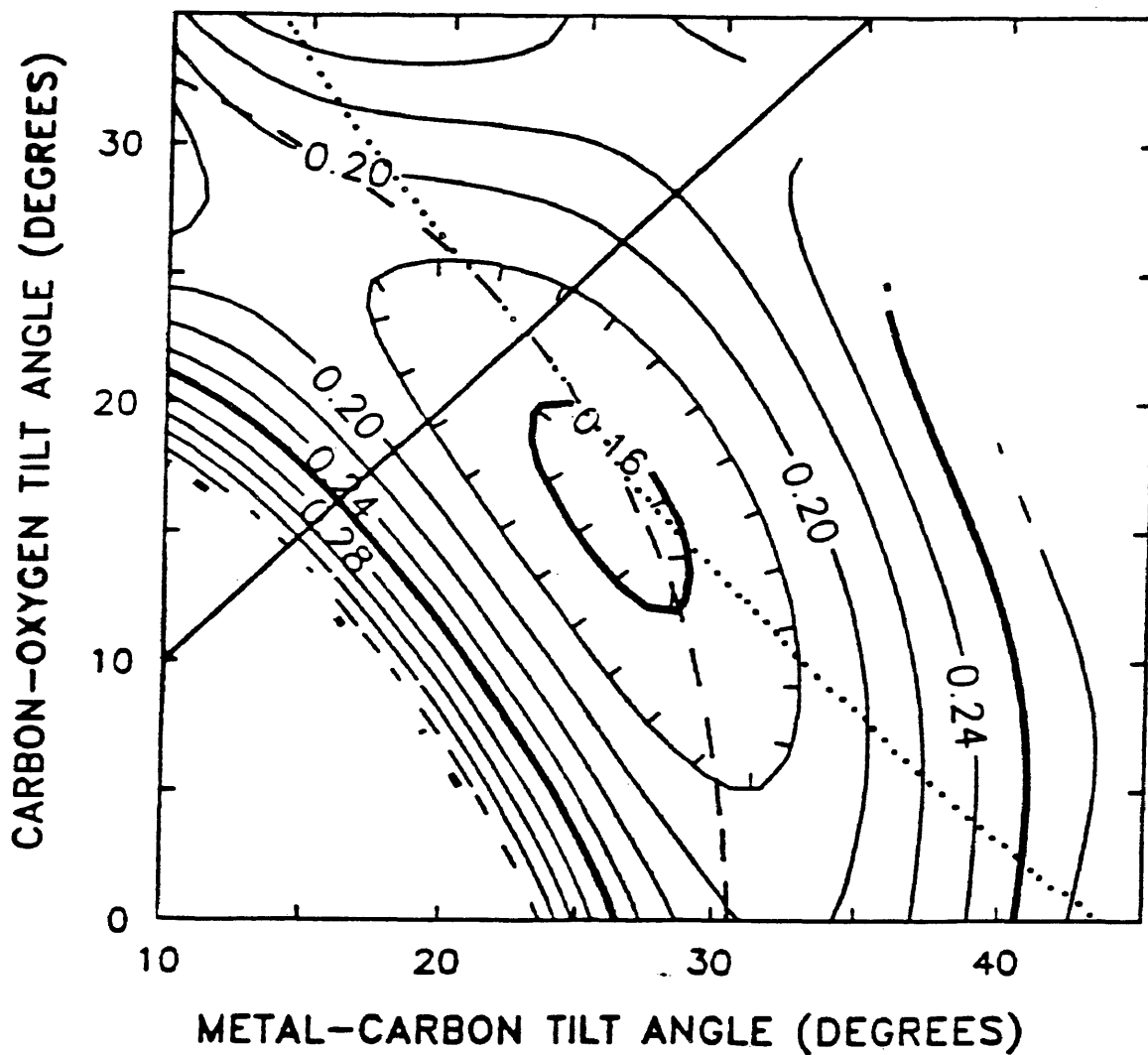


Figure 2-6. R-factor contour plot for metal-C and C-O tilt given Ni-C bond length of 1.92Å, C-O bond length of 1.15Å and bulk Ni-Ni interlayer spacing. The solid line is the equal angle common tilt line. The dashed line corresponds to a Ni-O interlayer separation of 2.4Å while the dotted line represents an oxygen glide of 1.0Å.

variety of Ni-C and C-O bond lengths about the previous minimum. The contour plots were similar to Fig. 2-6. For the bond lengths near those in Fig. 2-6 the resulting contour plots were nearly identical. Figure 2-7 is a tabulation of the R-factor minimum in the two tilt space for the range of Ni-C and C-O bond lengths tested. A two dimensional polynomial fit to this effective r-factor space gave a minimum at a Ni-C bond length of 1.95 Å and a C-O bond length of 1.12 Å. The tilt angles from the four contour plots about this minimum agreed to within 1° with values of 27° for the Ni-C tilt and 17° for the C-O tilt.

A comment about the Ni-Ni interplanar spacing seems in order. At various times in the analysis when we had "best" models we explored the effect of changing the first interlayer spacing from the bulk value. In all cases there was an increase in the R-factor indicating that the bulk value for the R-factor was closest to the optimum, at least for the case of the first interlayer. A polynomial fit to the R-factor vs. first interlayer spacing, keeping the other parameters constant, suggests a possible 1% expansion. Sampling around this minimum in all five dimensions of parameter space was not done for obvious computational reasons. However, strong correlations of the Ni-Ni spacing with other parameters were not expected, since the two Ni

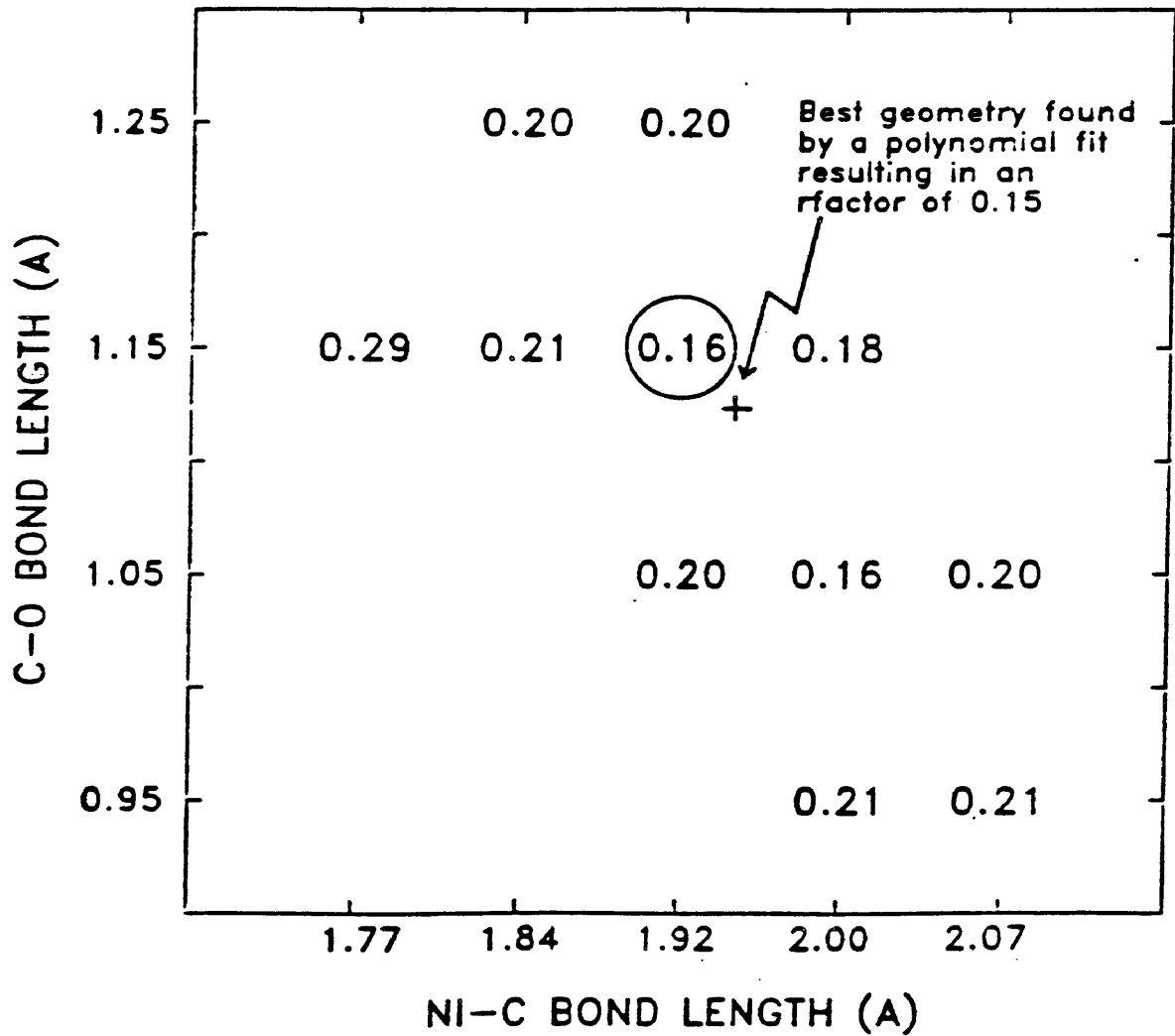


Figure 2-7. Lowest R-factors for different metal-C and C-O bond lengths upon optimizing metal-C and C-O tilts.

layers are closer to each other than to the other surface layers. In addition only a small part of the diffraction current is expected from the Ni layers, due to their depth below the top surface layer. For the same reasons variations in interlayer spacing below the first interlayer were not tested. In any case, it is most likely that upon CO adsorption to full coverage, the clean Ni multi-layer surface reconstruction is relaxed to near bulk values with possible trivial expansion. These results are in agreement with indications of MEIS investigations (19, 20).

To summarize our results, the structural model we propose for the full coverage CO on Ni(110) system at 125 K is one in which the CO is bonded as a molecule to the short bridge, via the C with a Ni-C bond length of 1.95 ± 0.05 Å. The C-O bond length is close to that of the gas phase with a value of 1.12 ± 0.05 Å. There are two tilts involved in the $[00\bar{1}]$ glide directions with values of $27 \pm 3^\circ$ and $17 \pm 3^\circ$ for the metal-C and the C-O respectively. The uncertainties in these angles may be as large as 5° assuming negative correlation between them. Finally, upon adsorption the interlayer contractions and dilations of the clean Ni(110) surface are reverted to near bulk values ± 0.02 Å. The uncertainties above correspond to 0.02-0.03 changes in the R-factor. The best value of the R-factor is ~ 0.15 but

analysis without the (01) experimental beam yields an R-factor minimum of ~ 0.12 . This beam, for which there was no symmetrical equivalent available, had poor agreement with all models tested due, perhaps, to defects in the LEED screen.

2.E: Discussion

A recent paper (21) has attempted to correlate metal-C and C-O bond lengths with EELS loss frequencies. The bond lengths determined in this study and the loss frequencies from references 7,8,9, and 10 agree very well with these correlations.

The ESDIAD (13, 14) experiments indicating a common tilt of 17° for the CO molecule measured the angular distribution of the desorbed O^+ ion. Our results indicating a 17° tilt for the C-O bond is consistent with their interpretation since they are insensitive to the metal-C bond tilt.

ARUPS studies (15) of this system base their interpretation on a tight binding calculation of a free unsupported CO layer. This calculation neglects most of the metal-C interactions and thus may be suspect in determining the metal-C tilt. However, this same study discusses the tilt in terms of the two dimensional interatomic distances. As shown in Fig. 2-8, as the tilt increases the oxygen

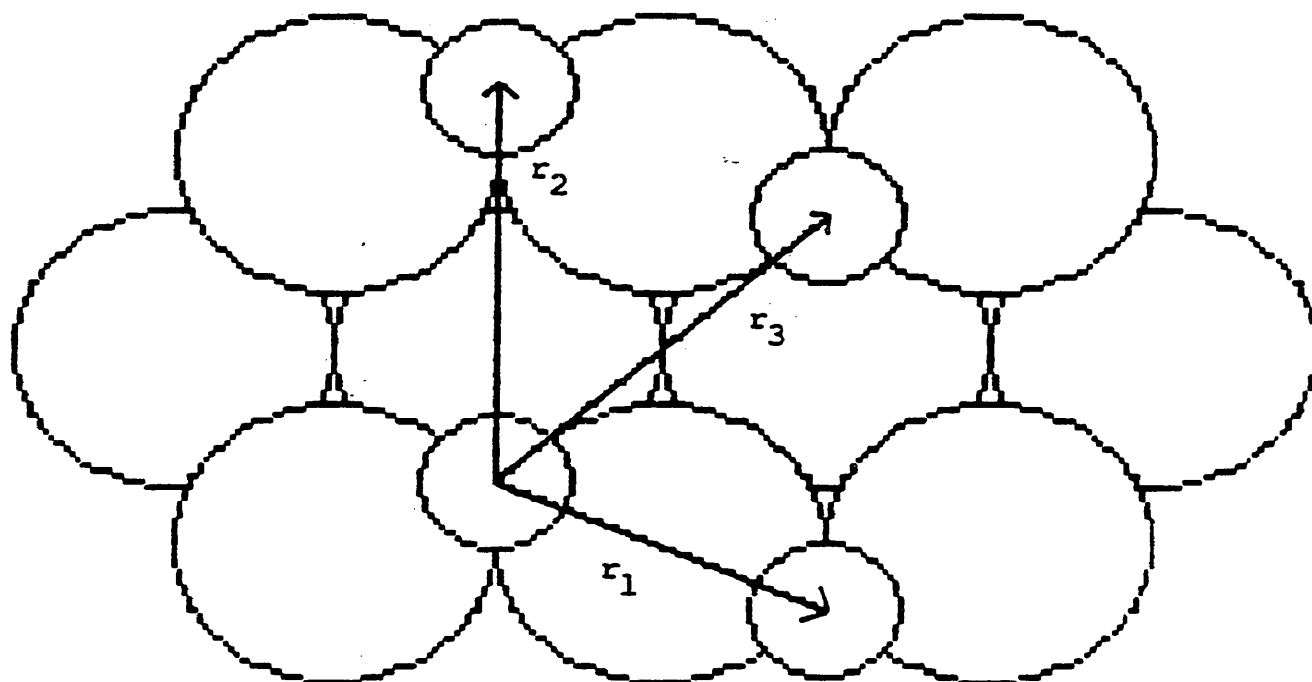


Figure 2-8. Definition of nearest neighbor distances for adsorbed atoms.

separation r_1 increases and r_3 decreases. Assuming common tilt the point at which these two distances are equal is about 17° . However at 17° the nearest neighbor carbons have a relatively small r_1 of about 2.7 Å. Based on this argument they speculate that bending the linear metal-C-O bond would lead to larger C-C separation, closer to the 3 Å value seen in other systems, while also allowing the oxygens to adjust to their optimal interatomic separations. Our model, motivated solely by the IV analysis, confirms this simple picture for the adsorption geometry. For the bond lengths and tilt angles determined in this study, the nearest neighbor carbons have $r_1 = r_3 = 3.05$ Å and nearest oxygens have $r_3 = 2.73$ Å.

Recent developments in theoretical explanations for the oscillatory behavior of variations in surface interlayers from the bulk, support the relaxation of the clean Ni(110) interlayer spacings upon the adsorption of a full layer of CO (22). Briefly, an atom in a metal prefers to inhabit a certain density of electrons due to the surrounding atoms. The atoms at the surface, however, are embedded in lower electron densities than those in the bulk. Thus the first layer contracts toward the second layer in order to increase the electron density. The second layer now has a higher electron density due to the contracted first layer, so it

dilates away from the third layer, and so on. Upon the adsorption of the gas, however, the electrons in the adsorbed species can make up for some if not all of the electrons missed by the surface Ni atoms, thus removing the impetus for the contractions and dilations of the clean surface Ni interplanar spacings.

To conclude this chapter we will make some general comments. First, further study of this system might involve the structures at low coverages of CO and the effect of temperature on both the low and high coverage surfaces. Also, the strong effect hydrogen had on the pattern indicates that coadsorption of hydrogen and CO on the Ni(110) surface may be rich in its complexity, and of interest in a variety of catalytic reactions. Finally, this study demonstrates the usefulness of R-factor contour plots for model selection of structures with a large number of parameters. The 5-dimensional grid needed to span the parameter space of this system would require 3125 points for a 4th order polynomial fit to the R-factor surface. However, by an interpretive-iterative interaction between the parameters and the R-factors, the number of grid points actually calculated was lower by more than an order of magnitude. This reduction was facilitated by correlations readily observed in the contour plots.

3. SURFACE STRUCTURE OF NO ON Ni(110)

3.A Previous Work

The NO on Ni(110) system has been studied less than its CO counterpart. The only study (the author could find) of this particular system was at temperatures above 300 K and at saturated coverage (23). Upon initial adsorption of the gas an increase in the background of the (1x1) Ni LEED pattern was observed until saturation at about 3 Langmuirs exposure. At this point a faint (2x3) pattern was observed, which did not change with temperature until dissociation of the NO molecule occurred. This intensification of the (2x3) pattern began at about 470 K. Based on this behavior they assessed the amount of initial dissociated coverage at less than 5%. This (2x3) pattern, from TDS, was ascribed to nitrogen. Upon further heating, as nitrogen desorbed, the (2x3) pattern disappeared leaving a (1x2) pattern, attributed to oxygen, which disappeared at the 1100 K TDS oxygen peak, leaving the clean (1x1) Ni(110) pattern.

Despite the scarcity of work on this (110) surface there exists several studies on other low index surfaces and on polycrystalline Ni which may yield insight into the adsorption of NO on Ni(110). In particular, polycrystalline Ni surfaces exhibit NO decomposition behavior more similar

to the (110) surface than to the closer packed (100) or (111) faces (24). This is probably due to the more open nature of the fcc(110) surface.

In an XPS and UPS study of NO on polycrystalline nickel films, Brundle (25) proposed that, at 80 K, NO chemisorbed molecularly, dissociating upon warming to 300 K, at which point the N and O atoms lie in nitride- and oxide-like electronic environments. At 80 K the $2\pi^*$ antibonding level shows a shift to a lower energy with the 5σ and 1π bonding orbitals suffering only small relaxation shifts, indicating a transfer of electrons from these bonding orbitals to the antibonding orbitals.

In another XPS study (26) of the NO-polycrystalline Ni system at high coverages, three distinct chemisorption states were identified: linearly bonded NO, bent bonded NO, and dissociated N. At 80 K the bent form of NO was predominant and upon heating the peak transferred its intensity to the dissociated N peak. If the surface was preoxidized, the bent NO did not appear and only the linear form was seen. In summary, the linear form of NO occurred only if the surface was preoxidized or deactivated by interaction with the bent NO.

The adsorption of NO on the (100) face of Ni has been studied by AES (26), SURAFS (27), XPS (28), UPS (24, 28),

TDS (24, 28), EELS (28) and LEED (24, 29). The general agreement is that at low temperatures (80-125 K) NO saturates at about 0.5 coverage in a molecular linearly bonded configuration. As the temperature increases NO dissociates leading to N_{ad} and O_{ad} in a $c(2 \times 2)$ periodicity. In a LEED structural determination of the Ni(100)- $c(2 \times 2)$ NO system at 500K it was found that the N and O randomly occupy four-fold hollow sites in the $c(2 \times 2)$ configuration. The Ni-N,O bond length was 1.7 Å and the first nickel interlayer was relaxed to the bulk value.

In AES, XPS, TDS, EELS, MQS, and LEED studies of the Ni(111)-NO system, NO has been determined to adsorb molecularly at low temperatures (125 K) (30, 31) and dissociatively at room temperature and above (31, 32, 33). The sequence of LEED patterns upon adsorption was (1×1) to $diffuse(2 \times 2)$ to $c(4 \times 2)$. Additionally, the above studies found that the dissociation temperature increased with coverage until at full coverage dissociation only occurred after the NO decomposition temperature was reached. This suggests that vacant sites are needed for dissociation of the adsorbed molecule.

3.B: Experimental

The nickel sample used in this experiment was the same

as used in the CO experiment described in the previous chapter with the same cleaning procedures used. Following ion bombardment cleaning and 15 minutes of anneal at 750 K the sample was cooled to 125 K in 2-3 minutes and 2 L exposure of NO administered at 5×10^{-8} torr. The base pressure of the system was 3×10^{-10} torr. Upon adsorption of the gas the background intensity of the clean surface (1x1) pattern increased and no superlattice spots were observed with this, or higher, exposures at 125 K. Only low temperatures were studied because we were interested in molecular adsorption. The exposure was selected because it maximized changes in the IV curves from those for clean Ni(110).

Intensity data were obtained at normal incidence, again orientation and minimization of stray magnetic fields was verified by similarity of symmetrical beams. Experimental IV data was acquired for 12 beams of which 6 were inequivalent by symmetry.

3.C Analysis

The symmetrical equivalent beams were averaged. The beams used were $(0,1)$, $(1,0) + (\bar{1},0)$, $(1,1) + (1,\bar{1}) + (\bar{1},1) + (\bar{1},\bar{1})$, $(0,2)$, $(2,0) + (\bar{2},0)$, $(2,\bar{1}) + (\bar{2},\bar{1})$, where the plus signs indicate beams averaged for the R-factor analysis. The

symmetrically equivalent beams were similar in all aspects and the averaging performed to utilize all data. Background subtraction and data smoothing was by the same methods detailed in the previous chapter for the CO data.

In the initial analysis sixteen models were tested. These geometries were generated by assuming four possible adsorption sites (top, short bridge, long bridge, and hollow) and three molecular configurations, (horizontal along the $[110]$ direction, horizontal across the $[110]$ direction and vertical) and one dissociated atom centered on the site. These geometries are shown in Figs. 3-1, 3-2, 3-3, 3-4. For these calculations a 50% NO coverage on the surface was assumed, consistent with exposure and temperature. This coverage was modeled by multiplying the input, to the analysis program, oxygen and nitrogen scattering potentials by 0.5 and placing adsorbates at every site. The resulting potentials model atoms with half of the scattering potentials of the initial N and O. Visual assessment of the IV curves and experiment, clearly showed that the horizontal molecules across the long bridge or hollow had much better agreement than did the other geometries.

Using these same programs the effect of changing the concentration of the NO on the surface was investigated.

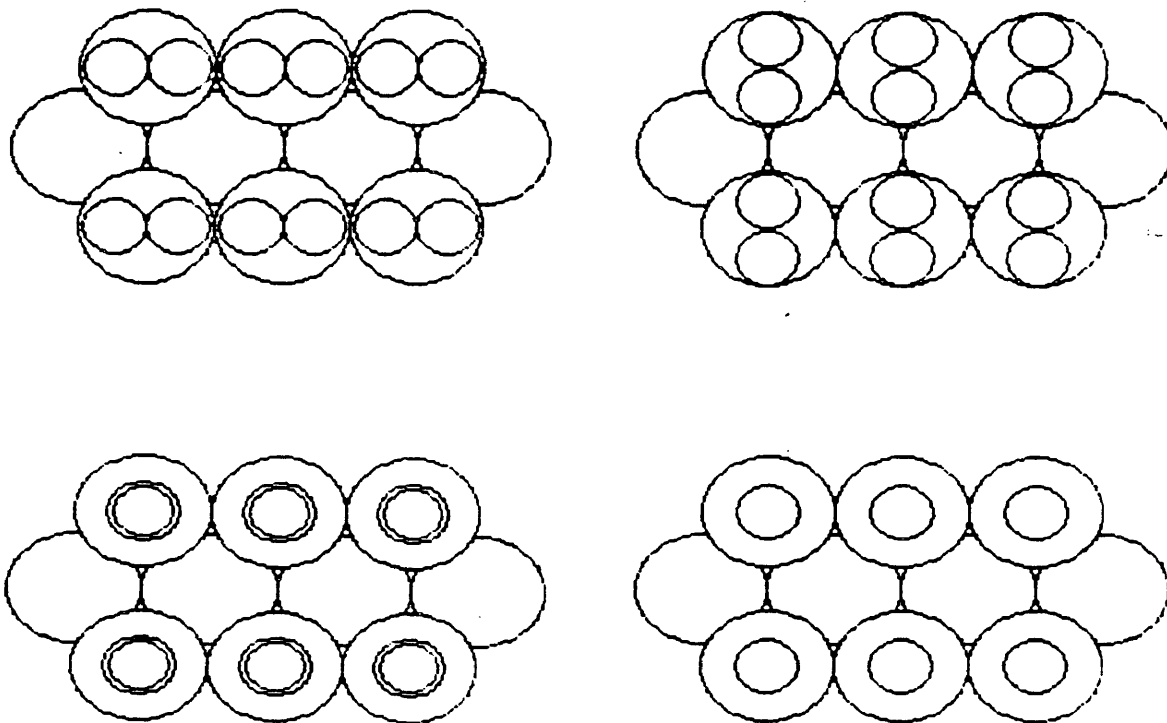


Figure 3-1. Top adsorption site models for NO adsorption. All models average the N and O scattering potentials, creating an effective NO atom.

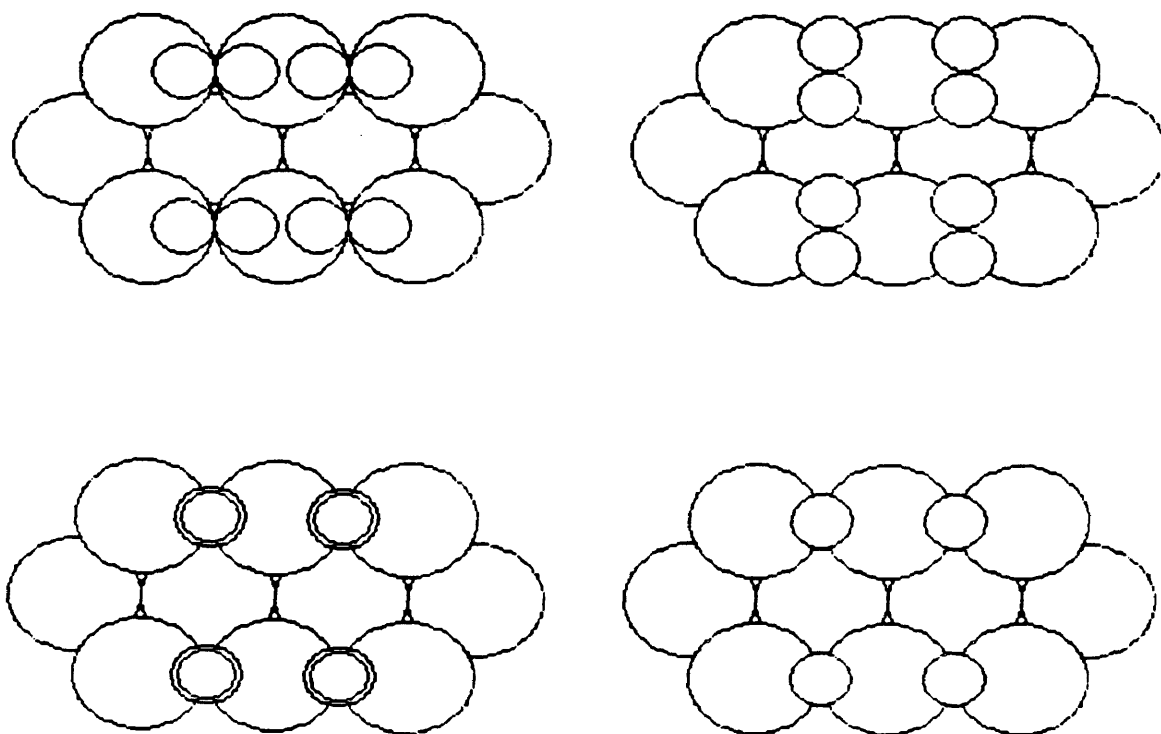


Figure 3-2. Short bridge adsorption site models for NO adsorption. All models average the N and O scattering potentials, creating an effective NO atom.

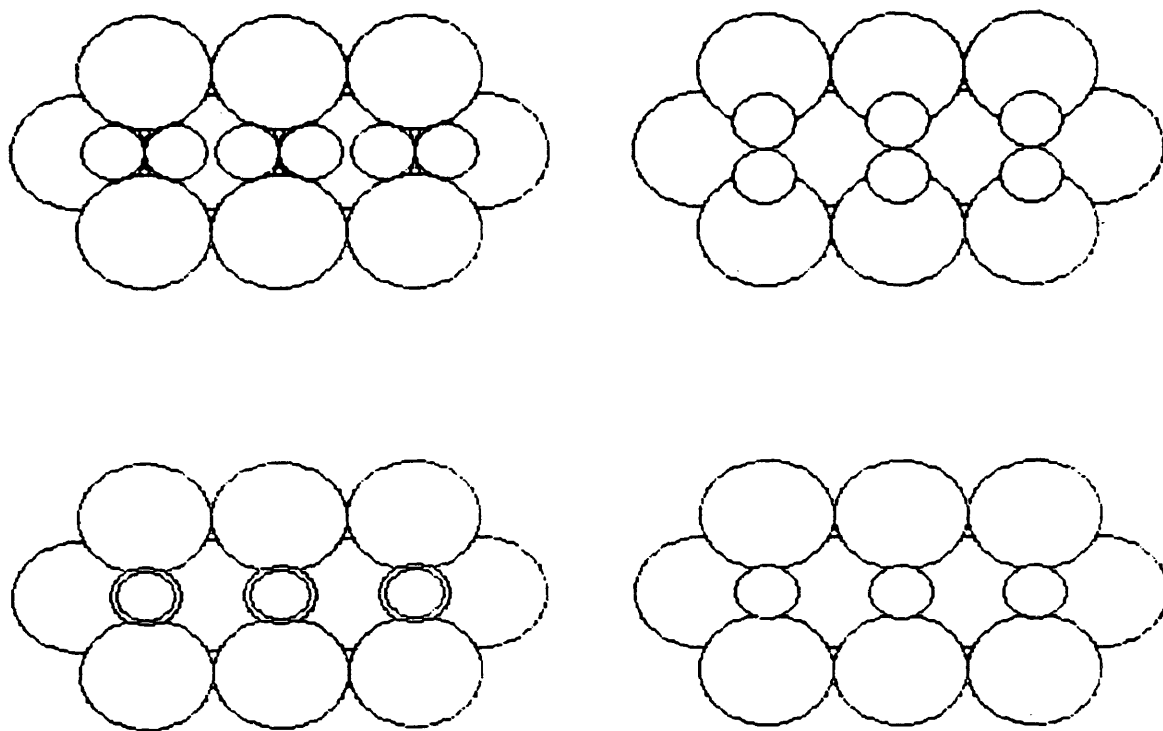


Figure 3-3. Long bridge adsorption site models for NO adsorption. All models average the N and O scattering potentials, creating an effective NO atom.

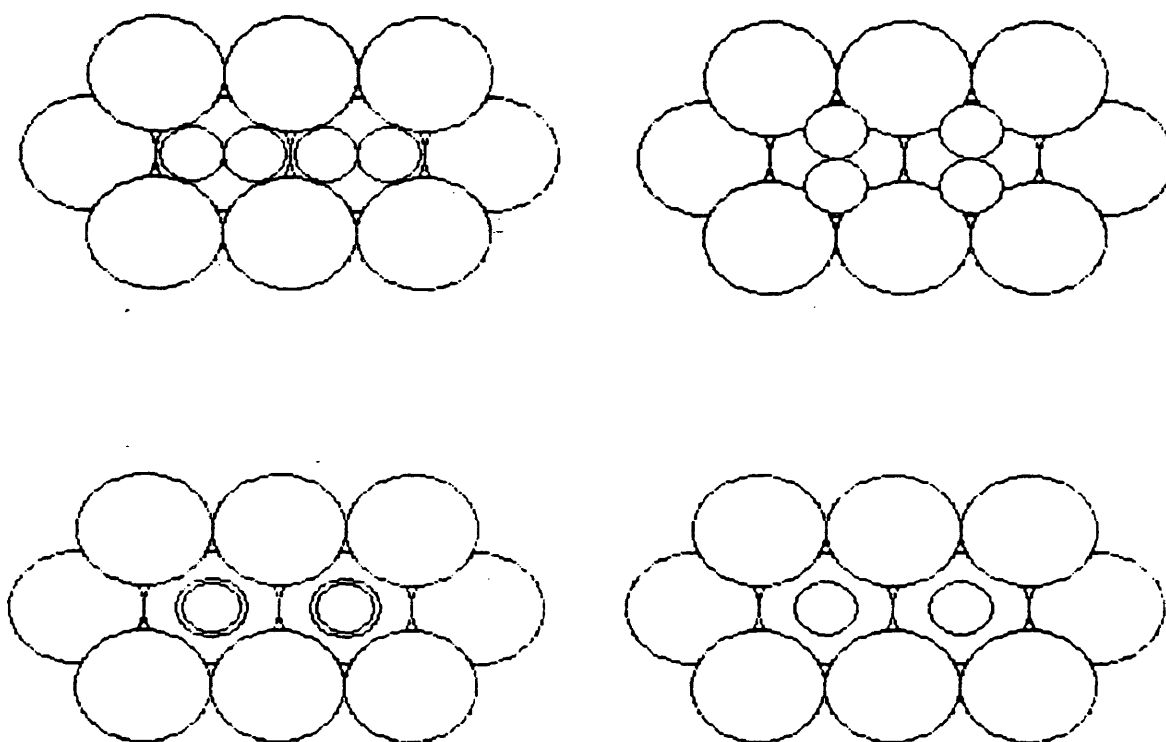


Figure 3-4. Hollow adsorption site models for NO adsorption. All models average the N and O scattering potentials, creating an effective NO atom.

Since visually the long bridge had much better agreement with the data the effect of concentration on the IV curves was tested on horizontal molecules across the long bridge geometries only. Again the concentration was modeled by weighting the scattering potentials. The change in the curves with NO surface concentration was subtle and R-factor analysis was needed to find the best effective concentration. In the range of concentration from 25% to 50% the R-factor varied by 0.003, an approximate 2% variation, with a minimum at about 40% surface concentration of NO molecules. Thus, in all further models the assumed concentration of NO molecules was kept at 40% and no further variation was tested. This is not expected to change the results due to the minimal variation of R-factor with concentration.

With the preliminary analysis completed, a new set of programs were utilized. For the horizontal models the same program used in the CO analysis was adopted, with changes in the data for the phase shifts. For vertical geometries a program using layer doubling, computationally much faster than renormalized forward scattering, was used. In fact, this layer doubling program was the standard against which the CO programs were originally tested. The (2x1) unit cell of the CO analysis was also kept, in order to better model

the 40% NO concentration on the surface, by minimizing multiple scattering effects among neighboring NO molecules. The original programs placed the NO in (1x1) sites with their scattering potentials appropriately weakened. On the actual surface the NO molecules are randomly distributed, with, we suspect, a preference for larger separation in (2x1) symmetry. Hence scattering from adjacent NO molecules (or N and O atoms if dissociated) adds only to the background and does not add diffraction features to the IV curves. To minimize the limitation in modeling such a random, but roughly uniform, distribution of NO on the surface, a (2x1) unit cell was used, and the scattering potentials multiplied by a factor of 0.8 to give an effective 40% concentration. A disadvantage of this method is that it introduces and gives non-zero intensity to fractional beams, which experimentally are not present. This may, in the case of particularly strong currents between fractional and integral beams cause problems. However, it turned out that in all cases, in the calculations, the fractional beam amplitudes were an order of magnitude smaller than the integral beams. This suggests that any such effect was minor or that, perhaps, they do exist experimentally but were unobserved.

3.D: Results

Due to the results of the Ni(110)CO system it was decided to recalculate the IV curves for the vertical molecule on the short bridge and the top site and to span a larger range of parameters. Geometries of vertical molecules on top sites with N-O bond lengths from 1.0 Å to 1.3 Å step 0.1 Å and Ni-N bond lengths from 1.7 Å to 2.0 Å step 0.1 Å gave a best R-factor of 0.21 at Ni-N and N-O bond lengths of 1.75 Å and 1.15 Å respectively. Short bridge vertical geometries were tested over the same N-O bond lengths but over dilated, in comparison with top site geometries, bond lengths expected due to the higher coordination number of this bonding site. The bond lengths ranging from 1.8 Å to 2.03 Å step 0.077 Å. The minimum R-factor of 0.21 occurring at Ni-N bond length 1.9 Å and N-O bond length of 1.15 Å. Two curious aspects of the R-factor space for these two vertical models were noted: first, the minimum in R-factor is very broad in N-O bond length with a change in R-factor of less than 0.002 over the range of N-O separation, while being very narrow in terms of Ni-N separation changing by more than 0.15 over the range; second, the respective minimums correspond to physically expected values for the bond lengths and sites. This second point may indicate the presence of some NO inhabiting these

sites mixed in with the NO described below as the correct model. A second and more mundane interpretation of the values for the bond lengths, is that for both sites, the resulting NO molecule has a Ni-N interlayer of about 1.8 Å and a N-O interlayer of 1.15 Å. These values are nearly integral multiples of the average wavelength (0.6 Å) for a low energy electron. This effect, wherein shifting scattering planes by multiples of 0.6 Å results in nearly identical IV curves is well known. In any case, the large R-factor of 0.21 suggests that these vertical geometries can be neglected.

Using the same program used for the vertical models, but with the scattering amplitudes of the N and O reduced by a factor of 100, a set of curves were run, representing a clean Ni(110) surface. The R-factor for this clean geometry was 0.21. This suggests that any model proposed as the correct geometry for this surface should have an R-factor less than that for the clean surface i.e. adding NO should increase the agreement. While this does not exclude the presence of some top and short bridge vertical NO, it suggests ignoring their possible influence in the subsequent analysis.

The analysis then focused on horizontal molecules and dissociated N and O atoms. Using the CO programs, four new

models were tested: horizontal molecules across the long bridge and in the hollow and dissociated atoms centered on the long bridge or above the hollow. In the following discussion it is easier to discuss the NO layer in terms of the separation above the first Ni layer rather than in terms of Ni-N and the Ni-O bond lengths.

The dissociated long bridge geometries centered the two atoms above the two long bridge sites in the (2x1) unit cell. The NO-Ni interlayer was varied from 0.3 Å to 0.5 Å in 0.1 Å steps, with the 0.4 Å interlayer giving the minimum R-factor of 0.18. The dissociated hollow geometries center the atoms in the hollow, with variation in the interlayer from 0.4 Å to 0.6 Å in 0.1 Å steps, the best R-factor of 0.16 occurred also at 0.4 Å interlayer. While our range of interlayers did not bracket the minimum, smaller values of the interlayer were not tried since they gave Ni-N,O bond lengths of less than 1.65 Å which are not expected physically. Note also that these dissociated geometries have an actual (1x1) unit cell. The program, which assumed a (2x1) unit cell behaved as expected with the intensities of the fractional beams six orders of magnitude smaller than the integral beam intensities. These results for the dissociated atoms foreshadow the final result. Atoms centered on the hollow are nearer to the actual atomic

positions, than are the atoms centered on the long bridge.

Initial geometries for the long bridge and hollow molecular adsorption sites varied the Ni-NO interlayer from 0.4 Å to 0.6 Å in 0.1 Å steps and the N-O bond length from 1.2 Å to 1.3 Å. The results showed that in both cases the best interlayer was 0.4 Å but that the correct N-O bond length had not been found. The results for the long bridge site indicated preference for larger bond lengths than had been tried, while the hollow site results had a preference for shorter bond lengths. The long bridge site had a "best" R-factor of 0.15 as opposed to the hollow best value of 0.18. Note, that a N-O bond length of 1.25 Å places the N or O atoms in the same position with respect to the Ni surface. Similarly a 1.3 Å long bridge N-O bond length places the atoms in the same position as a 1.2 Å N-O bond length hollow geometry, and so on. Thus an indication of a longer N-O bond length in the long bridge and a shorter N-O bond length in the hollow is motivated by placing the N and O atoms in the same definite relation with respect to the Ni surface. The bond length and interlayer, for the long bridge geometries, were thus varied until the minimum in the R-factor was found. For comparison some equivalent, with regard to N and O position with the Ni, hollow geometries were tested, in all cases the long bridge had lower R-

factors than did the hollow geometries. The minimum occurred for a Ni-N,O interlayer of (0.4 ± 0.03) Å and a N-O bond length of (1.45 ± 0.15) Å, where the uncertainties correspond to a 0.02-0.03 change in R-factor. The R-factor minimum corresponding to these parameters was 0.12. The contour plot for these horizontal long bridge geometries is shown in Fig. 3-5. The large uncertainty in bond length is not unexpected since LEED is most sensitive to vertical separation between atoms and less sensitive to horizontal separation. In addition this insensitivity to N-O bond length may be due to another factor which could not be easily tested and that is unsymmetrical adsorption across the bridge. If the NO binds across the long bridge in such a way that one of the atoms is closer to the bridge than the other atom the result, due to different domains, would be an effective uncertainty in the bond length. Due to the disordered nature of this system, however, such an asymmetrical binding could not be determined. The uncertainty in our results places an upper limit on the asymmetry of 0.075 Å.

The trend in which molecules centered over the long bridge or hollow had a minimum corresponding to placing the atoms in definite positions relative to the Ni substrate lead to the possibility that dissociated atoms inhabited

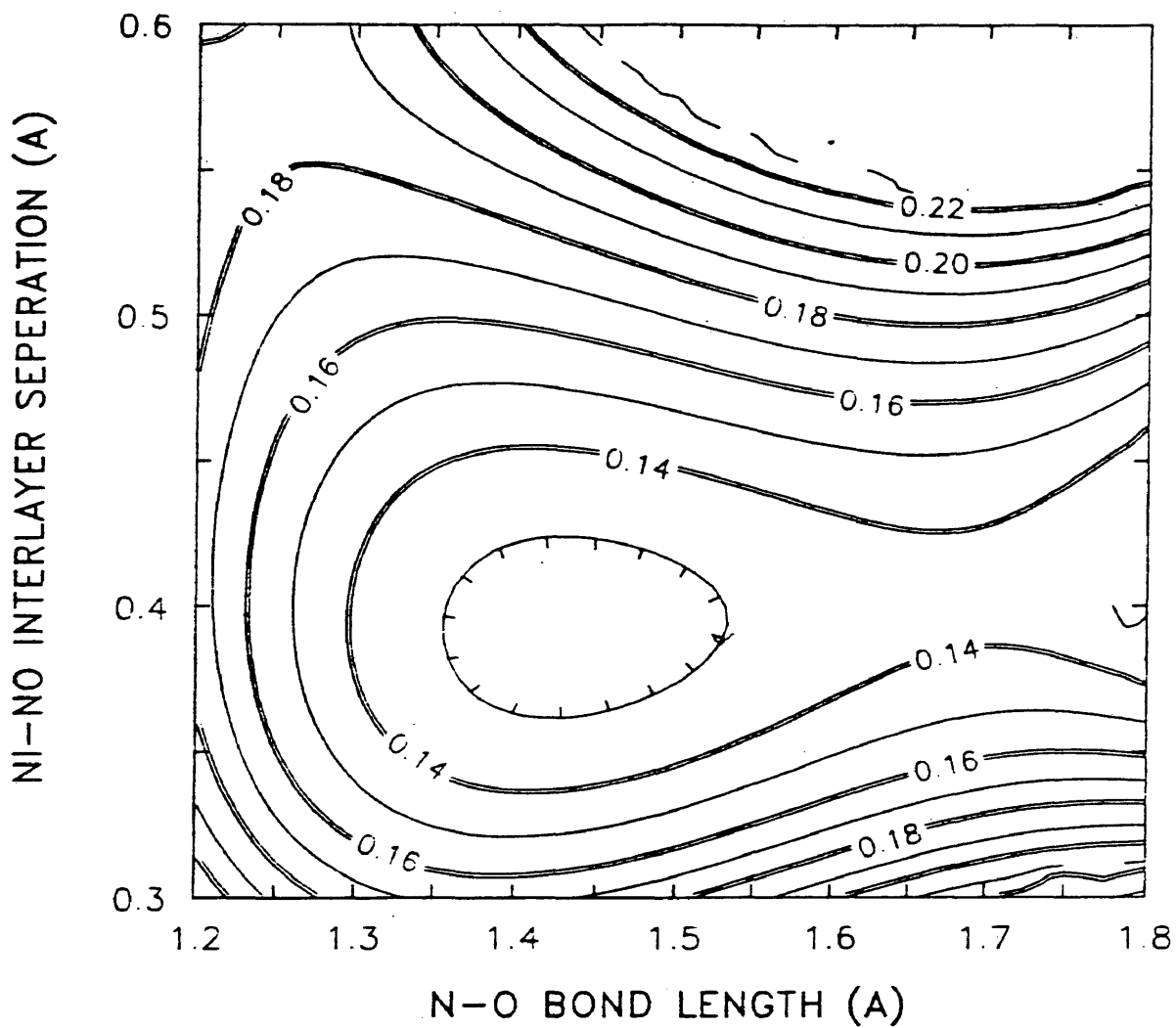


Figure 3-5. R-factor contour plot for Ni-NO interlayer and N-O bond length given bulk Ni-Ni interlayer spacing. This contour plot is for the molecular long bridge adsorption site geometry.

these positions. Thus, geometries in which dissociated atoms were placed in these positions were tested. The resulting R-factors while less than the equivalent hollow molecular values were, on average, 0.02 higher than the long bridge results and in all cases higher. Clearly multiple scattering between the neighboring N and O atoms defining the molecule is needed. To demonstrate the agreement of the theoretical IV curves and experiment and the subtlety of the change with geometry, IV curves are shown in Figs. 3-6 and 3-7. The geometries shown in these two figures are the molecular long bridge (N-O bond length = 1.4 Å, Ni-NO interlayer = 0.4 Å), molecular hollow (N-O bond length = 1.1 Å, Ni-N,O interlayer = 0.4 Å), dissociated NO placing the atom in the same position as the long bridge and hollow molecules, and the clean Ni(110) surface.

To summarize the results, NO at approximately 0.4 coverage and at 125 K adsorbs molecularly in a horizontal configuration across the long bridge with a Ni-N,O interlayer of (0.4 ± 0.02) Å. The N-O bond length is dilated from the gas phase value of 1.15 Å and has a value (1.45 ± 0.15) Å. These values result in a Ni-N,O bond length of 1.72 Å. Preliminary analysis indicated that the first Ni-Ni interlayer relaxed to the bulk value upon adsorption of the gas and in subsequent geometries was not

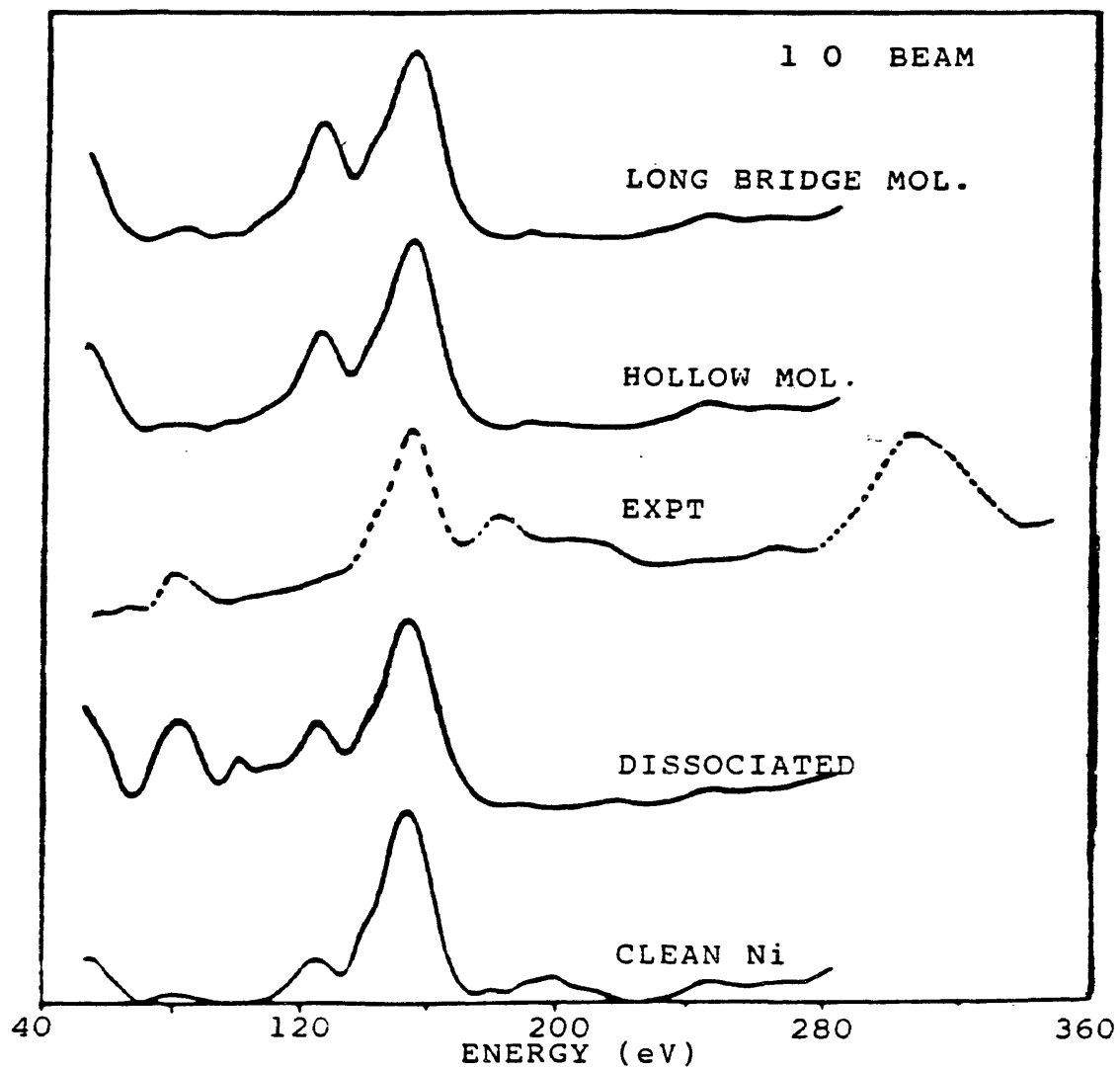


Figure 3-6. IV curve for the (10) beam for the clean Ni surface, dissociated NO, molecular NO on the hollow site, and molecular NO on the long bridge.

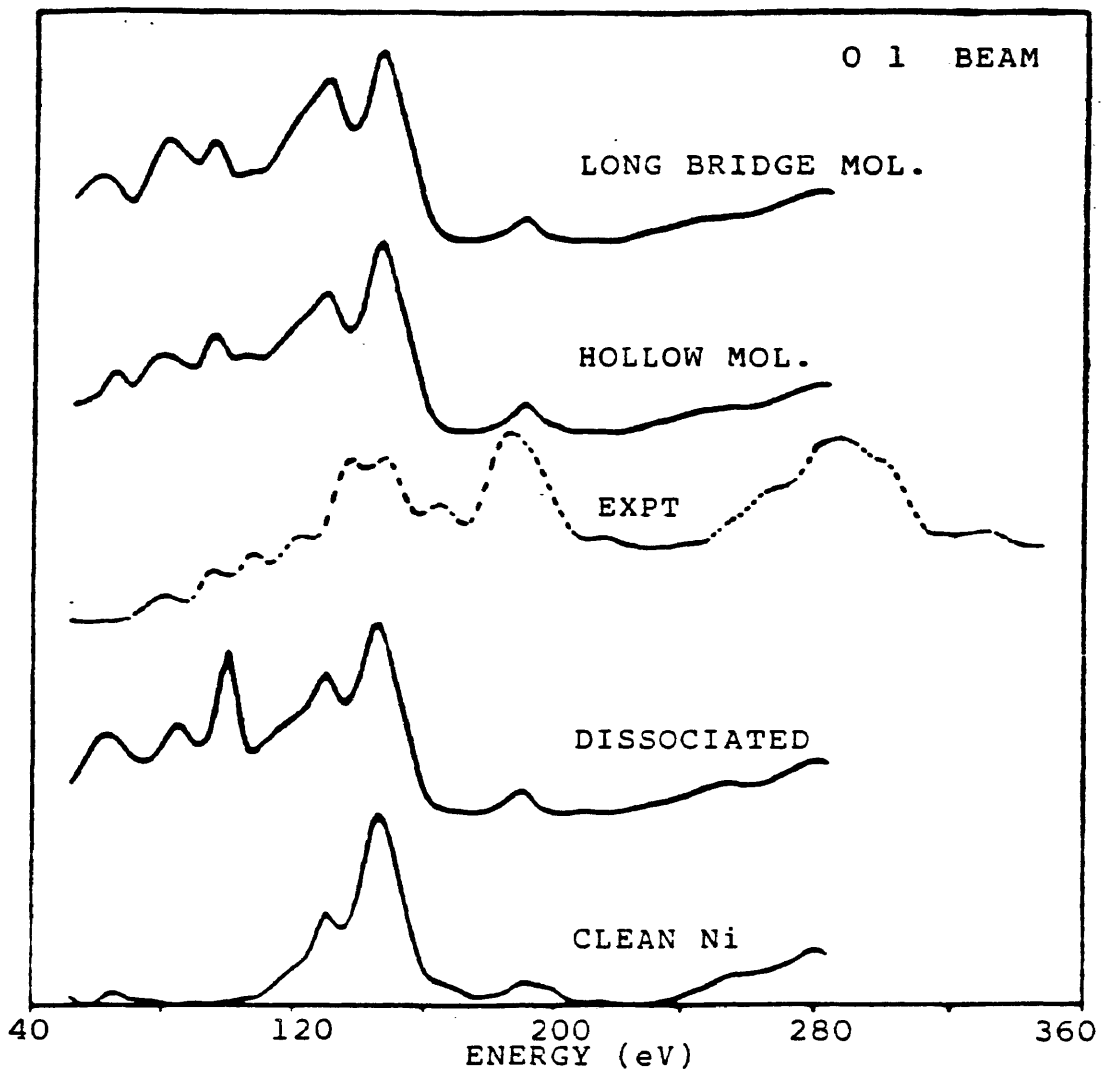


Figure 3-7. IV curve for the (01) beam for the clean Ni surface, dissociated NO, molecular NO on the hollow site, and molecular NO on the long bridge.

varied. To help visualize the adsorption geometry, the results are shown in Fig. 3-8.

3.E: Discussion

In their study of the Ni(110)-NO system, Price et. al. (23) suggest that dissociation of the NO is aided by vacant sites on the surface. They present the NO on W system as a model in which the molecule uses vacant sites to lie down and bind to two sites before dissociating. From their data on the Ni(110)-NO system, they were unable to draw such a conclusion. Additionally this same behavior is observed in the Ni(111)-NO results summarized above. Our results are consistent with such a vacant site model of dissociation. The 40% surface coverage of NO results, on average, with at least one adjacent vacant site per molecule. In addition the model proposed above requires a vacant site for each molecule, since the dilated N-O bond would place neighboring molecules closer than the atoms in the adsorbed molecule (i.e. the N-O bond length). This dilation of the bond from the free molecular value suggests that adsorption in this site is precursive to dissociation.

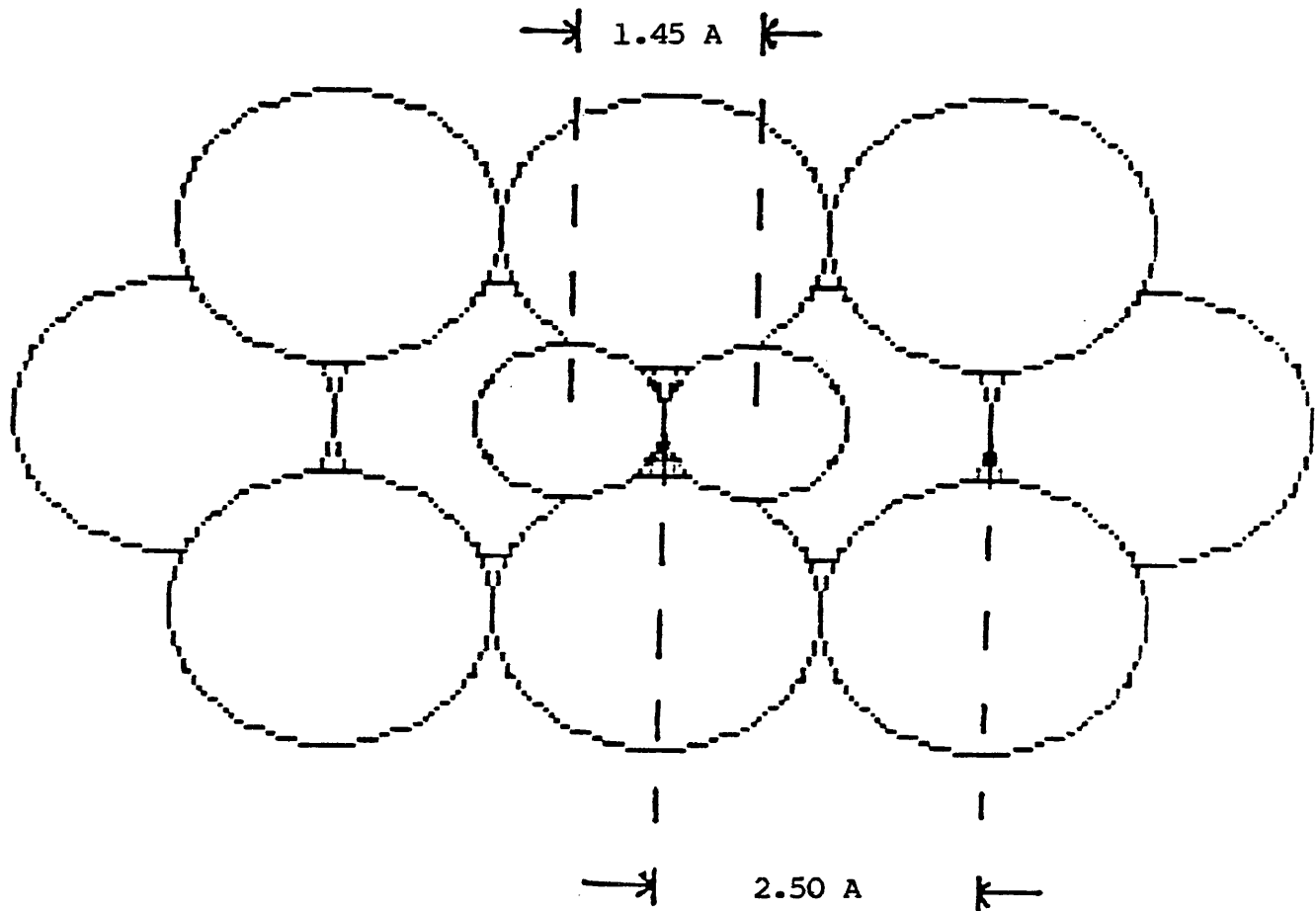


Figure 3-8. Structure of the Ni(110)-NO system as determined by LEED.

4. SAMPLE PREPARATION

4.A: Composition

The brass sample used in these experiments was prepared at RPI (34) and as received the brass sample was of composition Cu-27%Zn-7%Al (atomic percentages) with M_s of approximately -30°C . Following the LEED experiments the brass composition was measured by WDS on two different pieces of the original sample. The first piece had undergone only polishing, while the second piece had additionally undergone the in situ cleaning procedures, both procedures detailed below. Fig. 4-1 shows representative WDS spectra for the brass samples. The composition was measured at three locations on each sample. The results are shown in Table 4-1. The sample which had been in the chamber was found to contain 3.2% less zinc and 3.2% more copper than the sample which had not been under high vacuum and the ion bombardment cleaning procedures. This suggests that zinc may have evaporated from the surface while in the chamber. Since the WDS measurements probes thousands of angstroms into the bulk, this small change in composition may be greatly exaggerated at the surface. The other curious aspect in the WDS measurements is the discrepancy between the composition as measured and the composition

TN-5500 Colorado School of Mines / JEOL FRI 15-JUL-88 14:30
Cursor: 0.000keV = 0 ROI (1) 0.000: 0.000

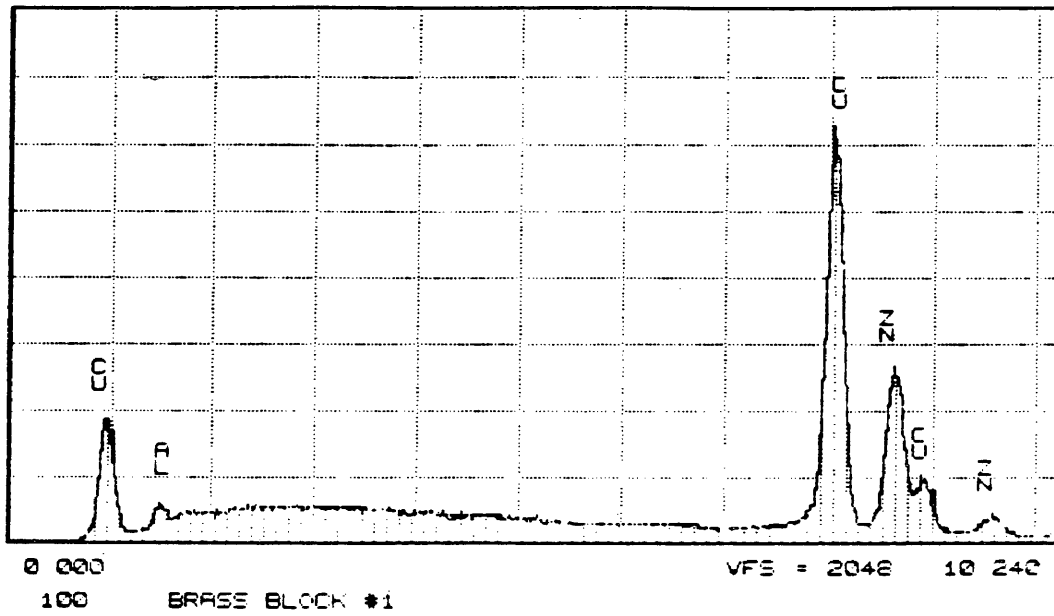


Figure 4-1. Representative WDS spectrum for a CuZnAl sample.

Location	1 (AT%)	2 (AT%)	3 (AT%)	AVG (AT%)
Brass				
Polished				
Cu	62.05	62.87	62.88	62.60
Zn	33.80	33.45	32.94	33.40
Al	4.15	3.68	4.17	4.00
Polished+ In Situ Clean				
Cu	67.01	65.39	64.93	65.78
Zn	29.27	30.34	31.09	30.23
Al	3.72	4.27	3.97	3.99
Steel				
Polished				
Fe	67.17	68.17	68.02	67.79
Ni	32.83	31.83	31.98	32.21
Polished+ In Situ Clean				
Fe	67.71	66.86	67.17	67.15
Ni	32.29	33.14	32.83	32.75

Note: The chi squared statistic of the fit of the above compositions to the WDS spectra varied from 0.93 to 1.51.

Table 4-1. WDS composition results.

expected. This discrepancy may be due to preferential etching of the constituents during the electropolish.

The FeNi sample was received with a composition known only to be >30% Ni. Again WDS measurements were performed on two pieces: the first had been polished before receipt of the sample but untouched by our cleaning procedures, the second piece had been polished and undergone the high vacuum cleaning procedures detailed below. Representative spectra for the two pieces are shown in Fig. 4-2. The results, shown in Table 4-1, indicate that the composition of the sample was virtually unchanged by the sample preparation. The composition of the sample was Fe-32.5%Ni.

The M_s temperature of FeNi alloys is highly sensitive to nickel composition. A Ni concentration of 32.5% corresponds to a M_s of 110 K while an uncertainty of 1% in the composition results in a change of over 70 K in M_s (35). Thus measurements were made to determine M_s as nearly as possible, to prevent inadvertent inducement of the transformation. A lower bound of 77 K was found by simply immersing the sample in liquid nitrogen and observing the formation of martensite plates. In an attempt to obtain an exact value for M_s resistivity vs. temperature measurements were attempted, since the resistivity of a FeNi sample is known to change sharply at the transition (36). This method

TN-5500 Colorado School of Mines / JEOL FRI 15-JUL-88 13:49
Cursor: 0 000kev = 0 ROI (1) 0 000: 0 000

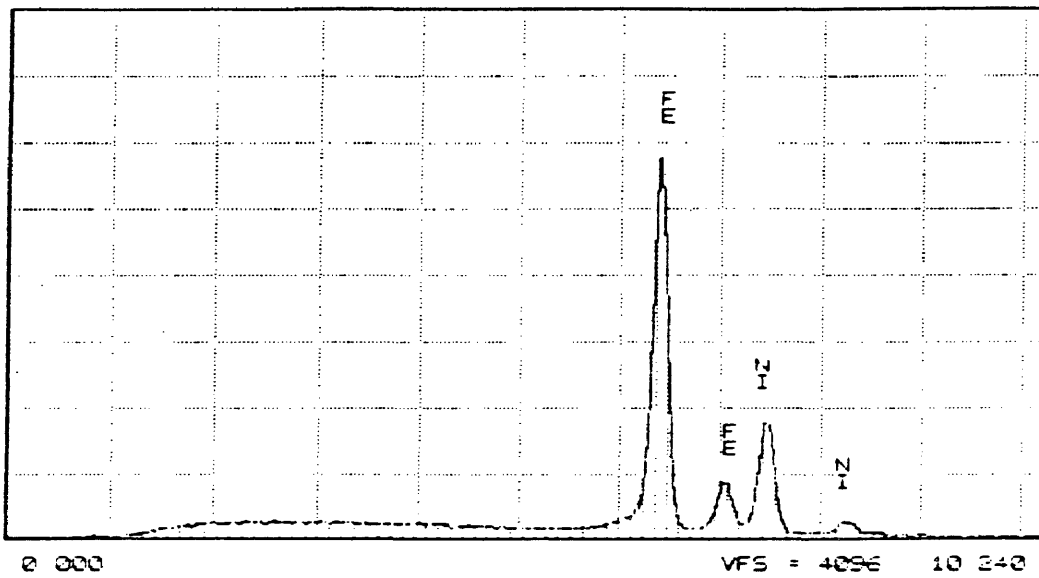


Figure 4-2. Representative WDS spectrum for a FeNi sample.

was unsuccessful due to instrumentation limitations. Thus, the sample was slowly cooled and formation of martensite visually determined. The results, while crude, placed M_s between 100 K and 160 K, consistent with the measured composition.

4.B: Orientation

The FeNi and CuZnAl samples were received in the form of unoriented single crystals, and the first step in preparing the samples for the LEED experiments was to orient and cut them to the crystal surfaces desired. The standard procedure for orienting a single crystal is to use Laue Back Reflection X-Ray photography (37). Using the Back Reflection photograph there are several methods which can be used to orient a sample. Among the more common are plotting the x-ray poles on a Wulff net and either comparing to standard projections or measuring the angles between the poles and comparing to known angles.

Initial efforts to orient the CuZnAl sample with either of these two methods were unsuccessful and it was decided to develop a more systematic method of orientation. The results were two BASIC computer programs, see Appendix A. The first program generates a set of standard projections, plotting the low Miller index poles, allowing for beams

extinguished by the structure factor. The second program takes the poles from a Laue photograph and plots them on a stereographic projection. Orientation is achieved by calculating the stereographic projections resulting from rotating the poles to the center and comparing to the standard projections. The hope is that one of the poles from the Laue photograph will be a low index spot and easily identified. In all four attempts with this method, the sample was oriented with just one Laue photograph and approximately an hour running the programs and comparing against the standard projections. An orientation is double checked by identifying as many spots as possible in the Laue photograph. Not all spots are easily identified since some may correspond to high Miller indices which may not be plotted on the standard projections.

The precision to which an orientation was determined was of primary concern. The goniometer and camera setup initially available turned out to be inadequate. The CuZnAl sample could only be oriented to the (110) surface to within $\pm 1.5^\circ$. In LEED the typical precision desired is $\pm 1/2^\circ$. This inability to orient the face to better accuracy was thought to be a possible cause of discrepancies in the CuZnAl LEED pattern, detailed below, and a new x-ray sample and film holder were needed. With the availability of a new

Polaroid x-ray camera and the machining of a sample holder to attach to the camera, the accuracy of the orientation was increased to better than $1/2^\circ$. The camera and sample holder were aligned by sighting a laser beam through the camera and onto the sample, reflective enough to act as a mirror. By adjusting three alignment screws the beam could be reflected back along the incident beam. The alignment of the sample and film plane, using this method, was determined to be better than $1/4^\circ$. This was checked by taking a Laue photograph of a sample of known orientation. The result was accurate to within less than the targeted $1/2^\circ$. Using this camera the FeNi sample was oriented to the (111) face $\pm 1/2^\circ$.

4.C: Polishing

Using the above method to determine the crystal orientation the CuZnAl and FeNi samples were then cut to within a few degrees of the desired face using a diamond wafering saw. This was followed by roll grinding from 240 grit to 600 grit in four stages. Polishing was done with 1 micron alumina and a finish polish of 0.05 micron alumina. For the brass sample the polishing solution contained dilute HF (which was safe on hands). Following the final polish, both samples were highly reflective and unscratched to the eye. Final orientation was done by machining a

grinding/polishing holder for the sample and repeating the grinding and polishing steps to orient the sample the final few degrees to the desired face.

The brass sample was then electropolished to remove any damage to the surface caused by the mechanical polish. The electropolishing was in a 5:3:1 phosphoric acid : ethanol : H₂O solution under a current density of approximately 30 mAmps for 90 secs (38). The sample was held parallel to the electrode and the solution stirred during the polish to minimize inhomogenities. Immediately after the etch the sample was rinsed in distilled water. The result was a sample with a deeper and somewhat darker shine than before the electropolish.

The FeNi sample was not electropolished or etched due to concern about pitting of the surface (39).

4.D: In Situ Cleaning and Annealing

After placing the samples in the chamber cleaning and annealing procedures had to be developed. The CuZnAl sample in particular, required extensive experimentation in developing cleaning procedures due to the high vapor pressure of zinc.

This high vapor pressure of zinc required that care be taken not to expose the brass samples to high temperatures

(>150°C) (40). Even during bakeout of the chamber the sample had to be cooled by pumping water through the cooling tubes.

A variety of argon ion bombardment cleaning procedures were tested to produce the best pattern. The restriction of avoiding high temperatures ruled out annealing the sample to remove the damage caused by the ion bombardment. Thus the sample had to be bombarded at energies high enough to sputter clean the surface yet low enough to minimize damage. The incident argon energy was varied from 100 eV to 3000 eV with the best results seeming to occur in the range 500-1000 eV. The effect of bombarding at 500-1500 eV and then lowering the energy to 100-250 eV for 10-30 minutes, in an effort to remove the ion damaged surface, was also tested with disappointing results. The effect of the bombardment rate was also investigated by varying the Ar partial pressure and/or the ion gun beam current, this was determined to have undetectable effect on the LEED pattern.

In addition the effect of annealing at low temperatures (<200°C) was also investigated. In all cases annealing for up to 1 hour had, at best, no effect on the pattern. In addition the effect of temperature on the sample was non-reproducible from sample to sample. In one sample the temperature could be raised to 150-200°C before the pattern

disappeared after 5-10 minutes. For the other brass sample tested the temperature at which the pattern faded was 100°C. In both cases the pattern could be recovered by further ion bombardment.

To summarize the procedure developed to clean and obtain the best pattern for the CuZnAl samples was several hundred hours of Ar⁺ ion bombardment at $1-5 \times 10^{-5}$ torr Ar (chamber pressure was 7×10^{-10} torr). The beam energy ranged from 500 to 1000 eV with current 15-25 mA.

The FeNi samples were much easier to clean. On the basis of procedures developed for pure nickel and iron, (8) and on FeNi samples of different compositions, the FeNi sample was cycled through dozens of cleaning and annealing cycles for hundreds of hours at 5×10^{-5} torr Ar⁺, 500 eV and 20 mA current at room temperature. The annealing stages were at 650-850 K. Following an AES measurement of the sample which indicated the presence of sulfur, in addition to the iron and nickel (following the above cleaning) the sample was then bombarded, at the same parameters but at 200°C for nearly one hundred hours. This procedure is known to remove sulfur from pure iron and nickel crystals (9), unfortunately problems with the Auger system prevented measuring the results of this ion bombardment at elevated temperatures.

The procedure to obtain the LEED pattern was to bombard the sample at 5×10^{-5} torr Ar followed by a 10 min anneal at 750 K and then cooling to the experimental temperature.

5. SURFACE STRUCTURE OF β CuZnAl

5:A Motivation

The main evidence for a surface martensite phase in β -phase alloys comes from electron diffraction studies. Two main effects are seen in Transmission Electron Diffraction (TED) patterns of these alloys. They are diffuse streaks in definite crystal directions and the appearance of extra maxima. This brief discussion of the literature is not intended to be a comprehensive review, but instead to present some of the evidence for and the debate about a surface martensite phase.

Wayman (41) attributed the diffuse streaks to low frequency TA phonon modes. In a more recent study (42) the diffuse streaking has been determined to be a sub-surface phenomenon due to both static and dynamic (phonon) displacements of atoms. In a different approach, Finlayson (43) has described the streaking in terms of a Kohn anomaly interaction between the electrons and phonons.

Of, perhaps, more interest to this study is the occurrence of extra maxima in the the diffraction patterns of a variety of β -phase alloys. Michal (44) has attributed the extra maxima in TiNi alloys to lattice displacement waves which he thought to be a true premonitory effect to

the subsequent transformation. In β -Brass alloys, Lovey (45) determined the extra maxima arose from the coexistence of 18R, 9R and 2H phases with the β phase. Lovey also found a surface specificity in the appearance of the maxima. The greatest sensitivity was found at the (110) surface with the (100) surface exhibiting no extra spots. This sensitivity has also been found in a neutron and x-ray diffraction study of Cu based β -phase alloys. The anomalous peaks in neutron and x-ray diffraction patterns was attributed to a Lattice Modulation Wave shifting the $\beta(110)$ planes in the $[1\bar{1}0]$ directions to give the 3R, 6R, or 9R periodicity of the martensite phase (46). It was determined that these peaks are a bulk phenomena and an essential precursor to the martensitic transformation.

There is also disagreement from author to author about whether the observed phenomena are due to the surface, are a bulk phenomenon, or a thin film artifact, or possibly a combination of the three. In Ref. (42) the streaking was determined to occur in the layers just below a surface oxide present on the surface. The neutron and x-ray studies, due to the penetration depth of the probes, are assumed to reveal bulk phenomena. Others have dismissed the modulated structures seen in these β alloys as being a thin film effect (47).

In addition to the experimental evidence there are also theoretical expectations for the presence of surface martensite before the bulk transformation. One might expect that the higher lattice energy of the surface, compared to the bulk, would provide some of the strain energy needed to drive the transformation. In terms of providing a nucleation site for the bulk transformation, one may write the total free energy change for the formation of small particles of martensite as

$$\delta G = \delta G_V + \delta G_S + \delta G_E$$

where G_V is the chemical free energy, G_S is the interfacial free energy, and G_E is the accommodation elastic strain. In the bulk this elastic strain dominates the transformation. At the surface, however, this term may be neglected and the interfacial strain is now the main factor influencing the transformation. The reduction of the elastic strain term at the surface leads to an expectation that the surface may form a martensite phase prior to the bulk transformation. In a theoretical study of the free energy as a function of surface strain Chandrasekaran (48) found that atomic relaxations may be a possible origin of surface martensite, and the extra maxima observed in the electron diffraction

studies.

To summarize, there is a large amount of evidence that a surface martensite phase is present in β phase alloys prior to the bulk transformation. However, there is still substantial disagreement on the interpretation of the evidence. Even if one assumes that surface martensite exists there is the question of whether it is an intrinsic property, with relation to the bulk transformation, or an extrinsic property due to experimental conditions. A LEED study of the surface would be beneficial due to the surface sensitivity and the possibility of determining the surface structure.

For our studies of the β CuZnAl sample the (110) surface was chosen for two reasons. The first is the surface sensitivity of this surface to the formation of surface martensite. The second reason is the expectation that the close packed planes of the parent phase, (110), and the product phase will be closely related.

5:B Experimental

To obtain the best LEED pattern, the CuZnAl samples were Ar^+ ion bombarded at 5×10^{-5} torr Ar, 750 eV with 20 mA beam current. The base chamber pressure was 7×10^{-10} torr. Performing the LEED experiments under the 5×10^{-5} torr argon

ambient gave a better signal to noise (i.e. beam to background) than under high vacuum. To further increase the signal the electron gun filament current was set at 0.95 A. This higher than normal setting of the filament has a non linear emission current with energy and the possibility of introducing nonlinearities in the IV curves, but does not affect the symmetry of the pattern. Lower filament currents made resolution of spots difficult. It was also found that the background decreased and the spots sharpened with time (up to 45-60 min) at room temperature possibly due to annealing.

Two samples were used in these experiments, the first was only roughly oriented to within $\pm 5^\circ$ of the (110) surface, the second sample was oriented to within $\pm 2^\circ$ of the (110) surface. After the LEED experiments this second sample, using the new x-ray camera and sample mount described in the previous chapter, was found to be rotated $2^\circ \pm 1/2^\circ$ towards the $[00\bar{1}]$ direction. The results for the two samples agreed with each other, with the better oriented sample having a better pattern and narrower spot sizes.

All observations reported were made at room temperature. Observations at temperatures down to 0°C did not improve the pattern. Raising the temperature resulted in an increase in background and at about 100°C the pattern

disappeared and required further cleaning to be re-established. This disappearance may be due to rearrangement of the atoms from their reconstructed positions due to the temperature, or due to segregation to the surface of the zinc. The second explanation is more likely since the pattern did not reappear upon recooling.

The LEED pattern observed, shown in Fig. 5-1, had fractional order spots: $(n/3, m)$ and $(n, m/3)$, where n and m are integers. Figure 5-1 also shows the observed mirror plane. No $(n/3, m/3)$ spots were observed. The pattern, defined by the integral spots, was that expected for a $\text{bcc}(110)$ surface and was verified by photographing the pattern and measuring the angle between the $(1,0)$ and the $(0,1)$ directions. The fractional spots were attributed to two domains: a (3×1) and a (1×3) . The large background, the broadness of the spots, plus the closer spacing of the beams as the energy increased, made resolution of individual spots more difficult with increasing energy, until at 180-200 eV individual beams could not be discerned.

To further complicate the pattern, splitting of the spots was also observed. This splitting was initially seen as anomalous movement of the integral and fractional spots as a function of energy. As the electron energy was ramped certain spots appeared to move faster than the

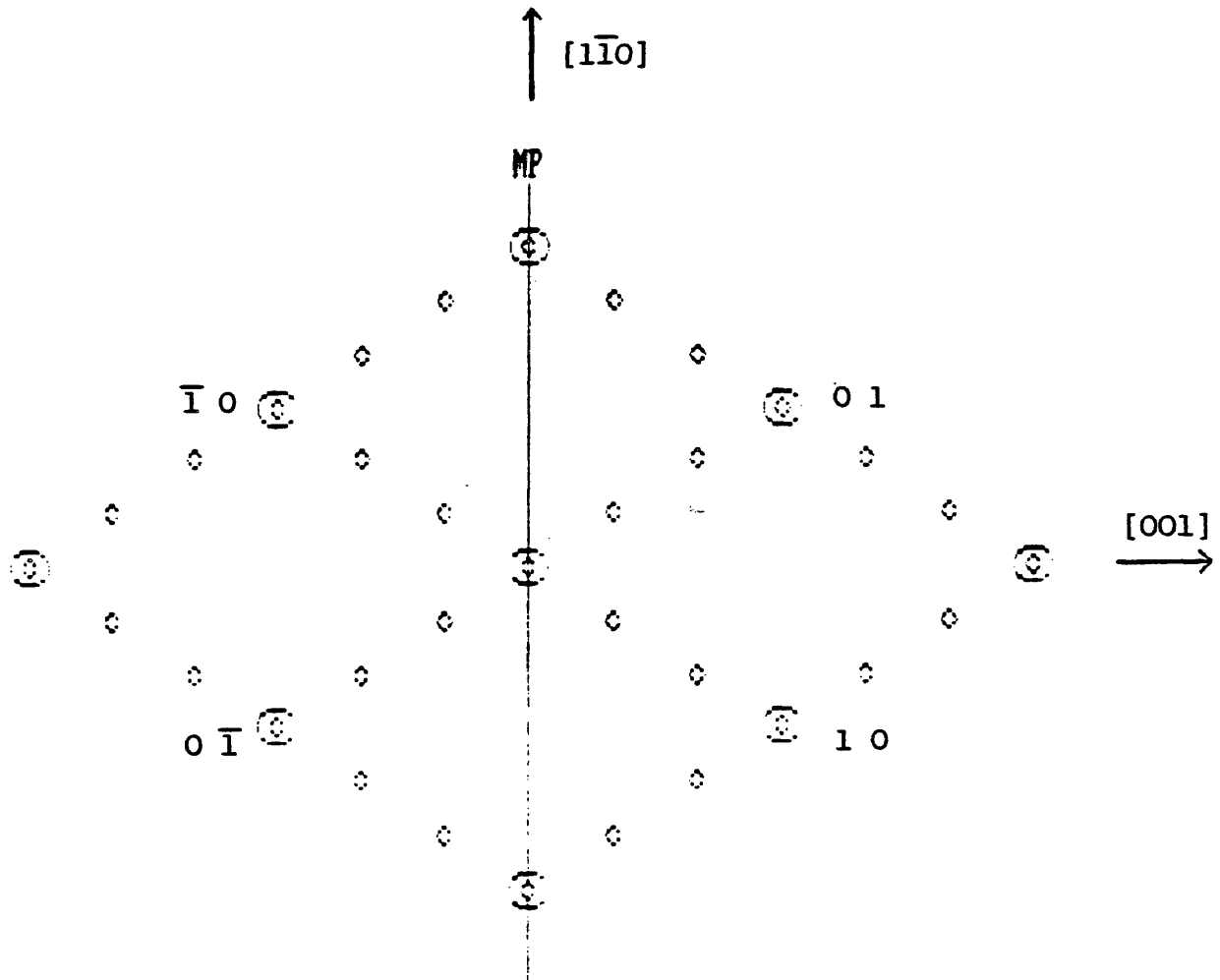


Figure 5-1. LEED pattern of the CuZnAl(110) surface showing a (3x1) and a (1x3) domain and the observed mirror plane. Defined in the figure are the crystallographic and the two-dimensional reciprocal lattice directions.

surrounding beams. It was only upon improvement of the pattern that this anomalous motion was resolved into the spot splitting. The high background and the broadness of the beams contributed to the difficulty of observing the splitting. All beams exhibited the anomalous motion, at differing energies, but only some beams could be resolved to split.

The pattern also exhibited an unexpected feature in its symmetry. The (3x1) and (1x3) domains had equal intensities with symmetric beams between each domain having the same IV behavior. However, the pattern intensities did not have inversion symmetry, e.g. the (1,0) and ($\bar{1}$,0) beams had different IV curves. This lack of inversion symmetry is unexpected for this surface since the unreconstructed bcc(110) surface has R2 periodicity with two orthogonal mirror planes and a 2D inversion axis. Any two dimensional lattice with translational symmetry, excluding the basis, has inversion symmetry. If one considers the basis, particularly in an alloy, inversion is no longer necessary. However, one would expect that LEED, which probes over a macroscopic area of the surface, would average over any local asymmetry and, thus, have inversion symmetry in the LEED pattern. Inversion, however, can be lost by considering the third direction in the stacking of the

layers (e.g. the fcc (111) surface has a 3-fold rotation axis and three mirror planes but no inversion axis). Thus, this lack of inversion symmetry indicates that some fundamental change occurs at this surface, which breaks the symmetry of the unreconstructed bcc (110) surface. Note, when the pattern was first observed, following only a few hours of cleaning and before resolution of individual spots was made, it appeared that the pattern possessed the two expected mirror planes and the inversion axis. However, after further cleaning to improve the pattern, the inversion symmetry was lost and did not reappear. This may indicate that the surface had been stabilized by the presence of impurities, prior to cleaning, which inhibited the reconstruction responsible for the loss of symmetry.

The most obvious explanation of the lack of inversion symmetry and the spot splitting is the presence of steps on the surface. The 2° misalignment of our sample introduces a step approximately every 60 Å. While smaller than the >100 Å terrace width desired in LEED, a 60 Å terrace is certainly large enough that scattering from the terrace should predominate over scattering from the steps. For this reason it is not considered likely that scattering from the steps is responsible for the loss of inversion symmetry. Also the observed mirror plane is the one expected to

be lost if steps from our misalignment were responsible.

Experimental error in the alignment of the sample surface is also not considered the likely cause. For a stepped surface there are two specular beams: the beam corresponding to the terrace, and the beam corresponding to the actual surface orientation. For our samples only one specular beam was observed. A second specular beam may be present and not seen due to the beam widths, but this places an upper limit of 1-2° on the misorientation from the (110) surface. Thus error in orientation of the surface is dismissed. Error in alignment of the sample to the electron beam is also considered an unlikely cause. The question of whether the steps are responsible for the beam splitting must also be addressed. A terrace of dimension smaller than the electron beam coherence length (~ 100 Å) will be seen as a superlattice and have corresponding fractional order spots. However, the intensity of a beam is inversely proportional to the area of the unit cell to which it corresponds (49). Since the intensity of the split spots were within an order of magnitude of the integral beams this tends to rule out the splitting as being due to a terrace whose smallest dimension is roughly 30 times the dimension of the bcc(110) unit cell.

To summarize, the LEED pattern had two domains, a (3x1)

and a (1×3) . Both integral and fractional spot were observed to split. The pattern had only a $(00\bar{1})$ mirror plane and was missing the expected $(1\bar{1}0)$ mirror plane and inversion axis. Scattering from steps on the surface is not expected to be the cause of either the spot splitting or the loss of the second mirror plane and inversion axis.

An IV analysis was not done on this surface. The splitting of the spots made it difficult to separate the IV curve for a particular beam from the IV curves of the surrounding split spots. For these two reasons it was decided that any measured IV curves would be suspect in their interpretation. However, a fair amount of information and inference can be made from the symmetry of this pattern.

5.3 Models Proposed

As mentioned above, any two dimensional lattice with translational symmetry must also have inversion symmetry. To break this symmetry requires the introduction of the third dimension either through rumpling of the atoms or through stacking. It is hard to imagine rumpling which would not have inversion since the two dimensional translational symmetry of the layer would position symmetric atoms equivalently. Similarly it is difficult to construct a basis which would not have inversion, particularly when

anti-phase domains are considered. A more likely possibility is a stacking fault which removes the symmetry.

The observed $(00\bar{1})$ mirror plane tells us that, on average, scattering in the $[001]$ and $[00\bar{1}]$ directions are equivalent. Conversely, the lack of the $(1\bar{1}0)$ mirror plane indicates that scattering in the $[\bar{1}10]$ and the $[1\bar{1}0]$ directions are not equivalent. A possible reason, and one preserving the bcc (110) layer is to shift the entire layer in the $\pm[1\bar{1}0]$ directions, such that the high symmetry axes in different layers does not coincide. Note, this proposed shift moves the atoms to pseudo 3-fold positions such as are present in close packed lattices. For one domain with a shift in the $[1\bar{1}0]$ direction the resulting surface now has only the $(00\bar{1})$ mirror plane. However, if one also allows for domains in which the shift is in the opposite direction, the resulting LEED pattern now has both orthogonal mirror planes. Thus for this model to be correct one domain must be preferred over the other. Steps and kinks might drive this preference. For our sample orientation the predominant steps will be in the $[00\bar{1}]$ direction (i.e. as one moves along the $[00\bar{1}]$ direction one will encounter the steps) with kinks (assuming $1/2^\circ$ misalignment in the $[1\bar{1}0]$) in the $[1\bar{1}0]$ direction every 100-150 Å. These kinks may be responsible for the preference in shift direction.

This stacking fault may not be confined to the top layer but be several layers deep. The martensitic transformation in this alloy changes the R2 BCC lattice to a R9 stacking faulted FCC lattice. Fig. 5-2 demonstrates how a modulation wave shifting the planes in the $[1\bar{1}0]$ direction might transform the R2 to a R3 periodicity. In Ref. 46, based on the neutron and x-ray diffraction studies, a modulation wave with this same shift of the (110) planes in the $\pm[1\bar{1}0]$ direction was proposed as the method of producing R3, R6 or R9 periodicity. The LEED conclusions, presented here, were made without reference to the literature.

There are a variety of possible reconstructions that may be responsible for the (3x1) domains. One of the more plausible is the Lattice Displacement Wave (LDW) in which the atoms are shifted from their positions in a wavelike manner with a three atom wavelength. In Fig. 5-3 the top bcc (110) surface layer is shown and the resulting surfaces obtained as the close packed rows are alternately shifted up and down along the $[1\bar{1}\bar{1}]$ directions as a function of the wave amplitude. A curious feature of this reconstruction model is that with an amplitude of approximately 35% of the nearest neighbor distance the resulting two dimensional lattice is also a bcc (110) layer rotated 70° with respect

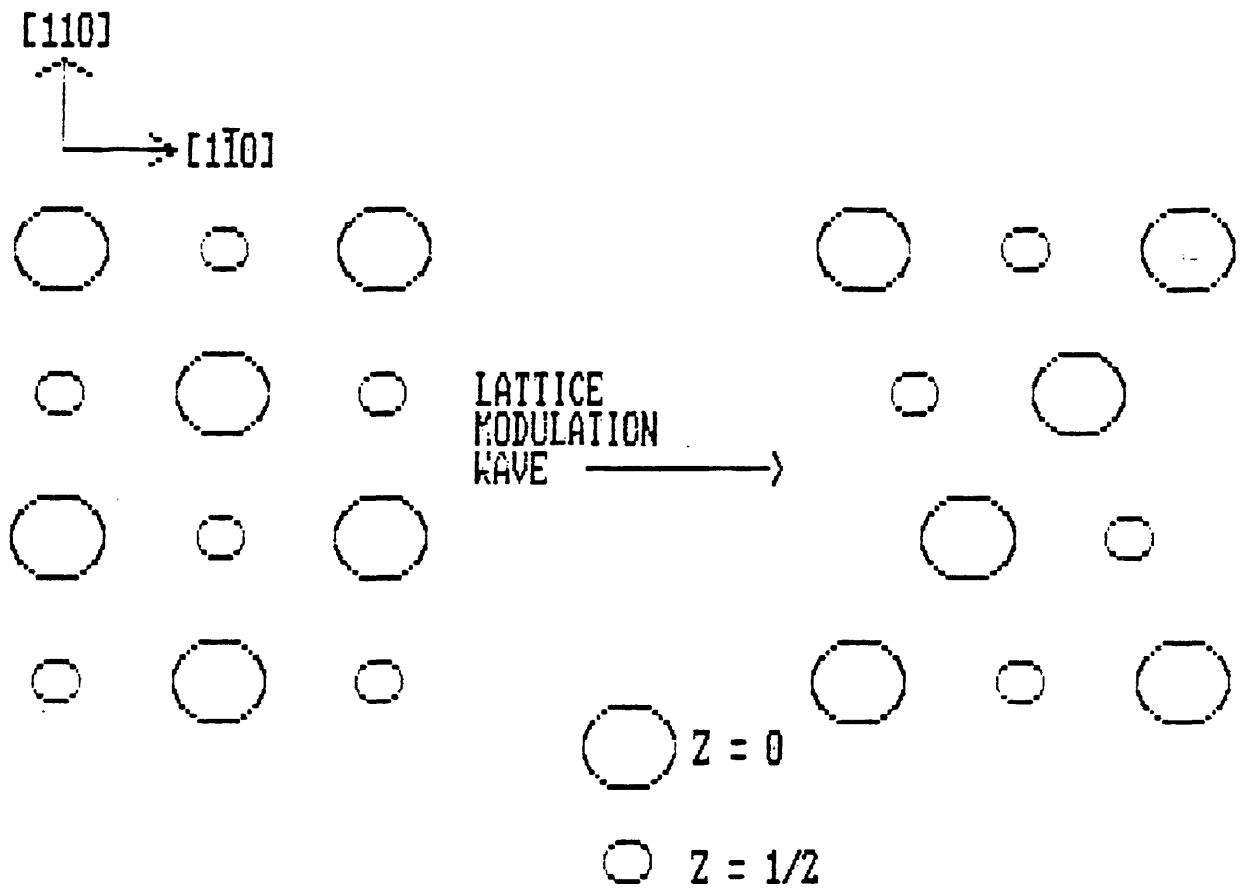


Figure 5-2. Modulation wave of the (110) planes in the $[1\bar{1}0]$ directions resulting in a R3 periodicity.

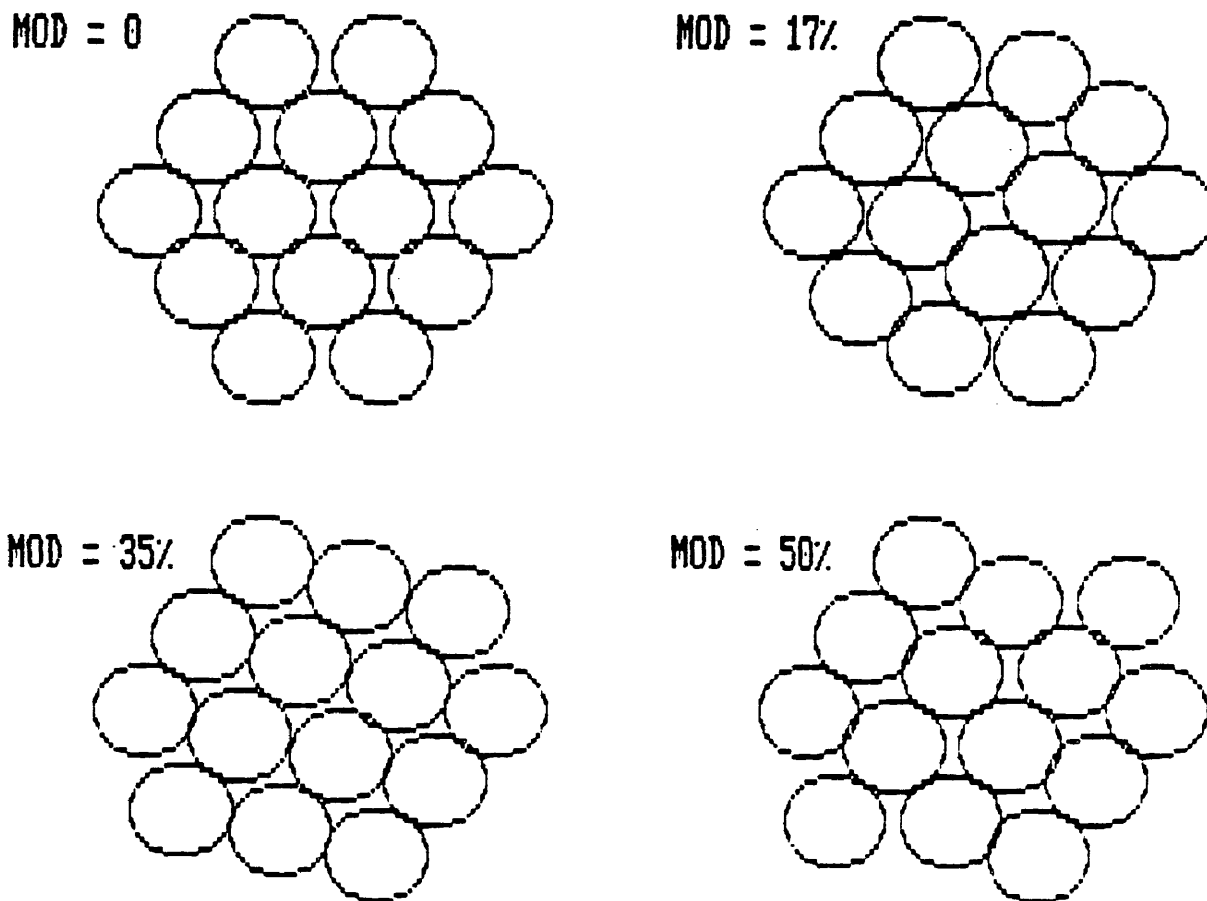


Figure 5-3. Lattice Displacement Wave shifting the close packed rows, from no displacement to 50% of the nearest neighbor distance.

to the previous orientation. Thus a (3x1) reconstruction of the surface could result in a layer with the same two dimensional periodicity of the original layer. This (3x1) reconstruction may be driven by the stacking fault proposed above.

Possible explanations for the spot splitting observed are the presence of antiphase domains and/or an additional superlattice present on the surface with larger unit cell than the (3x1). Antiphase domains are known to lead to spot splitting on a variety of surfaces (50). Briefly, if there is some periodicity to a domain or a domain/anti-domain alternation, the result is a superlattice with a unit cell made up of some number of the basic domains. In this system possible domains are the (3x1) and the (1x3), and if the LDW model is correct the phase of the wave.

Another and more intriguing possibility, for the spot splitting, is the presence of an additional superlattice on the surface. Any such model proposed for such a superlattice is pure speculation, yet one might imagine that some hexagonal patches of atoms might form. In particular Cu, Zn, and Al in their pure form are all close packed lattices. The high vapor pressure of zinc and the indication, from the WDS measurements, that zinc is evaporating from the surface suggests that there may be a

large difference in the composition of the surface compared to the bulk. This difference in composition may lead to the formation of close packed islands. As stated this is all speculation; what we do know is that the spot splitting is reproducible, not only in the same sample but from sample to sample.

To put the above discussion together, we propose the following model for the reconstruction of the β -CuZnAl(110) surface and the formation of a surface martensite phase. The R2 stacking periodicity of this surface is changed in preparation for the R3 (or R9) periodicity of the bulk martensite by the presence of a Lattice Modulation Wave translating the (110) layers in the $[1\bar{1}0]$ direction. The top layer is additionally reconstructed into (3x1) domains by the presence of a Lattice Displacement Wave which moves the close packed rows in the $[1\bar{1}1]$ direction, which may have the effect of rotating this top layer by 70° . Additionally the surface may have hexagonal islands which are responsible for the spot splitting observed, and which may be precursive to the eventual close packing of this layer in the bulk martensite.

5.D: Discussion

To summarize, we have observed a definite reconstruction of the CuZnAl(110) surface at temperatures 30-50°C above the transformation temperature. The Lattice Modulation Wave and the Lattice Displacement Wave proposed for the reconstruction are consistent with models proposed for the extra maxima seen in TED studies of beta phase alloys. These models were deduced from the LEED experiment and prior to reference to the literature. The reproducibility of the pattern across the sample, and among samples which differed in their orientation by several degrees, suggests that this is an intrinsic property of the surface. In addition the surface sensitivity of LEED and the thickness of the sample (1-2 mm) rules out the reconstruction as exclusively a bulk or thin film artifact. The cleanliness of the surface, after ion bombardment, discounts impurities as a cause (there are even indications that impurities may inhibit the reconstruction). However, the UHV environment may be responsible for compositional changes at the surface which may affect the reconstruction.

Due to the richness of the LEED pattern for this β CuZnAl alloy and the volatility of the pattern with temperature these β -phase alloys seem to be good candidates for further study. In particular, replacing the zinc with

a more vacuum friendly component would allow greater freedom of study. For example CuNiAl exhibits many of the same TED phenomena as CuZnAl.

6: Surface Structure of FeNi(111)

6.A: Motivation

The evidence for a surface martensite in FeNi alloys is less convincing than for the beta phase alloys described above. Klosterman (51) found evidence, from visual and from electron diffraction studies, of surface martensite in Fe-30.2%Ni-0.04%C alloys. This surface martensite could be formed either through plastic deformation or by electropolishing and extended 5 to 30 microns into the bulk. The orientation of the surface martensite was of the Nishiyama-Wasserman relationship found for the bulk transformation in FeNi alloys. Specifically the relationship is

$$(111)_P \parallel (011)_M, \quad [11\bar{2}]_P \parallel [0\bar{1}1]_M.$$

Tyapkin (52) in electron diffraction studies of 27-50%Ni FeNi alloys observed diffuse electron scattering which increased as M_s was approached from above. He attributed this diffuse scattering to dynamic (phonons) and static displacements of atoms. However, Finlayson (53) was able to describe the diffuse streaks by a Kohn Anomaly interaction. In studies of surface relief, the M_s in surface layers of FeNi alloys was 10-30°C higher than in the bulk. The M_s was also found to be higher in thin FeNi foils than in the bulk

(54). Thus there are indications that FeNi surfaces may form surface martensite at temperatures above the bulk transformation.

Due to the orientational relationship between the parent and martensite lattice where the two close packed planes are parallel to each other, our studies of this alloy concentrated on the (111) surface.

6.B: Experimental

The sample was Ar^+ ion bombarded: 500 eV, 20 mA beam at 5×10^{-5} torr Ar. The base chamber pressure was 5×10^{-10} torr. Following bombardment the sample was annealed at 825 K for 10 min then cooled to the experimental temperature. The sample, due to poor thermal contact to the cooling coils, could only be cooled to room temperature in 10 min and to 200 K in 30 min. Orientation of the sample and minimization of stray magnetic fields was verified by similarity of symmetric beams.

A (1x1) hexagonal pattern was observed and no superlattice spots were seen. The pattern, at normal incidence, had the three fold symmetry expected for a fcc(111) surface. Fig. 6-1 shows the observed pattern, the direction of rotation for off normal incidence of the electron beam and the beam notation used.

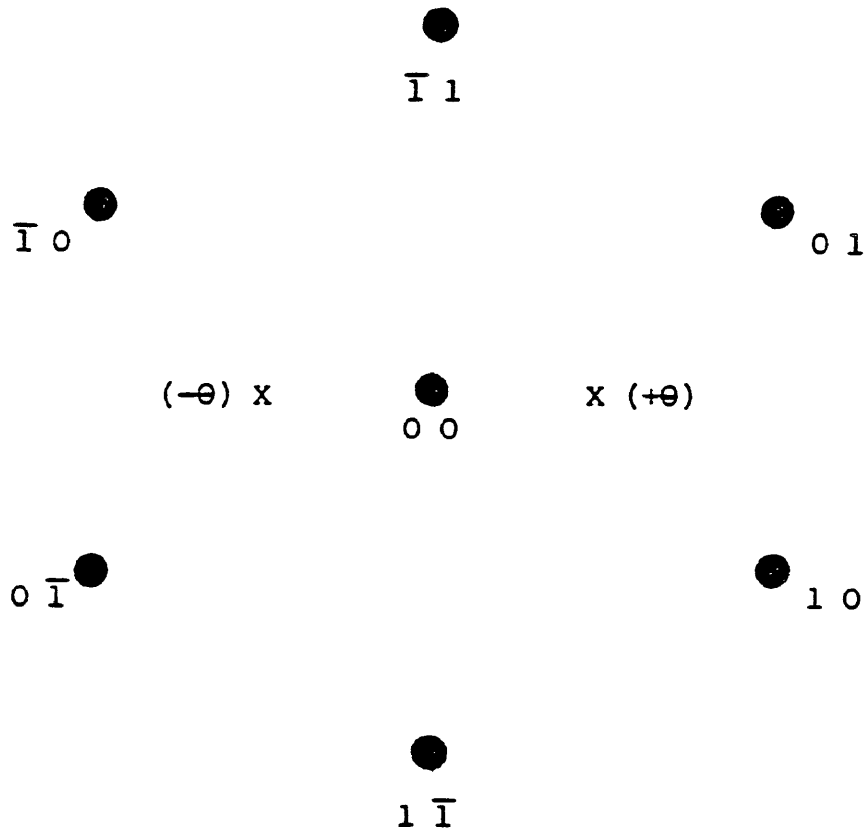


Figure 6-1. LEED pattern of the FeNi(111) surface showing beam designation and orientation of off-normal incidence of the electron beam.

Prior to obtaining LEED IV data the surface Debye temperature was determined. Within the kinematic limit the intensity of backscattered electrons as a function of temperature is given by

$$I = I_0 e^{-2M}$$

where the exponential is the Debye-Waller factor. For the specular (0,0) beam the Debye-Waller factor is given by

$$2M = \frac{24mT(E\cos^2\theta + V_0)}{m_a k_B (\theta_D^{\text{eff}})}$$

where m is the free electron mass, m_a is the mass of the atom, E is the incident electron energy, V_0 is the inner potential, k_B is the Boltzmann constant, T is the temperature and θ_D^{eff} is the effective Debye temperature for the perpendicular component of the atomic vibration (55). Thus a plot of the $\ln(I)$ vs. temperature will give the effective Debye temperature. Experimentally, the background increases with temperature and this background intensity, I_b , must be subtracted from the measured intensity.

Figure 6-2 shows the (0,0) beam at room temperature and $\theta=10^\circ$. The three peaks at 69 eV, 130 eV, and 211 eV were used

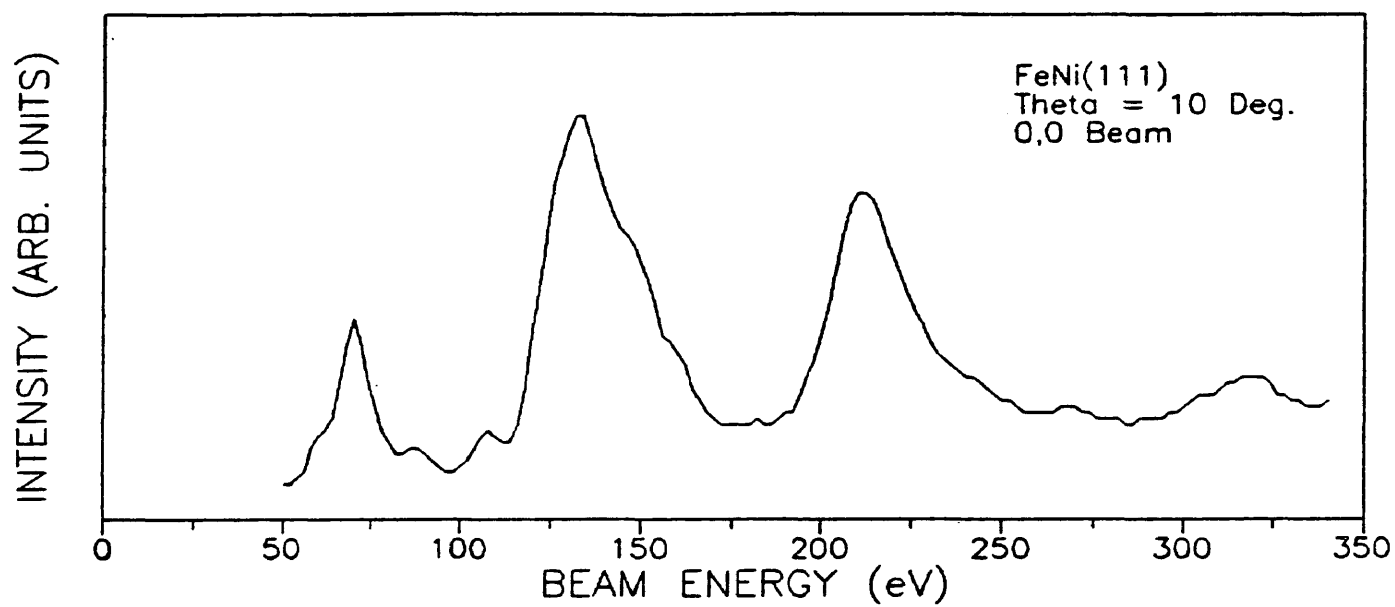


Figure 6-2. Experimental IV curve for the (0,0) beam at 10° off normal incidence and at room temperature.

for the intensity vs. temperature measurements. The peak at 320 eV was too small and could not be discerned from the background at higher temperatures and was not used. The sample was heated to 650 K and then allowed to cool. Data were not taken until the temperature reached 495 K when the cooling rate was at a manageable 2.5 K/sec. The cooling rate decreased with temperature and at 325 K had fallen to 0.25 K/sec. The total time to cool from 495 K to 325 K was about 5 min. Intensity data were continuously recorded on a x-y recorder. The background was measured by moving the window off the beam every 25-30 K during the data run. The plot of the $\ln(I-I_D)$ vs. temperature is shown in Fig. 6-3. The results are tabulated below. The two high temperature

E (eV)	e_D^{eff} (K)
-----	-----
69	303
130	342
211	389

readings at 211 eV are excluded. The increase in background plus the closer spacings of the beams at higher energy made measurements of the background intensity difficult especially at higher temperatures. If these two points are included the resulting fit gives $e_D^{eff}(211 \text{ eV}) = 465 \text{ K}$. Note, that as the electron energy increases the effective surface Debye temperature also increases due to the greater

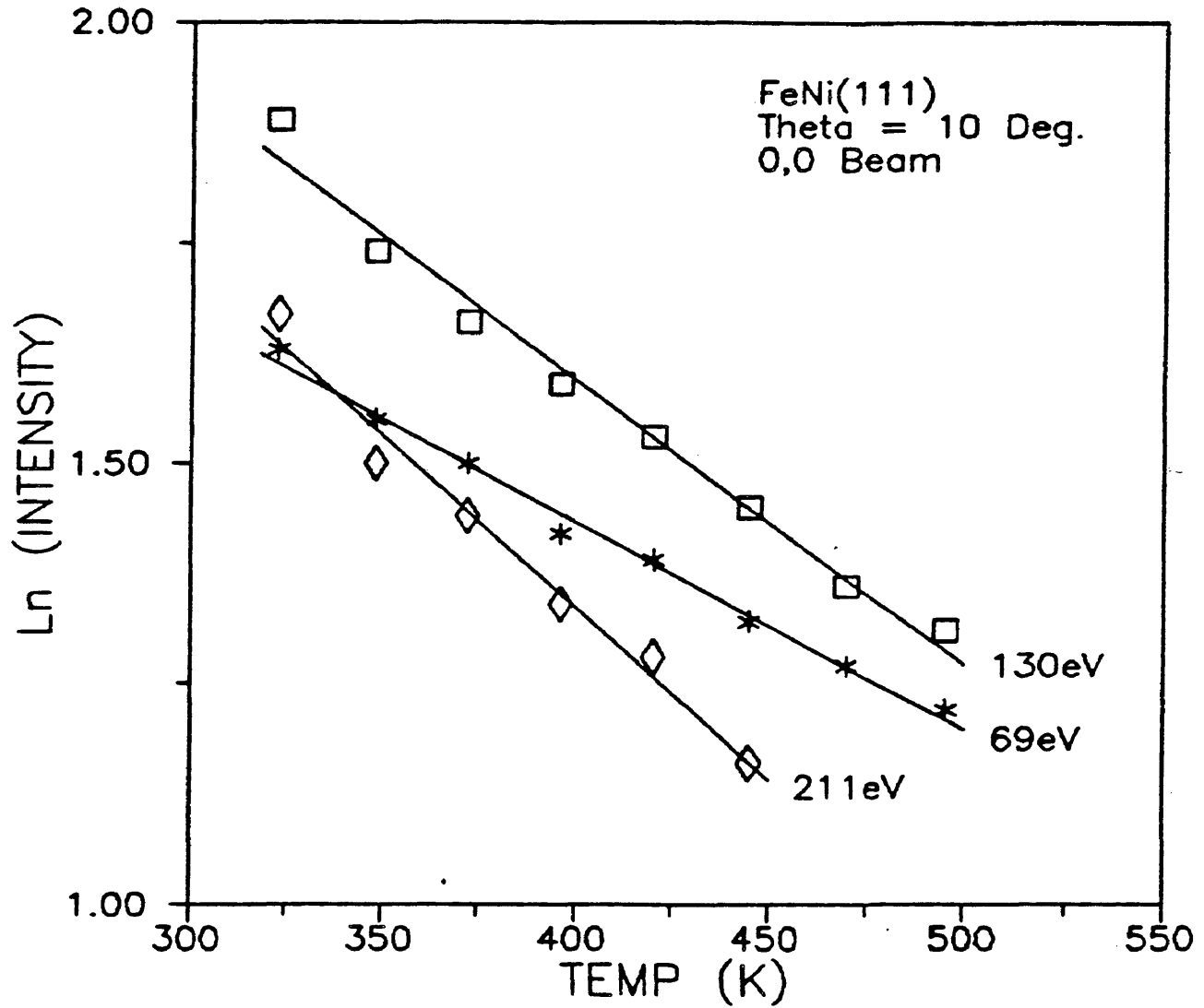


Figure 6-3. The intensity versus temperature for the (0,0) beam.

penetration depth of the electrons. As the electrons probe deeper into the sample they detect more bulk-like behavior of the atomic vibrations. The linear variation of the effective Debye temperature with energy is also expected for electron energies in this range (56).

The IV curve for the (0,0) beam seen in Fig. 6-1 has four main peaks and appears to be highly kinematic. The Bragg peaks for the (0,0) beam are given by the formula

$$E = \frac{150.4 n^2}{4 \cos^2 \theta d^2} - \frac{V_0}{\cos^2 \theta} \quad (6-1)$$

where E is the peak energy in eV, V_0 is the inner potential in eV, d is the interlayer spacing in Å, and θ is the angle of incidence (57). The plot, shown in Fig. 6-4, of the 4 main diffraction peaks in the IV curve versus the square of the Bragg indices 3,4,5, and 6 has a good linear fit to Eq.(6-1). The slope gives a value of $d = 2.0524$ Å. The expected value for the (111) interlayer of this alloy is 2.0528Å, given the FCC lattice constants of 3.571 Å for Fe and 3.524 Å for Ni (58) and Vegards Law for extrapolating the lattice constant. The inner potential V_0 from the intercept is 13.6 eV. This is not the actual value of the inner potential since contact potentials of 1-2 eV between the sample and electron gun are not taken into account.

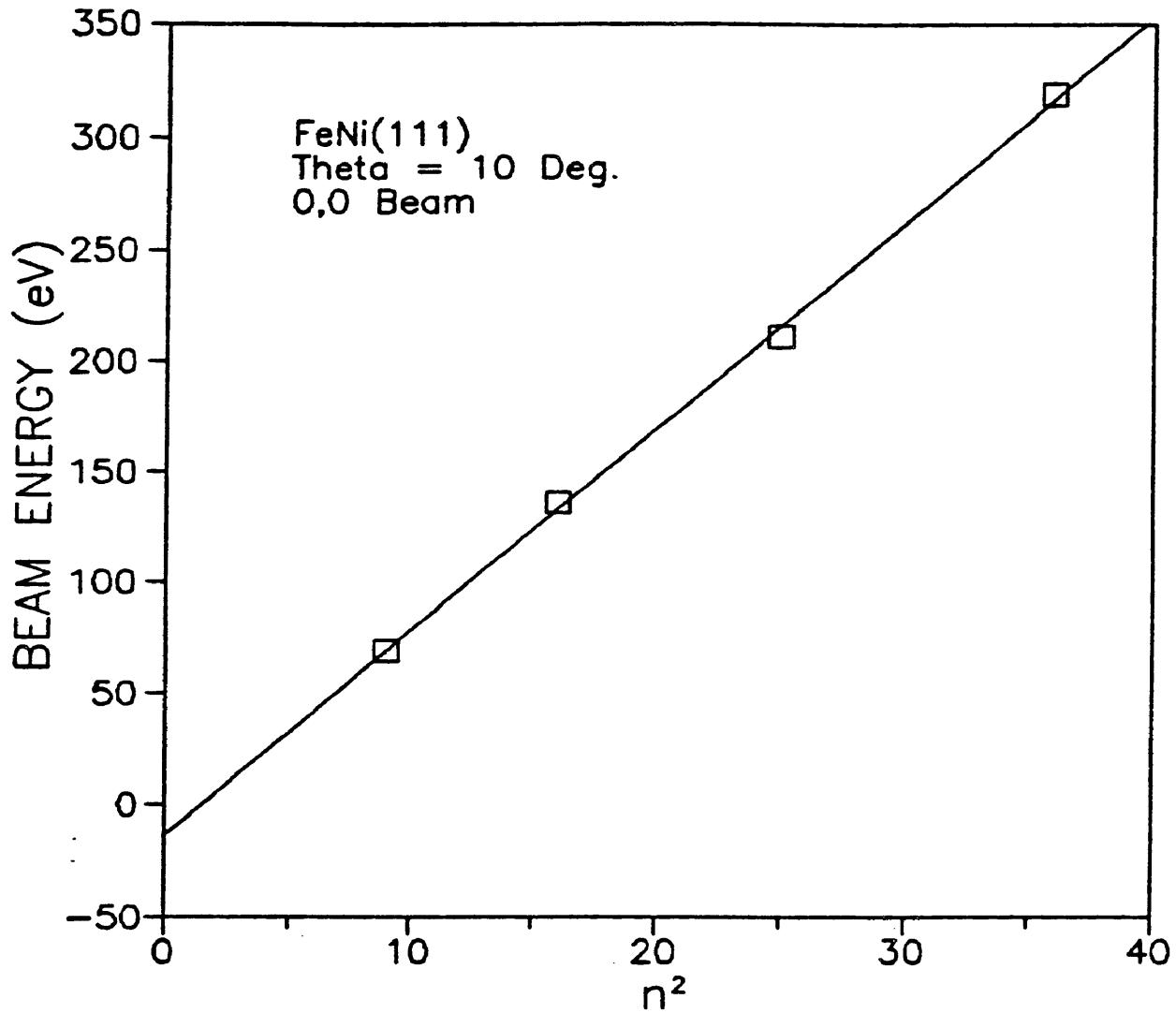


Figure 6-4. Bragg peaks of the (0,0) beam as a function of the Bragg index.

However, this value of 13.6 eV is an upper bound to the true inner potential, whose expected value is in the range 10-12 eV.

Following the above measurements IV data was acquired for this surface. Data was taken at 300 K, 205 K, 183 K, and at 180 K. The IV spectra for these four data sets were identical in peak location and relative peak heights. The only difference was in the width of the peaks between the data at 300 K and the lower temperature data. The original plan was to acquire IV data at lower and lower temperatures until the martensitic transformation temperature was reached, and to explore any changes in the IV curves and/or the pattern. Unfortunately, the poor thermal contact between the sample and cooling coils limited the lowest temperature reached to 180 K, 55 K above the "normal" limit and 25-70 K above the expected M_s . The lack of any change in the pattern and in the measured IV curves in the temperature range 500 K to 180 K suggests that a surface martensite phase, if present, forms at temperatures less than 25-70 K above M_s .

Data were taken "live" since the video recorder introduced a large amount of noise into the recorded IV curves. Following the ion bombardment cleaning and annealing the sample was cooled to the experimental

temperature. Cooling to 200 K required 30 min and the subsequent IV acquisition took another 13 min, giving 43 min from anneal to end of data acquisition. This amount of time is long enough for any residual gases present in the system to adsorb on the surface. However, due to the reproducibility of the IV curves and the lack of any observed superlattice any adsorbates are expected to add only to the background and not to any features in the IV curves.

IV spectra was acquired for 15 beams of which 7 were inequivalent by symmetry. The normal incidence beams acquired were the $(\bar{1},0)+(0,1)+(1,\bar{1})$ and the $(1,0)+(0,\bar{1})$, where the plus sign indicates those averaged due to symmetry. Off-normal data was taken at $+8^\circ$ and -8° , both directions in order to average symmetric beams and to minimize any error in the azimuth and angle of incidence. The beams acquired were $(0,0)_+ + (0,0)_-$, $(1,\bar{1})_+ + (1,\bar{1})_-$, $(0,\bar{1})_+ + (1,0)_-$, $(1,0)_+ + (0,\bar{1})_-$, and $(\bar{1},\bar{1})_+ + (1,1)_-$ where the subscripted plus and minus refer to the direction of rotation. Again the symmetric beams were similar in all aspects. For the analysis the 200 K data was used since it had the least noise. Data at the other temperatures was not analyzed due to the lack of any significant differences in the IV spectra. During the R-factor analysis low R-factors

were obtained without data smoothing. Thus no smoothing was done on the experimental IV curves under the premise that the less filtering done the better. Background subtraction was performed on the IV data using the same method described in the CO chapter of this dissertation.

6.C Analysis

The theoretical calculations of the IV curves were made using a pre-existing program (59). The scattering in the bulk was by renormalized forward scattering. Thirty-one beams were used in the calculations and no symmetry was assumed in order to use the same program for the normal and off-normal calculations. The atomic scattering was calculated to 8 partial wave phase shifts. These phase shifts were calculated using often tested potentials (60). The scattering in this alloy was modeled by averaging the Fe and Ni phase shifts consistent with the expected Fe-32%Ni composition. Although surface segregation is not expected to be significant in this alloy a difference in composition of the surface from the bulk is not expected to significantly alter the IV curves due to the similar scattering potentials of the two atoms. Figure 6-5 shows the L_0 phase shifts of Fe and Ni. Note that the two atoms have similar potentials, with the average alloy atom having

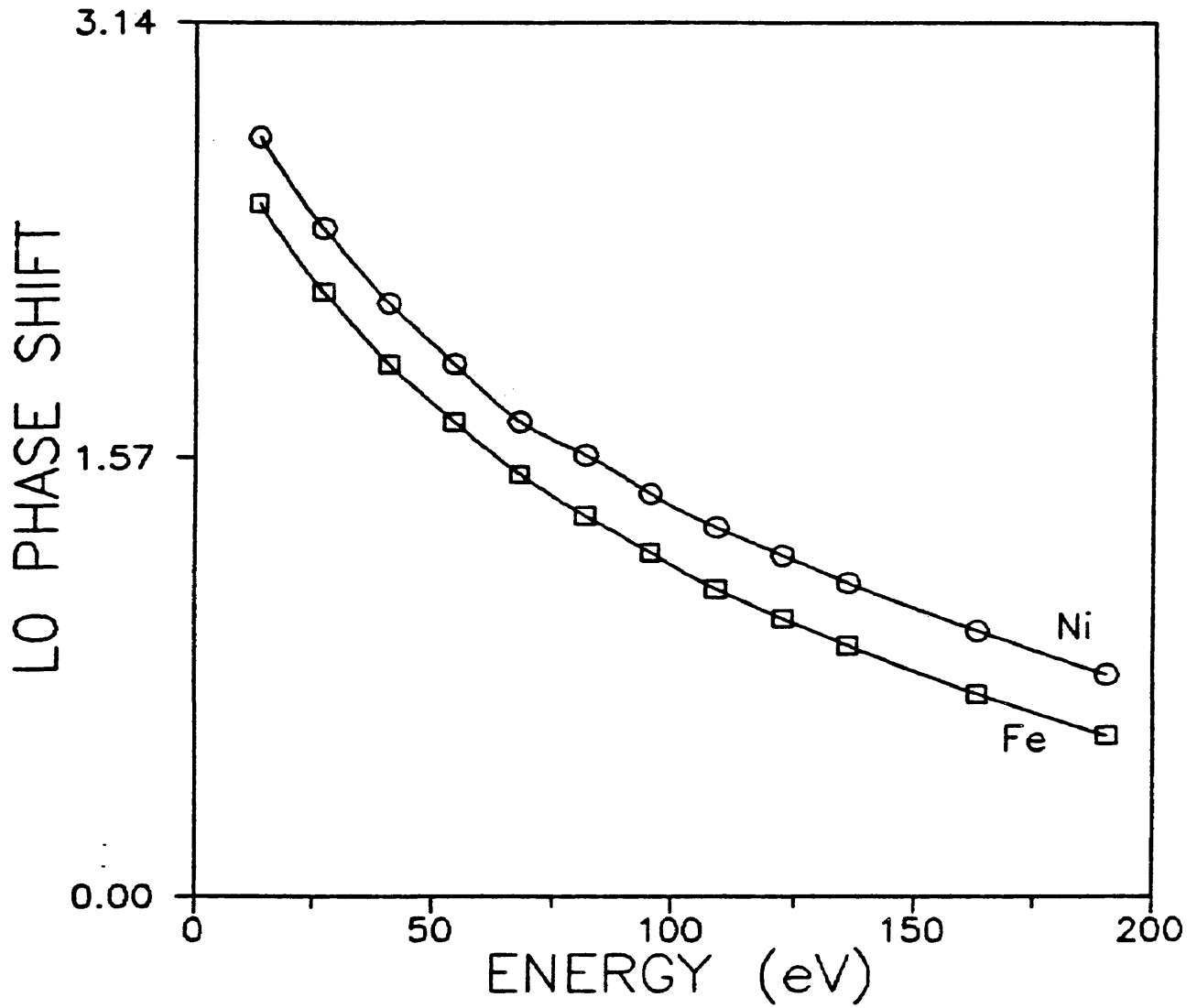


Figure 6-5. The L_0 phase shift for Iron and Nickel as input to the IV calculations.

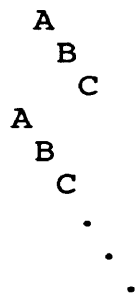
a potential between the two. Note in the calculations the phase shifts are extrapolated to energies higher than the 200eV limit shown in Fig. 6-5. The Debye temperature used in the calculation was 325 K and an inner potential of 11eV was assumed.

Four structural models were examined in the analysis. These are shown schematically in Fig. 6-6. The four models correspond to R3(ABCABC...) and R2(ABAB...) stacking surfaces on R3 and R2 bulk substrates.

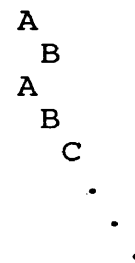
6.D: Results

In the initial geometries two structural parameters were varied: the lattice constant and the first interlayer spacing. Three lattice constants were tried: the value expected for a Ni lattice, 3.52 Å, the value for a Fe-32%Ni lattice, 3.556 Å, and that expected for an fcc Fe lattice 3.57 Å. Three first interlayer separations were also tried: a 5% contraction from the bulk value, bulk spacing, and a 5% dilation. Visually the pure fcc stacking structure gave the best agreement with the experimental IV curves. Figures 6-7 and 6-8 shows the agreement for the four models given a 3.556 Å lattice constant and bulk first interlayer separation. The individual R-Factors for each beam are also displayed in the figure which bear out the visual

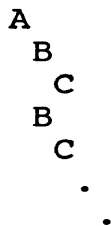
FCC Bulk
FCC Terminated



FCC Bulk
HCP Terminated



HCP Bulk
FCC Terminated



HCP Bulk
HCP Terminated

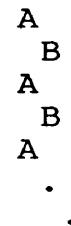


Figure 6-6. Schematic of four possible stacking models for the FeNi(111) surface.

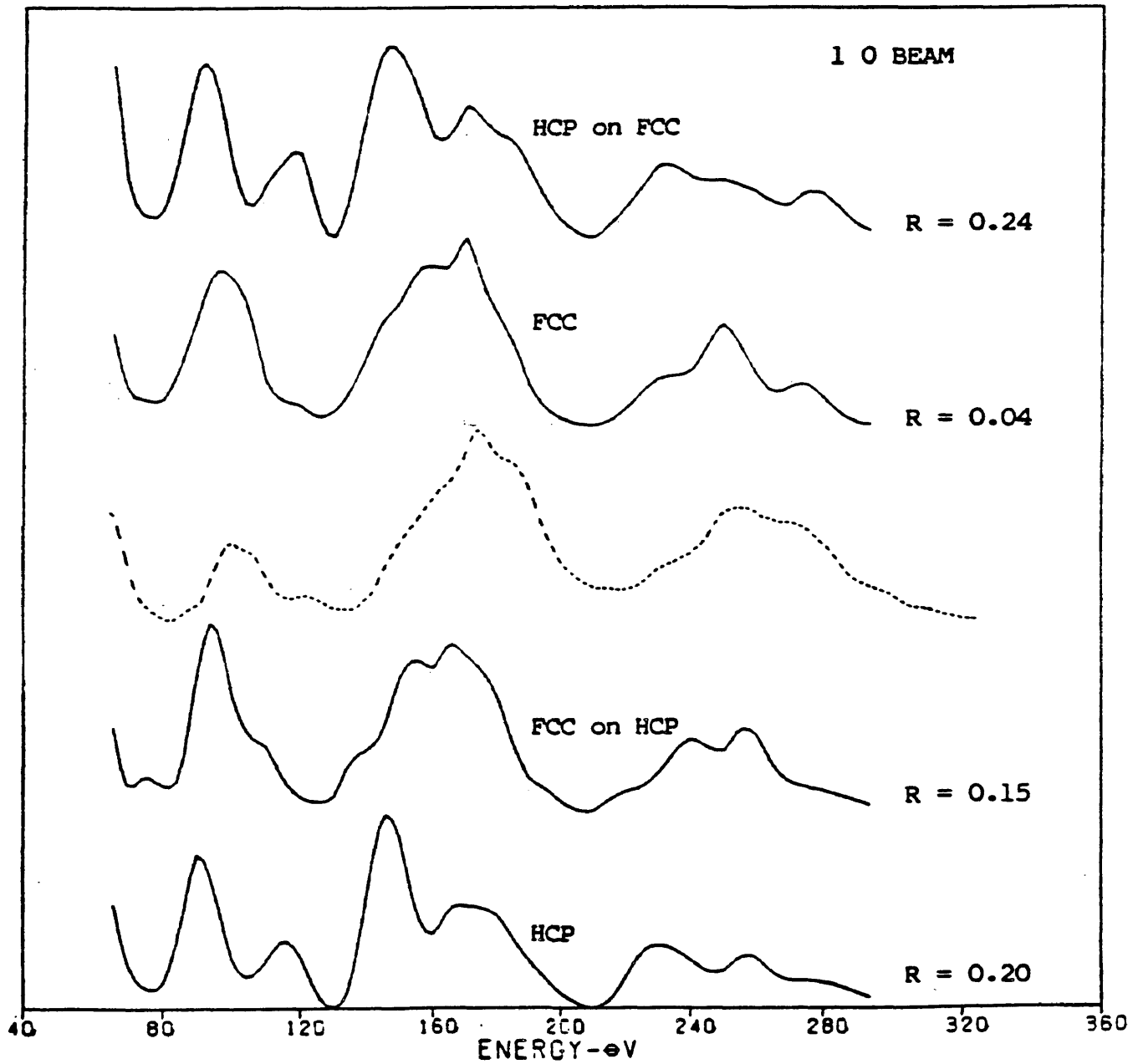


Figure 6-7. IV curves for the (10) beam at normal incidence for the four stacking models.

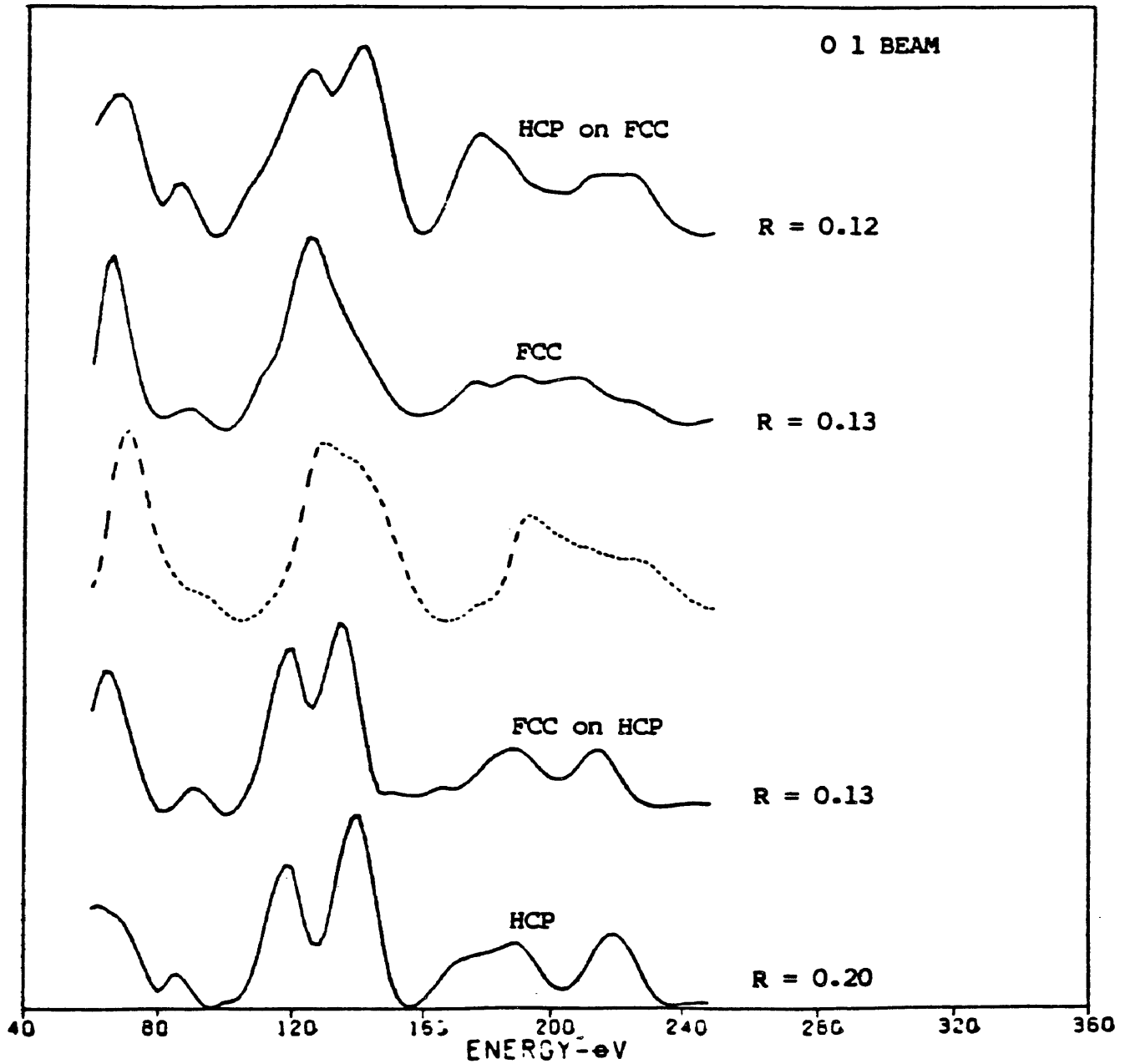


Figure 6-8. IV curves for the (01) beam at normal incidence for the four stacking models.

assessment. The off-normal incidence beams also gave the better agreement to the pure fcc geometry. Since the LEED pattern had 3-fold symmetry pure hcp stacking would normally be excluded. The 3-fold symmetry of the hcp terrace is lost in favor of 6-fold symmetry when domains due to mono-atomic steps are considered. However, to allow for the possibility of double-atomic steps the HCP geometries were calculated. Note also that the calculated IV curves differ for all four models which indicates that, theoretically for this surface, LEED is sensitive to differences in stacking between the fourth and fifth layer.

The analysis then focused on the fcc terminated surfaces on a fcc substrate. Again the lattice constant and first interlayer separation were varied. Four lattice constants were tried: 3.52 Å, 3.54 Å, 3.556 Å, and 3.57 Å. The interlayer was varied from a 5% contraction to 0% contraction in 1% steps (0.02 Å). The results are shown in Fig. 6-9. Two main features should be noted in this plot of the R-factor versus interlayer. First is the very low value of the R-Factor: ≈ 0.076 . Second is that as the lattice constant increases the minimum in R-factor moves to lower values of the first interlayer. This is to compensate the increase in the second and deeper interlayers as the lattice constant increases. The average of the first and second

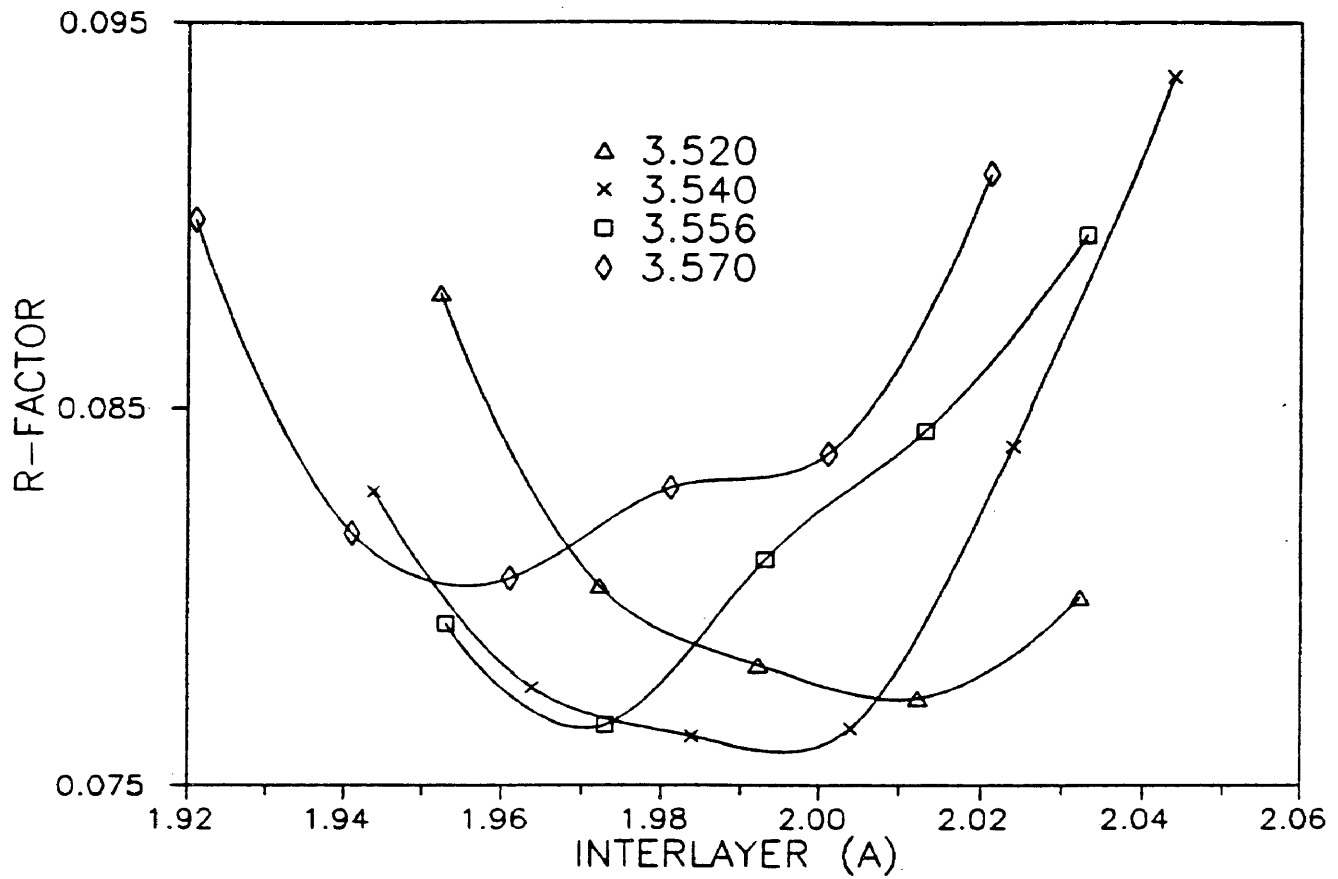


Figure 6-9. R-factor as a function of the first interlayer spacing for four possible lattice constants.

interlayers (the second interlayer is equal to the bulk value) is 2.01 Å to within 0.005 Å for all four lattices as shown in Table 6-1. This behavior and the large variation (0.05 Å) of the first interlayer separation suggested changing the second interlayer from the bulk value.

The first interlayer was varied from a 0% to 6% contraction and the second interlayer from a 1% contraction to a 3% dilation, both in 1% steps. Not every point in this space for all four lattices was calculated, but the minimum in all cases was bracketed. While contour plots of the R-factor results are disappointing in their fit to the two dimensional surface Fig. 6-10 is representative of the contour plots generated and illustrates the negative correlation between the first and second interplanar separations. The results for these geometries are shown in Table 6-2. Again if one averages over the first, second and third (bulk) interlayer separations the result for the four lattices is 2.027 ± 0.003 Å, where the uncertainty is the standard deviation over the four lattices.

6.E: Discussion

One must resist the temptation to place too much emphasis on small changes in the R-factor. In the geometries above changes of ± 0.01 Å in one of the parameters

	LATTICE CONSTANT (Å)			
	3.520	3.540	3.556	3.570
First Interlayer (Å)	2.01	2.00	1.97	1.96
Second Interlayer (Å)	2.03	2.04	2.05	2.06
Average (Å)	2.02	2.02	2.01	2.01

Table 6-1. Summary of the first interlayer variation as a function of lattice constant.

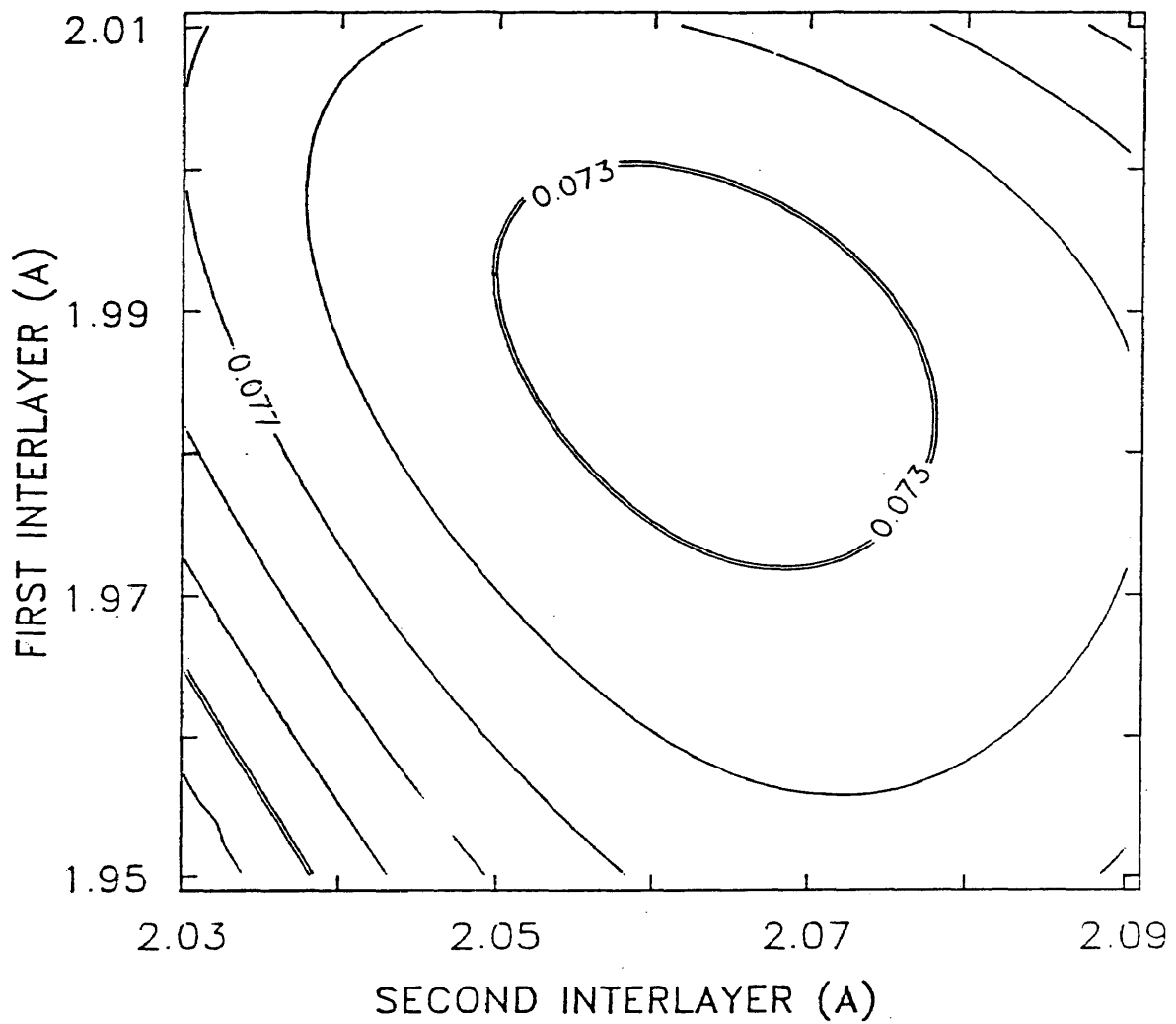


Figure 6-10. R-factor contour plot of the first and second interlayer assuming a lattice constant of 3.52Å.

	LATTICE CONSTANT (Å)			
	3.520	3.540	3.556	3.570
R-Factor	0.072	0.074	0.077	0.081
First Interlayer (Å)	1.99	1.98	1.97	1.96
Second Interlayer (Å)	2.07	2.06	2.05	2.06
Third Interlayer (Å)	2.03	2.04	2.05	2.06
Average (Å)	2.03	2.02	2.03	2.03

Table 6-2. Summary of the first and second interlayer variation as a function of lattice constant.

result in a variation of about 0.001 in the R-factor. The heuristic nature and lack of a universally accepted R-factor rules out placing much stock in such small changes. This is the motivation behind using changes of 0.02-0.03 in the R-factor to determine the uncertainty in the structural parameters. Given the size of our R-Factor minimum, ≈ 0.07 , we will use a variation of 0.01 as defining the uncertainty.

The first question to be decided is that of the true lattice constant. The standard practice, in LEED, is to assume a lattice constant and leave this value constant throughout the analysis. Wayman (61) in a Fe-30.2wt%Ni alloy determined the lattice constant to be 3.591 Å. In FeNi₃ the lattice constant was determined to be 3.552 Å (57). In a LEED kinematic treatment the lattice constant for a Fe-59%Ni alloy was found to be 3.70 Å. Our kinematic treatment gave a result of 3.56 Å. From a nearest neighbor viewpoint, with values of 2.48 Å for bcc Fe and 2.49 Å for fcc Ni (62) suggests that the alloy would have a lattice constant < 3.52 Å for all compositions. This lack of a agreement in the lattice constants of FeNi alloys was the motivation behind varying this parameter. Our dynamical results have the minimum R-factor for a lattice constant of 3.52 Å for this Fe-32.5%Ni alloy. However, this minimum was found using 0.02 Å steps in the interplanar separation and

1.0eV shifts in the inner potential. The actual minimum may change if the parameter space was explored about the minimum for each of the lattices using smaller step sizes. Given the caveat above about placing too much emphasis in small R-factor variations such a search was deemed to be unwarranted.

I propose that, at 200 K, the actual lattice constant is (3.54 ± 0.03) Å with a first interlayer contraction of $(3 \pm 1.5)\%$ with a value of (1.98 ± 0.03) Å and a second interlayer dilation of $(1 \pm 1.5)\%$ with a value (2.06 ± 0.03) Å. The average of the first three interlayers is (2.027 ± 0.003) Å.

In a LEED study of the Ni(111) surface in which only the top interplanar separation was allowed to vary the result was a $1.2 \pm 1.2\%$ contraction (63). A theoretical calculation on the Ni(111) surface predicts a 2.9% contraction of the first interlayer and a 1.4% dilation of the second interlayer (64). These results, for this similar surface, are consistent with our results for this FeNi alloy.

Despite the success, measured by the R-factor, of our structural determination of this FeNi(111) surface there is disappointment that equipment limitations prevented our definitively answering the question of whether a martensitic

phase is present on the surface prior to the bulk transformation. All we can conclude is that at temperatures down to 180 K there is no evidence that a surface martensite phase exists. It is hoped that this study serve as the basis for a complete study of this surface as the martensitic transformation occurs.

REFERENCES CITED

1. M. A. Van Hove and S. Y. Tong, Surface Crystallography by LEED, Springer Verlag, Berlin (1979).
2. M. A. Van Hove, W. H. Weinberg, C. -M. Chan, Low Energy Electron Diffraction: Experiment, Theory and Surface Structure Determination, Springer Verlag, Berlin, 237 (1986).
3. E. Zanazzi and F. Jona, Surf. Sci. 62, 61 (1977).
4. SURFACE II Graphics System, Kansas Geological Survey.
5. R. J. Behm, G. Ertl, Surf. Sci. 160, 387 (1985).
6. R. M. Lambert, Surf. Sci. 49, 325 (1975).
7. J. C. Bertolini and B. Tardy, Surf. Sci. 102, 131 (1981).
8. B. J. Bandy, M. A. Chesters, P. Hollins, J. Pritchard and N. Shepard, J. Mol. Struct. 80, 203 (1982).
9. R. J. Maddix, J. L. Gland, G. E. Mitchell and B. A. Sexton, Surf. Sci. 125, 481 (1983).
10. M. Nishijima, S. Masuda, Y. Sakisaka and M. Onchi, Surf. Sci. 107, 31 (1981).
11. P. R. Mahaffy and M. J. Dignam, Surf. Sci. 175, 651 (1986).
12. J. Lee, J. Arias, C. Hanrahan, R. Martin, H. Metiu, C. Klauber, M. D. Alvey and J. T. Yates, Jr., Surf. Sci. 159, L460 (1985).
13. W. Reidl and D. Menzel, Surf. Sci. 163, 39 (1985).
14. M. D. Alvey, M. J. Dresses and J. T. Yates, Jr., Surf. Sci. 165, 447 (1986).
15. H. Kuhlbeck, M. Neumann and H. -J. Freund, Surf. Sci. 173, 194 (1986).
16. H. -J. Freund, J. Rogozik, V. Dose and M. Neumann, Surf. Sci. 175, 651 (1986).

17. IMSL ICSSCU
18. Y. Gauthier, R. Baudoing, C. Gaubert and L. J. Clarke, *J. Phys. C.* 15, 3223 (1982).
19. E. Tornquist, E. D. Adams, M. Copel, T. Gustafsson, and W. R. Graham, *J. Vac. Sci. Technol.* A 2, 939 (1984).
20. S. M. Yalisove, W. R. Graham, E. D. Adams, M. Copel, and T. Gustafsson, *Surf. Sci.* 171, 400 (1986).
21. D. F. Ogletree, M. A. Van Hove and G. A. Somerjai, *Surf. Sci.* 173, 351 (1986).
22. J. R. Smith and A. Banerjea, *Phys. Rev. B* 37, 10411 (1988).
23. G. L. Price, B. A. Sexton and B. G. Baker, *Surf. Sci.* 60 (1976).
24. G. L. Price, B. G. Baker, *Surf. Sci.* 91, 571 (1980).
25. C. R. Brundle, *J. Vac. Sci. Technol.* 13, 301 (1976).
26. A. F. Carley, S. Rassias, M. W. Roberts and W. Tang-Han, *Surf. Sci.* 84, L227 (1979).
27. J. Stohr, K. Baberschke, R. Jaeger, R. Treichler and S. Brennam, *Phys. Rev. Lett.* 47, 381 (1981).
28. D. E. Peebles, E. L. Hardegree and J. M. White, *Surf. Sci.* 148, 635 (1984).
29. M. A. Passler, T. H. Lin and A. Ignatiev, *J. Vac. Sci. Technol.* 18, 481 (1981).
30. M. J. Breitschafter, E. Umbach and D. Menzel, *Surf. Sci.* 109, 493 (1981).
31. S. Lehwald, J. T. Yates, Jr. and H. Ibach, *Proceedings of Fourth International Conference on Solid Surfaces Volume II*, 221 (1980).
32. H. Conrad, G. Ertl, J. Kupperts and E. E. Latta, *Surf. Sci.* 50, 296 (1975).
33. F. Bozso, J. Arias, C. P. Hanrahan, J. T. Yates, Jr, R. M. Martin and H. Metiu, *Surf. Sci.* 141, 591 (1984).

34. Deng Y., 1984, A Theory for Thermoelastic Martensitic Transformation in Cu-Zn-Al Alloys, Doctoral Thesis, Rensselaer Polytechnic Institute, Troy, New York.
35. Z. Nishiyama, Martensitic Transformation, Academic Press, New York, 277 (1978).
36. R. F. Bunshah and R. F. Mehl, Trans. AIME, 1251 (1953).
37. B. D. Cullity, Elements of X-Ray Diffraction, Addison-Wesley, Reading, Mass. (1978).
38. S. Maroie, P. A. Thiry, R. Caudano and J. J. Verbist, Surf. Sci. 127, 200 (1983).
39. K. Yoshida and G. A. Somorjai, Surf. Sci. 75, 46 (1978).
40. R. G. Musket, W. McLean, C. A. Colmenares, D. M. Makowiecki and W. J. Siekhaus, Surf. Sci. 10, 143 (1982).
41. K. Otsuka, C. M. Waymon, and H. Kubo, Met. Trans. 9A, 1075 (1978).
42. T. R. Finlayson, A. J. Morton, and P. D. Norman, Met Trans 19A, 199 (1988).
43. G. Van Tendeloo, M. Chandrasekaran, and F. C. Lovey, In Proceedings of The International Conference on Martensitic Transformations (ICOMAT-86), Japan Inst. of Metals, 868 (1986).
44. G. M. Michal, P. Moine, and R. Sinclair, Acta Metall. 30, 125 (1982).
45. F. C. Lovey and M. Chandrasekaran, Acta Metall. 31, 1919 (1983).
46. A. Nagasawa, ICOMAT-86, 95 (1986).
47. I. M. Robertson and C. M. Waymon, Met Trans 15A, 269 (1984).
48. M. Chandrasekaran, G. Guenin and L. Delaey, J. Phys. Colloq 43, 591 (1982).
49. M. A. Van Hove, W. H. Weinberg, C. -M. Chan, p. 103.

50. Ibid 86.
51. J. A. Klosterman and W.G. Burgers, *Acta Met.* 12, 355 (1964).
52. Y. D. Tyapkin, V. G. Pushin, R. R. Romanova and N. N. Buynov, *Phys. Met. Metallog.* 41, 123 (1976).
53. T. R. Finlayson, A. J. Morton and P. D. Norman, *Met. Trans. A* 19A, 199 (1988).
54. Z. Nishiyama, p. 282.
55. M. A. Van Hove, W. H. Weinberg, C. -M. Chan, p. 43.
56. Ibid, 44.
57. P. R. Watson and J. Mischenko, *Surf. Sci.* 186, 184 (1987).
58. W. B. Pearson, Lattice Spacings and Structures of Metals and Alloys, Vol. 2, Pergamon Press, Oxford (1967).
59. M. A. Van Hove and S. Y. Tong, p. 86.
60. V. L. Moruzzi, J. F. Janek, and A. R. Williams, Calculated Electronic Properties of Metals, Pergamon Press, Inc., New York (1978).
61. C. M. Wayman, *Trans. Met. Soc.. AIME* 224, 1128 (1962).
62. C. Kittel, Introduction to Solid State Physics, fifth edition, John Wiley and Sons, New York 32 (1976).
63. J. E. Demuth, P. M. Marcus, and D. W. Jepsen, *Phys. Rev. B* 11, 1460 (1975).
64. J. R. Smith and A. Banerjea, *Phys. Rev. B* 37, 10411 (1988).

APPENDIX: Computer Programs for Generating
Stereographic Projections and Plotting
Laue Back Reflection Photographs

```

4 KEY OFF
5 REM this program takes the poles from a back reflection
6 REM laue photo and plots them on a wulff net for
  comparison
7 REM with standard projections - data is input in x,y
  coords
8 REM in units of cm
10 KEY OFF
12 CLS
15 DIM H(200),K(200),L(200),X(200),
  Y(200),POLEX(200),POLEY(200)
20 NPLANES = 0
30 INPUT "ENTER NUMBER OF POLES TO PLOT:",NPLANES
35 INPUT "ENTER FILM SAMPLE SEPERATION:",D
37 PRINT "      X , Y"
40 FOR N = 1 TO NPLANES
42 ROW = 4 + N
45 LOCATE ROW,1 :PRINT N;":": LOCATE ROW,4: INPUT "
  ",POLEX(N),POLEY(N)
50 XXX = POLEY(N) : YYY = POLEX(N) : GOSUB 4000
60 MU = ARCTAN
70 YYY = SQR(XXX*XXX + YYY*YYY) : XXX = D : GOSUB 4000
80 SIGMA = ARCTAN/2
90 XXX = 1 : YYY = COS(MU)*TAN(SIGMA) : GOSUB 4000
100 GAMMA = ARCTAN
110 XXX = 1 : YYY = TAN(MU)*SIN(GAMMA) : GOSUB 4000
120 DELTA = ARCTAN
130 H(N) = COS(DELTA)*COS(GAMMA)
140 K(N) = SIN(DELTA)
150 L(N) = SIN(GAMMA)*COS(DELTA)
160 LOCATE ROW,30 : PRINT H(N),K(N),L(N)
170 XXX = L(N) : YYY = H(N) : GOSUB 4000
180 PSIBEG(N) = ARCTAN
190 NEXT N
200 DEF FNACOS(Z) = -ATN(Z/SQR(1-Z*Z)) + 1.5708
210 GOSUB 1010
220 GOSUB 2010
230 GOSUB 3010
240 LOCATE 1,1
250 INPUT "ENTER POLE NUMBER TO PROJECT ",POLENUM
270 IF POLENUM > NPLANES GOTO 3150
272 IF POLENUM <= 0 GOTO 360
280 XXX = L(POLENUM) : YYY = H(POLENUM) : GOSUB 4000

```

```
290 PSIHKL = ARCTAN
300 XXX = H(POLENUM) : YYY = L(POLENUM) : GOSUB 4000
310 THETA = ARCTAN
320 XXX = SQR(H(POLENUM)*H(POLENUM) + L(POLENUM)*L(POLENUM))
      * SIN(PSIHKL+THETA)
330 YYY = K(POLENUM) : GOSUB 4000
340 PHI = -ARCTAN
350 GOTO 210
360 THETA = 0
380 PHI = 0
390 GOTO 210
1000 REM
1010 REM DRAW CIRCLE
1020 REM
1030 CLS
1040 XSCALE = 240/2
1050 YSCALE = XSCALE*5/9
1060 CIRCLE (459,145),240
1070 FOR I=-80 TO 80 STEP 10
1080 A = I/180*3.14159
1090 T = 2*COS(A+1.5708)/(SIN(A+1.5708)+1)
1100 LINE(457,145+T*YSCALE)-(461,145+T*YSCALE)
1110 T = 2*SIN(A)/(COS(A)+1)
1120 LINE(459+T*XSCALE,143)-(459+T*XSCALE,147)
1130 NEXT I
1140 LOCATE 1,65
1150 PRINT
1180 RETURN
2000 REM
2010 REM CALCULATE X,Y COORDINATES OF PROJECTION FOR EACH
      POLE
2020 REM
2030 FOR I=1 TO NPLANES
2078 X1 = SQR(H(I)*H(I) + L(I)*L(I))*SIN(PSIBEG(I)+THETA)
2080 Y1 = K(I)
2082 Z1 = SQR(H(I)*H(I) + L(I)*L(I))*COS(PSIBEG(I)+THETA)
2086 IF ABS(Z1) = 1 GOTO 2092
2088 THETA1 = FNACOS(Z1)
2090 GOTO 2094
2092 THETA1 = (1-SGN(Z1))*1.5708
2094 XXX = X1
2096 YYY = Y1
2098 GOSUB 4000
2100 PHI1 = ARCTAN
2102 X2 = SIN(THETA1)*COS(PHI1+PHI)
2104 Y2 = SIN(THETA1)*SIN(PHI1+PHI)
2106 Z2 = COS(THETA1)
2160 IF X2 < -.02 GOTO 2200
```

```
2170 Y(I) = 2*Z2/(X2+1)
2180 X(I) = 2*Y2/(X2+1)
2190 GOTO 2220
2200 X(I) = 4
2210 Y(I) = 4
2220 NEXT I
2230 RETURN
3000 REM
3010 REM PLOT THE PROJECTIONS
3020 REM
3030 XSCALE = 240/2
3040 YSCALE = XSCALE*5/9
3050 FOR I = 1 TO NPLANES
3060   RADIUS = .04/2*245
3070   XX = X(I)*XSCALE + 459
3080   YY = -Y(I)*YSCALE + 145
3090   CIRCLE (XX,YY),RADIUS
3091   ROW = YY/12 + 1
3092   COL = XX/8.99 + 1
3093   LOCATE ROW,COL : PRINT I
3100 NEXT I
3110 RETURN
3120 FOR I=1 TO NPLANES
3130 LPRINT I,H(I),K(I),L(I)
3140 NEXT I
3150 KEY ON
3160 END
4000 IF(ABS(XXX) < .01) THEN ARCTAN = SGN(YYY)*1.5708 :
      RETURN
4010 IF XXX > 0 AND YYY > 0 THEN ARCTAN = ATN(YYY/XXX) :
      RETURN
4020 IF XXX > 0 AND YYY < 0 THEN ARCTAN = ATN(YYY/XXX) :
      RETURN
4030 IF XXX < 0 AND YYY > 0 THEN ARCTAN = 3.14159 +
      ATN(YYY/XXX) : RETURN
4040 IF XXX < 0 AND YYY < 0 THEN ARCTAN = 3.14159 +
      ATN(YYY/XXX) : RETURN
4050 ARCTAN = (1-SGN(XXX))*1.5708
4055 IF H(I) > 0 AND K(I) > 0 THEN ARCTAN = ATN(K(I)/H(I))
4060 RETURN
```

```
5 REM THIS PROGRAM PLOTS STANDARD STEREOGRAPHIC PROJECTIONS
6 REM this program was written for TI Basic, scaling will
7 REM vary if run under other systems
8 REM
10 DIM X(200),Y(200),H(200),K(200),L(200),R(200),PSIBEG(200)
20 NPLANES = 0
30 FOR I=-3 TO 3
40 FOR J=-3 TO 3
50 FOR M=-3 TO 3
60 SUM = ABS(I) + ABS(J) + ABS(M)
65 REM LINE 70 ELIMINATES POLES ON THE BASIS OF THE bcc
66 REM STRUCTURE FACTOR AND IF THE INDEX IS ARBITRARILY
67 REM HIGH
70 IF (SUM=2 OR SUM=4 OR SUM=6 OR SUM=8) AND (I*I+J*J+M*M) <
    16 GOTO 90
80 GOTO 120
90 NPLANES = NPLANES + 1
100 H(NPLANES) = I : K(NPLANES) = J : L(NPLANES) = M
105 R(NPLANES) = SQR(I*I + J*J + M*M)
112 XXX = L(NPLANES)
113 YYY = H(NPLANES)
114 GOSUB 4000
115 PSIBEG(NPLANES) = ARCTAN
120 NEXT M
130 NEXT J
140 NEXT I
150 DEF FNACOS(Z) = -ATN(Z/SQR(1-Z*Z)) + 1.5708
170 INPUT "ENTER H,K,L: ",HH, KK, LL
171 XXX = LL
172 YYY = HH
173 GOSUB 4000
174 PSIHKL = ARCTAN
175 XXX = HH
176 YYY = LL
177 GOSUB 4000
178 THETA = ARCTAN
180 XXX = SQR(HH*HH + LL*LL)*SIN(PSIHKL+THETA)
182 YYY = KK
184 GOSUB 4000
186 PHI = ARCTAN
210 GOSUB 1010
220 GOSUB 2010
230 GOSUB 3010
240 LOCATE 1,1
250 INPUT "DO YOU WANT ANOTHER PROJECTION [Y/N] ?",ANS$
260 PRINT
270 IF ANS$ = "Y" GOTO 170
280 GOTO 3150
```

```
1000 REM
1010 REM DRAW CIRCLE
1020 REM
1030 CLS
1040 XSCALE = 240/2
1050 YSCALE = XSCALE*5/9
1060 CIRCLE (459,145),240
1070 FOR I=-80 TO 80 STEP 10
1080 A = I/180*3.14159
1090 T = 2*COS(A+1.5708)/(SIN(A+1.5708)+1)
1100 LINE(457,145+T*YSCALE)-(461,145+T*YSCALE)
1110 T = 2*SIN(A)/(COS(A)+1)
1120 LINE(459+T*XSCALE,143)-(459+T*XSCALE,147)
1130 NEXT I
1140 LOCATE 1,65
1150 PRINT HH;KK;LL
1180 RETURN
2000 REM
2010 REM CALCULATE X,Y COORDINATES OF PROJECTION FOR EACH
      POLE
2020 REM
2030 FOR I=1 TO NPLANES
2078 X1 = SQR(H(I)*H(I) + L(I)*L(I))*SIN(PSIBEG(I)+THETA)
2080 Y1 = K(I)
2082 Z1 = SQR(H(I)*H(I) + L(I)*L(I))*COS(PSIBEG(I)+THETA)
2086 IF ABS(Z1) = R(I) GOTO 2092
2088 THETA1 = FNACOS(Z1/R(I))
2090 GOTO 2094
2092 THETA1 = (1-SGN(Z1))*1.5708
2094 XXX = X1
2096 YYY = Y1
2098 GOSUB 4000
2100 PHI1 = ARCTAN
2102 X2 = SIN(THETA1)*COS(PHI1+PHI)
2104 Y2 = SIN(THETA1)*SIN(PHI1+PHI)
2106 Z2 = COS(THETA1)
2160 IF X2 < -.02 GOTO 2200
2170 Y(I) = 2*Z2/(X2+1)
2180 X(I) = 2*Y2/(X2+1)
2190 GOTO 2220
2200 X(I) = 4
2210 Y(I) = 4
2220 NEXT I
2230 RETURN
3000 REM
3010 REM PLOT THE PROJECTIONS
3030 XSCALE = 240/2
3040 YSCALE = XSCALE*5/9
```

```
3050 FOR I = 1 TO NPLANES
3060   RADIUS = .04/R(I)*245
3070   XX = X(I)*XSCALE + 459
3080   YY = -Y(I)*YSCALE + 145
3090   CIRCLE (XX,YY),RADIUS
3100 NEXT I
3110 RETURN
3120 FOR I=1 TO NPLANES
3130 LPRINT I,H(I),K(I),L(I)
3140 NEXT I
3150 END
4000 IF (ABS (XXX) < .01) THEN ARCTAN = SGN(YYY)*1.5708 :
      RETURN
4010 IF XXX > 0 AND YYY > 0 THEN ARCTAN = ATN(YYY/XXX) :
      RETURN
4020 IF XXX > 0 AND YYY < 0 THEN ARCTAN = ATN(YYY/XXX) :
      RETURN
4030 IF XXX < 0 AND YYY > 0 THEN ARCTAN = 3.14159 +
      ATN(YYY/XXX) : RETURN
4040 IF XXX < 0 AND YYY < 0 THEN ARCTAN = 3.14159 +
      ATN(YYY/XXX) : RETURN
4050 ARCTAN = (1-SGN(XXX))*1.5708
4055 IF H(I) > 0 AND K(I) > 0 THEN ARCTAN = ATN(K(I)/H(I))
4060 RETURN
```